Structural changes in heart and kidney tissue in response to modification of substrate availability.

Kirsti Brisk

Trinity College

Department of Physiology, Anatomy and Genetics

Supervisors: Prof. Carolyn Carr and Prof. Helen Christian

Thesis submitted for the degree of

Masters of Science (by Research)

2021

Impact of COVID-19 on this research thesis

Due to lockdown limitations to laboratory occupancy levels, some of the cells and EHTs were produced by Ujang Purnama. Cells and EHT for preliminary experiments were all produced by me. Cell culture duties were shared for the period leading up to and after lockdown in order to minimise the number of people in the lab at any one time. I carried out media changes for the monolayer cells but not the EHTs. I did not complete the final insulin resistance protocol for any tissues (the preliminary experiments used a prototype protocol).

Ideally this project would have involved time spent with the technicians in the Dunn School learning the slicing process and identifying ways to control for the direction of slicing. Unfortunately, the timing of the Coronavirus lockdowns not only made this impossible, but also the technicians were under pressure to complete a backlog of work. There was a delay of several months before receiving the grids.

I suffer with ME and Fibromyalgia which are exacerbated by stress and I have to be careful about not exceeding my energy levels. During lockdown I was living with my parents for support but for personal reasons my brother and his family also came to live in the house, which was then very busy and on top of which I was needed to help with childcare. Over several years I have developed a particular system of medical interventions which enable me to continue with my studies but due to ongoing COVID-19 restrictions I am still not able to access essential elements of this. Increased pain and exhaustion resulted in a significant deterioration in my health and for various periods of time I was not well enough to undertake any academic work.

Contents

Impact of COVID-19 on this research thesis ii

Contents iii

Abstract iv

Acknowledgements vi

Introduction 1

Diabetes 1

Cardiomyopathy 6

Methods 24

Method Development and Results 30

Discussion 58

Conclusion 66

Concluding Statements 68

Appendix 1 -Diabetic nephropathy I

Introduction I

Methods VI

Results VIII

Discussion X

Appendix 2 - References XII

Appendix 3 – Data Processing XXIII

Appendix 4 – R code and References XXVI

Appendix 5 - Experiments XXXIII

Abstract

Introduction

Diabetes is a disease of impaired metabolism caused by a disparity between the insulin secretion necessary to maintain normoglycaemia and the ability of β-cells to secrete insulin. In all types of diabetes this results in hyperglycaemia which may lead to tissue damage. This project investigates the structural changes in human induced pluripotent stem cell-derived cardiomyocytes (hiPSC-CM) as a result of maturation and insulin resistance.

Separately, this project also briefly investigates the effects of hyperglycaemia on the structure of glomeruli in a mouse model of diabetic nephropathy (βV59M).

Methods

hiPSC-CM in monolayer and in 3D as engineered heart tissue (EHT) were treated with oleic acid to increase maturity, and with palmitic acid and high insulin to induce insulin resistance. Previous work in the Carr group had shown that both treatment with oleic acid and culture as EHT induced a switch from glycolysis to oxidative metabolism and induction of insulin resistance impaired glucose metabolism. Transmission Electron Microscopy (TEM) was used to produce high magnification images which were assessed for quantitative analysis of muscle, nuclear area and mitochondrial area and structure. Statistical analysis was performed using R.

Sections of diabetic and control mouse kidney were stained with periodic acid Schiff's assay (PAS), and confocal microscopy was used to observe mesangial matrix expansion. The glomeruli in these images were graded to produce quantitative data.

Results

Nuclear area, muscle area, as well as mitochondrial size, number and total area, were all increased by culturing hiPSC-CM in EHT. However only mitochondrial size and muscle area were further increased by oleic acid treatment. Insulin resistance had a significant effect only on average muscle area and on the distribution of the data for mitochondrial size and nuclear area.

There was a significant increase in mesangial matrix expansion in 12-week diabetic mice compared to non-diabetic mice.

Conclusions

Transmission electron microscopy images of hiPSC-CM showed changes in muscle area and mitochondrial morphology in hiPSC-CM cultured in 3D as EHT. Induction of insulin resistance caused increased disorder of mitochondria. Image analysis using FIJI and statistical analysis using R enabled some conclusions to be supported quantitatively. Orientation of slicing and separating mitochondrial populations would be important aspects of future work.

The βV59M mouse model shows significant indications of mesangial matrix expansion. Further work should include identifying the cause of the PAS staining using glycogen anti-bodies.

Acknowledgements

I am very grateful to the Wellcome Trust for extending my funding to allow me to complete my studies despite delays due to poor health and COVID-19.

My greatest appreciation goes to Prof. Carolyn Carr for personal support and understanding as well as academic guidance.

I would have been unable to undertake the TEM imaging without the training and supervision of Prof. Helen Christian who graciously gave up significant amounts of her time, which helped me to learn this new set of skills.

My thanks to Ujang Purnama for his constant positivity and providing previous data, training in hiPSC-CM and EHT culture protocols and providing cells and EHT when Covid restrictions limited lab occupancy.

I am grateful to the technicians at the Dunn School for producing the grids for my TEM imaging despite the challenges of Covid restrictions.

My thanks to Dr. Lisa Heather for kindly providing electron microscopy images of rat heart tissue for comparison, I hope the results of my project may be helpful in any future image analysis.

The statistical analysis required proved to be more complex than initially expected so I am grateful to Dr. Jack Miller for his enthusiastic advice on statistics and introduction to coding in R.

To the members of CMRG, I thank-you all for a supportive and stimulating environment to complete my studies. It was a joy to be working in your group and you helped me regain my love of research.

I am thankful to Dr. Maria Rohm for providing the fixed kidneys, training in scoring and support in the initial stages of the kidney project.

I am indebted to Prof. Frances Ashcroft and Prof Roger Cox for providing the opportunity for me to study in Oxford.

Introduction

Diabetes

Diabetes Mellitus is a disease which constitutes a large economic burden globally. In the UK, in the financial year 2017/2018, 53.4 million prescription items were dispensed on the NHS for diabetes with the total net ingredient cost alone amounting to around £1 billion[1]. It is estimated that by 2035/36 the total economic cost of diabetes in the UK will be almost £40 billion per year, including both medical bills and indirect losses to the economy[2].

All forms of diabetes are characterised by a disparity between the insulin secretion necessary to maintain normoglycaemia, and the ability of patients' β-cells to secrete this insulin. However, the cause of this disparity differs between types of diabetes. In 2018 in the UK, the prevalence of diabetes was 6.7%, the majority of which (~90%[1]) was due to Type 2 Diabetes Mellitus (T2DM). Type 1 Diabetes Mellitus (T1DM) is an autoimmune reduction of β-cell mass, often at a young age, and accounts for approximately 10% of cases. It causes severe and irreversible loss of insulin secretion and needs to be treated with insulin. T2DM is associated with several risk factors, both genetic and environmental. Genome-wide association studies have identified around 400 loci[3]. Risk factors include increased age, non-white ancestry and family history, as well as environmental factors such as increased BMI, abdominal obesity (independent of BMI), unhealthy diet, disturbed sleep, and a sedentary lifestyle[4]. Neonatal Diabetes (ND), which is rare (~1 in 100,000 births), is a severe genetic disorder that is usually diagnosed within 6 months of birth. It can cause a severe loss in insulin secretion due to mutations

affecting all β-cells. Depending on the specific mutation, some patients with ND can be treated with sulphonylureas[5].

T2DM is a progressive disease where the initial cause can be unclear. The main areas the disease affects are blood glucose levels, circulating free fatty acids, insulin signalling and β-cell function. The dysfunction of these all feed into each other and can cause further deterioration creating a 'downward spiral' of disease. Hyperglycaemia is an example of this, where glucose toxicity causes damage to β-cell function leading to even less control of blood glucose levels[6,7].

Common to all types of diabetes is an absence of, or insensitivity to, plasma insulin which results in an imbalance in substrate metabolism leading to micro- and macro- vascular complications. The majority of these secondary complications can be attributed to elevated plasma glucose levels and the resulting glucotoxicity[6]. Macrovascular complications include heart attack and stroke, while microvascular include retinopathy, neuropathy (especially peripheral) and nephropathy[4]. This project investigates aspects of diabetic cardiomyopathy in T2DM and nephropathy induced by hyperglycaemia.

Hyperglycaemia

An increase in gluconeogenesis in the liver is responsible for increasing the basal plasma glucose levels[8] via a combination of decreased insulin sensitivity, increased glucagon sensitivity and increased substrate delivery[4]. Postprandial plasma glucose levels are increased by impaired suppression of hepatic glucose production and decreased hepatic glucose uptake[9,10].

Other causes of hyperglycaemia include: reduced non-insulin mediated glucose uptake[9,10], excessive renal glucose reabsorption via the sodium/glucose co-transporter[11],

a higher plasma glucose threshold for transferring glucose to urine[4], and impaired insulin mediated vasodilation increasing the time over which both glucose and insulin can reach tissues[12,13].

Insulin Resistance

Insulin resistance occurs when cells cannot respond to normal levels of insulin. This causes the β-cells to increase insulin release in order to maintain healthy levels of plasma glucose. Prolonged insulin release then causes damage to the β-cells and ultimately leads to apoptosis and a decrease in plasma insulin[14]. Insulin resistance occurs in many tissues (e.g. adipose, kidney, gastro-intestinal tract, vasculature and brain tissues, as well as the pancreatic β-cells themselves) but is particularly problematic in muscle and liver as these are the main tissues that remove glucose from the plasma after a carbohydrate meal[4].

Cellular causes of insulin resistance include abnormalities in insulin signalling (discussed below), glucose transportation, glucose phosphorylation, glycogen synthesis, pyruvate dehydrogenase complex activity and mitochondrial oxidative activity[4,8,15,16].

Molecular mechanisms of insulin and insulin resistance

Insulin binds to the insulin receptor, activating insulin receptor tyrosine kinase which leads to the phosphorylation of insulin receptor substrates (IRS)[17]. Phosphorylated IRSs activate signalling molecules such as Phosphatidylinositol-3-Kinase (PI3K). PI3K promotes the translocation of the glucose transporter 4 (GLUT4) to the plasma membrane increasing the transportation of glucose into relevant tissues (GLUT4 is mainly found in muscle). Increased glucose uptake phosphorylates the transcription factor forkhead box protein O1 (FOXO1), inactivating it and altering the transcription of downstream genes. Insulin also acts via the RAS–mitogen-activated protein kinase (MAPK) pathway[4].

Insulin resistance is caused by altered phosphorylation of IRS, preventing downstream signalling, including the PI3K pathway[18,19], and can cause degradation of the IRS [20]. There are many causes of altered phosphorylation[21,22]:

- abnormal lipid accumulation (often associated with obesity)[23]
- mitochondrial dysfunction (associated with obesity) [24–26]
- inflammation[27]
- endoplasmic reticulum (ER) stress[4]

A detailed description of the complex causes of altered phosphorylation in IRS phosphorylation is beyond the remit of this thesis. However, Khalid et al[14].present a comprehensive review of the changes to the insulin signalling pathway in insulin resistance, including a clear diagram providing an overview of the pathways in Figure 1 of the review[14].

β-cell dysfunction

The involvement of β-cell dysfunction in the progression to diabetes (T2DM) is described by Weir and Bonner-Weir in five stages[28]:

Stage 1: insulin resistance in insulin sensitive tissues leads to a compensatory increase in insulin secretion by β-cells. It is clinically seen as an increased glucose stimulated insulin secretion (GSIS) response to intravenous glucose, possibly due to the increased β-cell mass seen at this stage. While this is known as stage 1 of diabetes disease progression, clinically it is described as the “prediabetic period”.

Stage 2: loss of the acute (>10 minute) period of GSIS alongside elevated fasting plasma glucose levels (above 5.6 mM) and changes to β-cell gene and protein expression. These

changes are likely to be linked with glucotoxicity. Clinically this is a “stable” phase and can be controlled with lifestyle changes, with varying degrees of success.

Stage 3: a significant increase in glucose levels indicates the start of this clinically “unstable” phase which occurs when the β-cells can no longer maintain stable glucose levels with the increased insulin secretory function (although some newer studies suggest that dietary changes can still slow or even reverse the decline). This is likely due to a combination of further increased insulin resistance and a decline in β-cell function. This stage is a rapid decline into clinical diabetes.

Stage 4: another stable phase, often the final stage for T2DM. Insulin secretion levels have dropped significantly but remain high enough to prevent decline into ketoacidosis. β-cell mass may have decreased by up to 50%, however insulin secretion has decreased by a greater proportion, suggesting decreased efficiency in the insulin secretion of the remaining β-cells as well as the β-cell loss.

Stage 5: clinically characterised as a decline into ketoacidosis. This is generally only seen with T1DM, where the functional β-cell mass is more severely decreased than T2DM, unless T2DM is combined with additional factors such as severe pancreatitis.

Cardiomyopathy

According to the British Heart Foundation, both the deaths by and burden of people living with heart disease is a major concern. Approximately 25% of all UK deaths are caused by heart and circulatory disease. Around 7.6 million people are living with heart and circulatory diseases in the UK. To put this in perspective, this is more than twice the number of people living with cancer and Alzheimer's disease combined[29].

Diabetic Cardiomyopathy

Diabetic cardiomyopathy is a disease leading to structural, functional and metabolic changes to the myocardium as a result of Diabetes Mellitus. It can occur along side but is independent of other cardiovascular disease and hypertension[30]. Male patients with T2DM are twice as likely to suffer heart failure when compared to their male contemporaries. Women with T2DM are five times more likely to suffer heart failure than their peers. Studies also show increased mortality and rate of re-hospitalisation for patients hospitalised for heart failure with diabetes compared to those without[31]. Although these sex differences are substantial they are not addressed in this project as it focuses on other aspects of cardiac tissue model development.

Despite many studies and clinical trials, the evidence is inconclusive as to the beneficial effect of tight glycaemic control on cardiovascular risk in patients with diabetes, suggesting that other risk factors such as elevated lipids and increased inflammation are also key[32]. Similarly, studies looking at cardiovascular risk in patients with diabetes being treated with diabetic drugs show a mixture of both increased and decreased risk. There are also links between the diabetic myocardium and cardiac hypertrophy, increased LV mass and wall thickening, increased oxidative stress, and ROS[31]. When Diabetic

Cardiomyopathy was initially identified it was observed as a dilated phenotype with an increased LV volume and reduced LV ejection fraction (Heart Failure Reduced Ejection Fraction, HFREF). However more recently a restrictive phenotype has been identified with a preserved ejection fraction (Heart Failure Preserved Ejection Fraction, HFPEF) which is widely considered to be an initial stage in a progression of the disease to the dilated phenotype[30]. Figure 1 summarises the metabolic and structural disease progression.

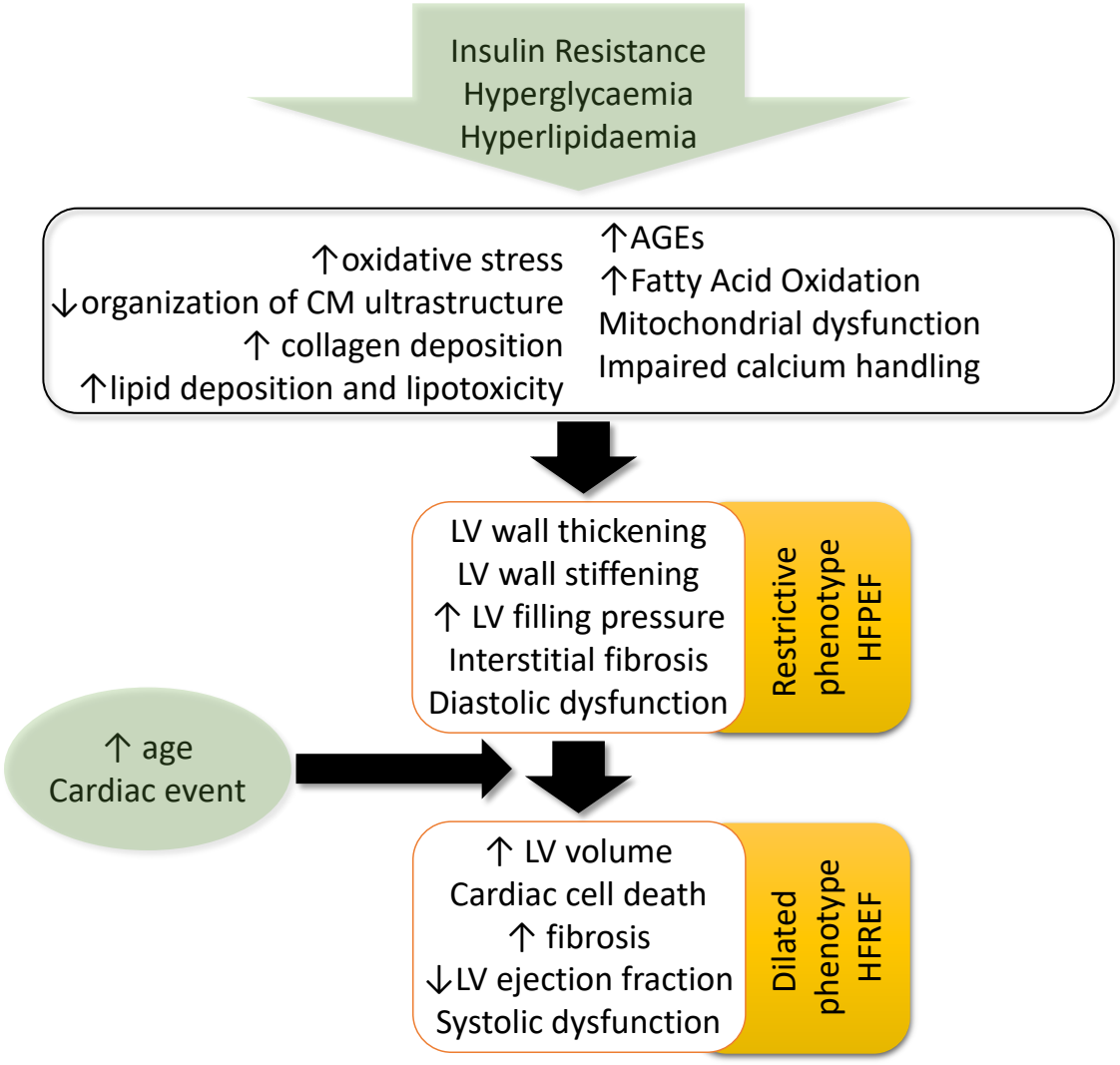


***Figure 1**: Diabetic Cardiomyopathy metabolism and structure summary.*

A study in Scotland[33] looking at risk factors and treatments shows 32% of patients with T2DM also had a recorded history of cardiovascular disease (CVD). This study highlights three primary risk factors as age (53% of patients ≥80 years old had CVD compared to

15% of patients <60 years old), gender (35% of males patients compared 29% of females patients) and length of time since a diabetes diagnosis. Having adjusted for these factors it became clear that there are a further six risk factors highlighted in the study: higher BMI, higher HbA_{1c}, smoking, albuminurea, higher cholesterol and higher blood pressure. In this study, 65% of men and 68% of women (all with T2DM) display two or more of these risk factors. This is despite a third of these patients already being in receipt of two or more drugs to control the risk factors.

Treatments

Treatments for CVD with T2DM focus on reducing identified risk factors. Non-drug interventions are a useful tool but medication will also be required for many patients. Treatments to reduce blood pressure and cholesterol levels in T2DM patients follow the same path as for patients without diabetes, including lifestyle changes combined with use of statins and anti-hypertensive medications as appropriate[34–36]. A US study[37] shows, in a cohort of patients including all types of diabetes, the positive impact of successful intervention of multiple risk factors. By successfully meeting less intense control goals for all three of HbA_{1c}, blood pressure, and cholesterol, a 37% risk reduction of all-cause mortality is achieved, again confirming that T2DM is a multi-factorial disease.

Medications specifically for elevated HbA_{1c} act through several different mechanisms. Metformin, one of the most commonly prescribed, inhibits hepatic gluconeogenesis, increases insulin sensitivity and decreases glucagon sensitivity[38]. Pioglitazone, a thiazolidinedione, also increases insulin sensitivity but by activation of PPARγ and to a lesser extent, PPARα[39]. Canagliflozin, Dapagliflozin and Empagliflozin are sodium/glucose co-transporter 2 inhibitors (SGLT2i) and reduce the reabsorption of glucose from urine.

Recent trials, EMPEROR-Reduced[40] and DAPA-HF[41,42], have shown Empagliflozin and Dapagliflozin are effective in reducing the risk of CVD in diabetic and non-diabetic patients alike, separate to the impact of glycaemic control. Liraglutide and Semaglutide are glucagon-like peptide 1 receptor agonists (GLP-1RA) and reduce the blood glucose by increasing insulin sensitivity and decreasing glucagon sensitivity[43,44].

Although the impact of these anti-diabetic medications on the risk of CVD has not always been clear, the study in the US suggests hazard ratios of 0.86 for Canagliflozin and Empaglifozin, 0.87 for Liraglutide and 0.74 for Semoglutide [43–46]. Given the study in Scotland shows each of these drugs being prescribed to fewer than 4% of patients[33], there is room for improvement to be made from wider use of these drugs.

In addition to the treatments for the identified risk factors previously discussed, pharmaceutical treatments that target the increased fatty acid uptake into the cell and mitochondria, and the increased fatty acid metabolism are of potential benefit in preventing or treating diabetic patients with heart disease. Unfortunately, so far, medications have proved to have limited benefit or dangerous/life threatening side effects. Fibrates act as PPARα agonists and are thought to have beneficial effects for patients with dyslipidaemia, however CPT-1 inhibitors Etomoxir and Perhexiline cause hepatoxicity and Thiazolidediones (PPARγ agonists) are associated with an increased risk of myocardial infarction.[47]

Structural, functional and metabolic characteristics of Diabetic Cardiomyopathy

Tissue level

Characteristics of Diabetic Cardiomyopathy vary but include impaired calcium handling. With the restrictive phenotype, there is a normal LV cavity and LV ejection fraction but

increased LV filling pressures with thickened and stiff LV wall. In the case of the dilated phenotype the LV cavity is larger than normal with a decreased ejection fraction. Both systolic and/or diastolic dysfunction have been reported, with diastolic common in the early stages of the disease (reported in 40-75% of asymptomatic Type 1 and Type 2 Diabetic patients) and systolic dysfunction more common as the disease progresses[30].

Cell level

Changes to diabetic heart cell structure mainly involve impaired organisation of the ultrastructure, changes to cell size and an increase in collagen deposition. There is a reduction in number and organisation of actin filaments[48]. Similarly, there are fewer and less well organised T-tubules than in a healthy heart but this may be less drastic than in non-diabetic cardiac disease[48]. The mitochondria appear swollen and, again, less organised[49]. In a rat model of diabetes, transmission electron microscopy (TEM) analysis showed changes in the myofibrils, disrupted mitochondria and increased lipids and collagen fibres[50]. In particular, the diabetic heart shows disruption and thinning of the myofibrils and swollen mitochondria with disrupted inner and outer membranes.

As on a tissue level, the changes seen in a diabetic heart on a cellular level depend on the phenotype of the heart: restrictive or dilated. In the restrictive phenotype cardiomyocytes are hypertrophied, due to increased glucose availability[51] in combination with other factors, including inflammation, oxidative stress, insulin resistance and activation of AMPK[52]. However, in the dilated phenotype there is a reduced cell diameter[48] and volume while the length of the cardiomyocytes appears unchanged. There is also considerable reduction of cell volume generally which has been replaced with collagen[51].

Increase in collagen deposition is a hallmark of both diabetic cardiac phenotypes. In normal hearts the collagen is mainly type I and III, in the diabetic heart there is an increase in production of type I but not III. This causes the stiffness seen in the LV in the restrictive phenotype. At this earlier stage the collagen has accumulated between the cells in the interstitial space, however in the dilated phenotype the collagen has replaced cells. Collagen synthesis is dysregulated in diabetes as profibrotic signalling is upregulated by advanced glycation end-products[53]. Increased apoptosis and necrosis are also seen in the diabetic heart, resulting from molecular mechanisms that also increase fibrosis and inflammation, and myocardial lipid accumulation leads to increased ceramide production and ER stress[54]. The collagen deposition is a combination of increased production in the fibroblasts already in the tissue and migration/differentiation of other cells such as fibroblasts migrating from the bone marrow or endocardium and pericytes differentiating into collagen producing cells[51].

Metabolism

Metabolism in the heart is of particular importance due to the high energy requirements and ATP turn over (0.5 $\mu mol.gww^{-1}$ ATP used per second[55]). To enable the heart to respond to changing substrate supply and energetic demands, it is able to switch fuel source rapidly. Fatty acids are more efficient energy producers in terms of ATP produced per carbon but have a higher O_2 requirement per ATP produced than carbohydrate fuels[47].

60-70% of the ATP requirement is produced via fatty acid metabolism under normal conditions[56]. The main stages of fatty acid metabolism[47] are: transport into the cell (FAT/CD36 translocase[57]), cytosolic lipid storage, transport into the mitochondria

(attachment of CoA by acyl-CoA synthetase, acyl group used to attach to carnitine, transported by carnitine-actylcarnitine translocase, removal of carnitine), β-oxidation (oxidation, hydration and thiolysis metabolise the fatty acid into multiple acetyl-CoA molecules to enter the Krebs cycle), and transfer from the mitochondria to the site of ATP utilisation (transfer of phosphate group from ATP to creatine in mitochondria and then back to a different ADP at the site of utilisation).

Given the dependence of the heart on fatty acid metabolism, it is unsurprising that changes are associated with disease. In non-diabetic heart disease, a decline in cardiac function correlates with a reduction in fatty acid metabolism, reduced PCr/ATP ratio[58,59] and reduced expression of proteins involved in fatty acid metabolism[60–63].

In diabetic heart disease, the opposite can be seen: namely an increase in fatty acid metabolism. In a mouse model, an increase in circulating lipids and concomitant increase in fatty acid metabolism has been seen before the presence of hyperglycaemia[64], suggesting that, at the onset of T2DM, lipotoxicity is of greater concern than glucotoxicity. The early effects of lipotoxicity result in symptoms of diastolic dysfunction and impaired response to cardiac stress[65]. Lipids of particular concern and research at present are ceramide, diacylglycerol and fatty-acyl-CoA[66,67].

The increase in circulating lipids seen in the mouse also fits with the increase in transport of fatty acids into the heart (with an increase in both the number of transport proteins and the proportion of transport proteins localised at the membrane[68]), the increase in fatty acid storage both in and around the heart[69], and the increase in expression, via PPARα, of genes involved in fatty acid uptake into the cell and mitochondria, fatty acid β-oxidation and lipid storage[70].

The myocardial oxygen consumption (MVO_2) is increased in diabetes, the majority of which can be explained by the increased oxygen demanded by the increase in fatty acid metabolism[71]. However, the increase in MVO_2 cannot be explained by the change in substrate alone. Other proposed causes, which are known to occur in the diabetic heart, are futile lipid cycling, oxygen wastage by uncoupling proteins and atypical calcium handling[72–74]. This increase in MVO_2 explains why the diabetic heart is unable to tolerate low oxygen environments leading to contractile defects[75].

Models of Diabetic Cardiomyopathy

Rodent

Rodents are good models for Diabetic Cardiomyopathy as they are not predisposed to traditional coronary artery disease, so any results are clearly due to diabetic cardiomyopathy and not atherosclerosis. Although the majority of genetic models are in mice, rat models are also used due their larger heart size, particularly for physiological measurements e.g. MRI or perfusions[76].

The most common rodent models of T2DM (e.g. ob/ob, db/db mice and ZDF rats) have genetic changes in leptin signalling. The ob/ob has a mutation in the ob(Lep) gene that prevents a functional form of leptin being produced. The db/db mouse and ZDF rats both have mutations affecting the leptin receptor gene (Ob-R) rather than leptin itself. All three rodent models prevent leptin action in the hypothalamus, preventing appetite suppression and causing obesity. The ZDF rats required further breeding, selecting rats that had hyperglycaemia, as the mutation was initially causing obesity but not diabetes. While modelling the basic diabetic phenotype of obesity and glucose and insulin abnormalities, these models do not mimic the causes of T2DM in humans, which are

often a combined result of genetic predisposition and environmental factors. Practically, these models can also be expensive and time consuming as the rats can take months to develop cardiac symptoms [76,77].

The Heather group have developed a rat model for early-stage T2DM which also models the cardiac changes associated with human patients [78]. This is based primarily on the models described in Reed et al and Srinivasan[79,80]. The Heather group's model uses Wistar rats and low dose streptozotocin (STZ) combined with a high fat diet. These rats have hyperglycaemia and increased fat in the liver but maintain their body weight, have normal insulin levels and do not develop ketosis. There are changes in the heart metabolism that model the increased fat metabolism and decreased glucose metabolism seen in the hearts of patients. This is indicated by decreased glucose metabolism protein levels, increased triglyceride concentrations, increased fat metabolism protein levels and increased levels of transcription factors associated with metabolism of fatty acids[78].

Cellular

While the advantages of *in vivo* models are clear, there are significant differences between rat and human heart tissue, including elevated heart rate and contraction, differing oxidative phosphorylation, and expression of contractile proteins and ion channels[81,82]. Therefore, there is a need to create models of cardiac structures using human cells or tissue. Human induced pluripotent stem cells (hiPSCs) that can be guided into differentiation into cardiomyocytes provide an attractive solution. They allow for patient-specific cells to be used in genetic disease modelling and easy expansion of hiPSCs makes them less limited than other human cell sources. Burridge et al.[83] provide a good overview of many published protocols used for differentiating human pluripotent

stem cells. An important factor in the majority of these protocols is the timely activation and then inhibition of WNT signalling, and that any protocol needs to be precisely and accurately followed in order to have reproducibility. The protocol used in the Carr laboratory for hiPSCs into cardiomyocytes is based on that in Lian, X et al.[84]

Despite significant research in the area, there are still concerns over the maturity of hiPSC-derived cardiomyocytes (hiPSC-CMs) which can differ from adult tissue in many ways which are summarised in Table 1.

***Table 1**: Summary of the differences between adult heart tissue cardiomyocytes and mature hiPSC-CMs*

Characteristic	Adult heart CMs	Mature hiPSC-CMs
gene expression profiles [85]		similar to foetal heart but differ from adult tissue, especially in respect to sarcomeric isoforms, calcium handling and ion channel genes
bioenergetics [86]	Fatty acid oxidation is the predominant pathway for energy generation	largely glycolytic as they are grown in high glucose medium with little or no fatty acids
electrophysiology[87]	Resting membrane potential ~ -85 mv, maintained by cardiac ion channels Action potential has plateau phase Ventricular CM do not beat spontaneously	Resting membrane potential ~ -5- to-60 mV Upstroke velocity slower and shorter plateau phase Beat spontaneously
T-tubules [88]	considered essential for efficient calcium delivery directly to the ryanodine receptor to induce calcium-induced calcium release	have rarely been identified Sarcomeres that are near the cell surface activated by calcium released at cell periphery
size and shape of the CMs	~150x10µm cylinder shaped cells[88]	triangular or oblong and only ~30x10µm[89,90]
nuclei [90]	bi- or multi-nucleated	rarely have more than one nucleus per cell
sarcomere development [91]	organised into A-bands, I-bands, Z-discs and M-bands	mostly aligned myofibrils with some indications of A-bands, I-bands, Z-discs and M-bands
size and organisation of mitochondria[85,92,93]	mitochondria are organised in networks	even in more mature hiPSC-CMs mitochondria appear randomly distribution, sometimes beginning to cluster
	mitochondria organise into separate populations which can be identified by their location and have distinct physiologies and morphologies[94,95]	
	Perinuclear (PN) mitochondria are round and found in clusters next to the nucleus	
	Subsarcolemmal (SS) mitochondria are also rotund and are found in clusters ‘under’ the sarcolemma	
	Interfibrillar (IF) mitochondria are layered between sarcomeric structures and are more elongated in shape	
	connections between mitochondria and sarcoplasmic reticulum exist in human heart tissue	No connections between mitochondria and sarcoplasmic reticulum are apparent
cellular make up	cardiomyocytes are mainly composed of sarcomeres and mitochondria: 40-52% of the cytoplasmic volume consists of myofibrils with 15-25% of the cytoplasmic volume being mitochondria[96–98].	As hiPSC-CMs mature the ratio of sarcomeres and mitochondria to cytoplasmic volume increase but are significantly less than those in adult cardiomyocytes[99].

Methods used to increase maturity in hiPSC-CMs include 3D culture, optionally with mechanical stress or load, electrical stimulation, changes in metabolism and long-term culture[100].

The use of 3D culture of stem cell-derived cardiomyocytes as a human model of cardiac tissues has developed alongside a medical need for better ways to repair hearts after myocardial infarction. Engineering heart tissue that can then be used to replace or support heart tissue that is damaged due to ischemia has a clear medical application. The development of these 3D tissues also provides a model of heart tissue that can be made with human cells for pre-clinical research or drug testing[100].

The process of producing 3D tissues requires two things: a scaffold and cells. There are three main scaffold types: solid matrix, decellularised natural scaffolds and liquid hydrogels. Solid matrices and decellularised scaffolds require cells to migrate into the scaffold to form a fully cellularised structure and the solid material can hinder cell to cell contact leading to anoikis[101–104]. Hydrogels, however, allow full permeation of cells through the structure and can show reduced anoikis even where cell to cell contact is not present on casting[105,106]. Another benefit of hydrogels is the ease with which the tissue can be formed around and attached to posts or holders, allowing the tissue to develop under strain or with a mechanical load, leading to the formation of beating tissues[107–109].

In the Carr group, the differentiation protocol used produces a cell population with 75-90% of cells positive for alpha-actinin, indicating differentiation into cardiomyocytes is achieved and a combination of methods are used to mature the cardiomyocytes[86]. Figure 2 shows images and data from previous work on development of these models in the Carr lab. The cells were grown in culture medium with low glucose and supplemented with oleic acid. This pushed the cells towards using increased fatty acid metabolism and

decreased glucose metabolism, more akin to that in the adult heart, as seen in Figure 2D. Figures 2A and 2B show oleic acid increased sarcomeric actin and mitochondria respectively. The cells were grown as engineered heart tissue (EHT) using the model developed by Breckwoldt et al.[110,111] where they are cast into hydrogel moulds around posts which, when the cells have formed tissue, create a mechanical stress for the beating cells to pull against. An image of the EHT on the posts is in Figure 2C, which shows an increase in sarcomeric actin in EHT compared to monolayer cell culture. Increased organisation of sarcomeres is apparent in the EHT confocal image but detail is lacking. A model of insulin resistance (IR) has also been developed in the Carr lab by treating the mature monolayer cells or EHTs with palmitic acid in glucose-free media for 3 days, followed by 3 days in media containing palmitic acid with high glucose and high insulin. This protocol induced insulin resistance as confirmed by ablated AKT phosphorylation in response to insulin (Figure 2E). The IR protocol induced a reduction in glycolysis and an increase in fatty acid oxidation (albeit not significant in the preliminary data shown) as seen in Figure 2F, and an increase in lipid accumulation (Figure 2G).

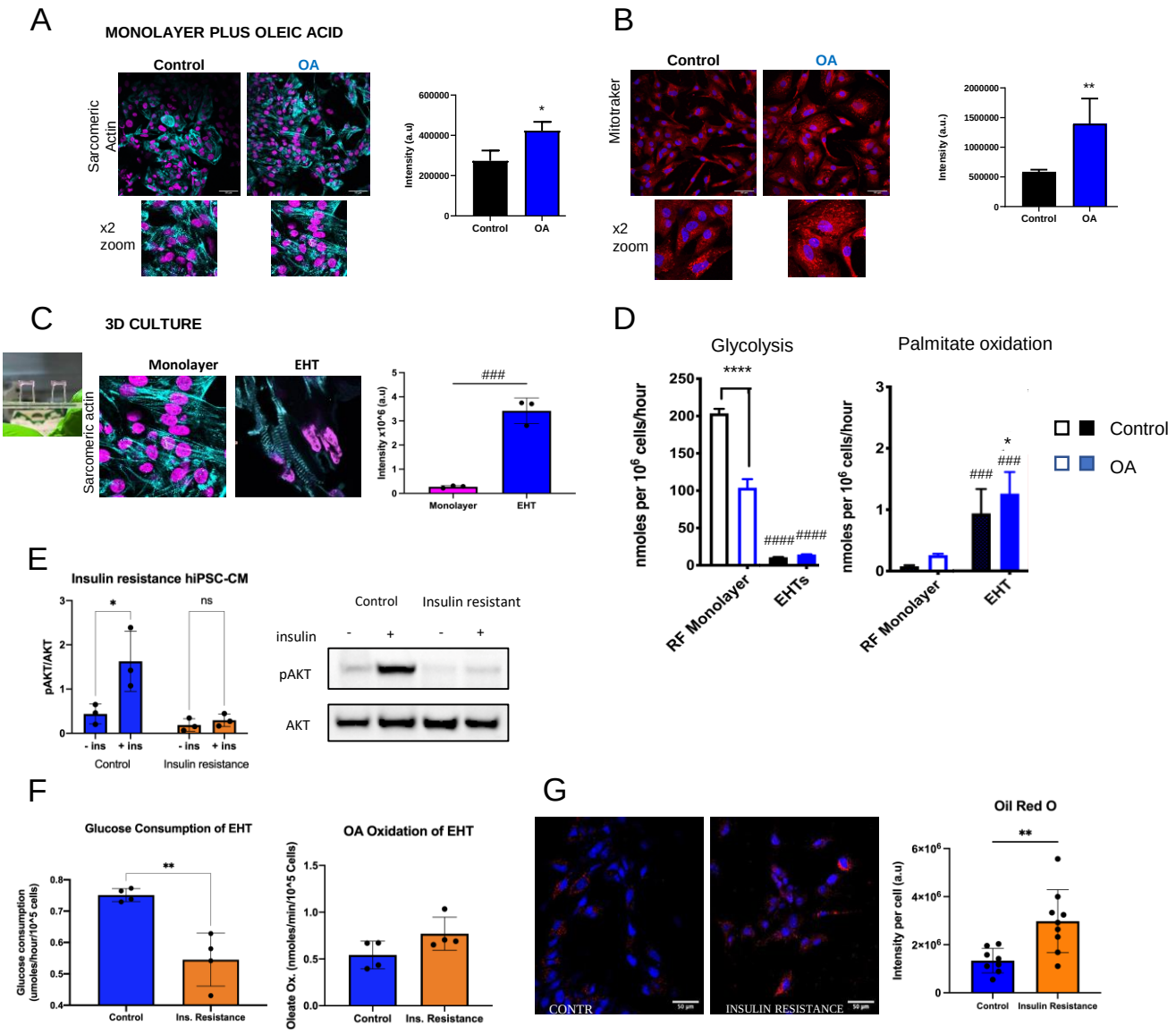


***Figure 2**: Previous data from the Carr group, Treatment of hiPSC-CMs in monolayer with OA for one week increases expression of sarcomeric actin (A) and mitochondrial membrane potential (B). 3D culture as engineered heart tissue (C) increases sarcomeric actin expression and shows formation of sarcomeric structure. (D) Culture with OA for one week and in EHTs decreases glycolysis and increases fatty acid oxidation. (E-G) Culture in high glucose/palmitate/insulin media induces insulin resistance shown by decreased phosphorylation of AKT (E), decreases glycolysis (F) and increases lipid deposition (G). *P<0.05, **P<0.01, ***P<0.001, ****P<0.0001 compared with control; # P<0.05, ## P<0.01, ###P<0.001, ####P<0.0001 compared with monolayer.*

The work in this thesis aims to investigate whether these metabolic changes are accompanied by morphological changes in CM mitochondria. For example, respiration complexes have been shown as necessary for sarcomeric structural organisation in maturation of CMs[112]. For Diabetes Mellitus, particularly important are the proteins involved in mitochondrial fission and fusion: DLP1, mitofusin (Mfn1 and Mfn2), Mff, Fis1, MiD49/51 and optic atrophy 1[113]. Correct regulation and function of these proteins are important for inner and outer mitochondrial membranes, cristae morphology, size, and transfer of mitochondrial DNA through fusion and fission[49]. Also important is the permeability transition pore, which, when closed, increases oxidative phosphorylation coupling, and when open leads to an osmotic gradient and swelling of the mitochondria[114]. Morphological changes reported in diabetic patient cardiac tissue or models include: reduced IF mitochondrial length, mitochondrial fragmentation, disorganised cristae, decreased size of mitochondria, swollen mitochondria, and increased total mitochondrial content[49]. These changes in morphology could cause reduced bioenergetic efficiency and mitochondrial dysfunction, leading to increased reactive oxygen species and cellular oxidative damage.

Electron Microscopy

Specifically, this project focuses on changes to the ultrastructure of the hiPSC-CM in 2D and in EHT using Transmission Electron Microscopy (TEM).

Rather than diffracting light, TEM imaging uses magnetic lenses to direct a beam of electrons. A high voltage current runs through a tungsten filament, heating it and producing electrons. The electrons enter the section as a constant beam and differential transmission through the section creates an image on a fluorescent screen which allows for initial visualisation to pinpoint the area of interest. The screen is then removed, the

electrons focused further and visualisation at the higher magnification is possible using a digital camera.

There are four stages to sample preparation: fixing, post-fixing and staining, embedding and slicing. A mixture of paraformaldehyde and glutaraldehyde are used to fix the sample, the first providing rapid fixing and the second longevity. This combination allows the use of larger specimens, otherwise the centre of a sample would deteriorate before glutaraldehyde had diffused in. In order to increase resolution between structures, samples are stained with heavy metals in the post-fixing and staining stage. The heavy metals impede the electrons as they pass through the sample, creating the differential transmission that allows visualisation[115]. Osmium is used to visualise lipids and uranium for proteins. Ultra-thin slices are required, to allow the electrons to pass through, and therefore the sample is embedded in plastic for support so it does not tear when sliced. Spurr's resin is used due its low viscosity and enhanced penetration of the samples[115].

Although sample preparation is more difficult for TEM than light microscopy and immunohistochemistry, and the equipment is expensive, TEM has significant benefits due to the higher magnification and resolution. TEM provides direct visualisation of intracellular structures, such that it is possible to see the structure of mitochondria (including cristae formation), sarcomeres and T-tubules and specific location of these structures within the cell. Another benefit of TEM is being able to measure structures more accurately. However, because the technique is highly labour intensive and each image visualises only a small section of the sample at a time, quantification is difficult. This explains why, in the literature, electron microscopy images are more often used as qualitative data to reinforce other findings. In this project we wanted to determine whether it is feasible to produce quantitative data to support the visual differences seen

in the images. Therefore, we developed methods to analyse and process the images to provide quantitative analysis.

Aims

In summary:

There is a need for models of cardiac structures using human cells or tissue for disease modelling, preclinical testing of pharmaceuticals and clinical replacement of cardiac tissue after myocardial infarction. An attractive solution is to use human induced pluripotent stem cells (hiPSCs) differentiated into cardiomyocytes. However, concerns remain over the lack of maturity of hiPSC-derived cardiomyocytes (hiPSC-CMs) compared to adult tissue.

The Carr group use altered metabolism (use of oleic acid) and culturing in 3D as EHT to increase maturity and generate a model for insulin resistance using low glucose, high insulin and palmitic acid. Metabolic and confocal microscopy methods have previously been used to identify levels of maturation in these models.

The work in this thesis aims to investigate whether these metabolic changes are accompanied by further morphological changes in CM, especially in the mitochondria, by using TEM and quantitative analysis of the resulting images.

The specific aims are:

- To compare different cellular cardiomyocyte models for maturity and/or adverse changes due to insulin resistance

Immature Monolayer Cells	Mature Monolayer Cells	Insulin Resistant Monolayer Cells
Immature EHT	Mature EHTs	Insulin Resistant EHTs

- To quantitatively assess the cellular and mitochondrial organisation and structures by measuring
  - Mitochondrial Number
  - Mitochondrial dimensions
  - Mitochondrial Contacts/networking
  - Nuclear Area
  - Muscle Development by area of filaments
- To qualitatively assess the structure of the cells and the mitochondrial focusing on
  - Cristae formation
  - Presence of T-tubules
  - Organisation of sarcomeres
- To compare cellular models with rat heart TEM images provided by Dr. Lisa Heather

Methods

All materials were used according to manufacturers' protocols unless otherwise specified. Due to lockdown limitations to laboratory occupancy levels, some of the cells and EHTs were produced by Ujang Purnama. Details of who performed each individual part of the experiments can be found in Appendix 5.

iPSC culture

The induced pluripotent stem cell line was cultured in TeSR-E8 media (STEM CELL Technologies) on matrigel (Corning Life Sciences) coated plates and flasks. Dissociation was performed using ReLeSR (STEM CELL Technologies) for 1 min at RT followed by a 6 min incubation at 37°C. The cells used were iPS(IMR-90)-4 which are human induced pluripotent stem cells generated from the IMR-90 cell line. [116] The original IMR-90 cell line is described as a fibroblast like cell line derived from lung tissue of a female foetus[117].

iPSC differentiation to CM

The iPSCs were differentiated according to a protocol based on those described in Lopez et al.[86] and Lian, X et al.[84] Flasks and plates were coated with reduced growth factor Matrigel (Corning Life Sciences) and cells initially plated using TeSR-E8 media. Media was changed over the 15-day protocol as indicated in Table 2.

***Table 2**: iPSC differentiation protocol*

Day 0 (24 hrs after plating)	RPMI 1640 (Gibco), 1% B-27 Supplement minus insulin (Gibco, B-27-I) and 6µM CHIR99201 (Tocris Bioscience)
Day 2	RPMI 1640 and 1% B-27-I
Day 3	RPMI 1640, 1% B-27-I and 2.5 µM Wnt-C59 (Tocris Bioscience)
Day 5	RPMI 1640 and 1% B-27-I
Day 7	Fresh RPMI 1640 and 1% B-27-I
Day9	Fresh RPMI 1640 and 1% B-27-I
Day 11	RPMI 1640, no glucose (Gibco) and 1% B-27-I
Day 13	RPMI 1640, no glucose (Gibco) and 1% B-27-I
Day 15 onwards Replaced on alternate days	RPMI 1640 and 1% B-27 supplement (Gibco)

Casting EHT

EHT production was based on protocols in Breckwoldt, K et al.[111] and Hansen, A. et al.[110] 1.6-1.8 ml of 2% ultra-pure agarose (Invitrogen), dissolved in sterile PBS, was placed in each well of a 24 well plate, with Teflon spacers (EHT Technologies) to create moulds. The spacers were removed after at least 1hr of cooling. hiPSC-CMs were dissociated over 4 hrs at 37°C with 200U/ml Collagenase II (Gibco) to produce single cells. After centrifugation, the cells were resuspended in EHT master mix (Table 3). 116 µl of mastermix was mixed with 3.6 µl thrombin and swiftly added into the moulds. The rack of silicon posts (EHT technologies) was added so that each mould contained two posts. After

2 hrs at 37°C, 400 µl of NKM was added for a further incubation of 30 mins. The formed EHTs, suspended on the posts, were transferred to new 24 well plates with 1.5 ml EHT media per well. The EHT media was exchanged for fresh on alternate days for maintenance.

Table 3: *Culture Media Recipes*

NKM	100 ml		DMEM (Biochrom)
	10 ml		Foetal Bovine serum (Thermofisher)
	1 ml		Penicillin/Streptomycin (Gibco)
	1 ml		L-glutamine (Life Technologies)
EHT Media	45 ml		DMEM
	500 µl		Penicillin/Streptomycin
	50 µl		Insulin 10 mg/ml
	50µl		Aprotinin 33 mg/ml (sigma)
	10 ml		Horse serum
EHT Master Mix	1x (µl)	4.5x (µl)	
	94.56	425.5	NKM
	6.68	30.1	2x DMEM
	0.12	0.5	Rock Inhibitor (Tocris)
	12	54	Matrigel
	3.04	13.7	Fibrinogen (sigma) and Aprotinin
	116.40	523.8	

CM and EHT maturation

CM or EHT were cultured in low glucose (5.5 mM) maintenance media supplemented with 400 µm oleic acid for 7 days.

Insulin resistant CM and EHT

CM or EHT were cultured in glucose-free IR media for 3 days followed by low glucose IR media for 4 days.

***Table 4**: Insulin Resistance Media Recipe*

Insulin Resistance Media (glucose-free and low glucose)	43.945 ml	DMEM No glucose for glucose-free IR Media Low glucose (5.5 mM) for IR media
	50 µl	Insulin 10 mg/ml
	5 ml	Horse serum
	1.05 ml	Palmitic acid-BSA 6:1

Fixing CM and EHT

Monolayer cells were passaged and seeded on polycarbonate filters on transwell plates (Appleton Laboratories) 24 hours before fixing. The EHTs were removed from their posts and cut using a scalpel immediately before fixing. All samples were immersion fixed in fresh 2 % paraformaldehyde/2.5 % glutaraldehyde, cells were fixed for 1 hour in their plates and EHT sections in Eppendorf tubes for 2 hours. Samples were then stored in 10 % fixative solution until processing.

Processing CM and EHT

Samples were washed with 0.1 M phosphate buffer (PB) before post-fixing in 1 % w/v osmium tetroxide (in 0.1 M PB), staining with 2 % w/v uranyl acetate (in distilled water). Increasing concentrations of ethanol (70-100 %) and then acetone were used to dehydrate the samples before embedding in Spurr's resin (Agar Scientific).

Sectioning CM and EHT

Sections of 50-80 nm thickness were cut using a Reichert ultracut S-microtome (Riechert-Leica) and mounted on 200 mesh nickel grids (Agar Scientific). (Performed by staff in the Dunn School).

Imaging

A JEM 1010 JEOL transmission electron microscope was used to examine the sections and a GANTAN Orius digital camera was used to take 20-30 images per sample. Using FIJI (Image J), each image was analysed by drawing a Region Of Interest (ROI) around each cellular structure of interest (Appendix 3 Figure 1), and the scale parameter was input to FIJI. Various parameters of the ROI sets were measured by FIJI and transferred to an Excel spreadsheet (Appendix 3 Figures 2 and 3). The data were processed to produce the required total and average values and transferred to a second spreadsheet (Appendix 3 Figure 4) before being imported to R for analysis. Table 5 shows the number of images analysed for each group.

Table 5: *Number of images analysed for each group*

	Control	Mature	IR
Cells	98	230	188
EHT	154	159	59

Statistics

Statistical tests were performed using Prism initially and then in R (code in Appendix 4). Log or Box-Cox transformations were performed and a linear mixed effects model fitted before parametric tests. A two-way ANOVA and estimated marginal means pairwise equality tests (Kenward-Roger degrees of freedom and Tukey P-value adjustment methods) were computed. The Ansari-Bradley non-parametric pairwise variance equality test (Tukey P-value adjustment method) was run for all parameters. For Nuclear Area and Muscle Area parameters, the Wilcoxon rank sum test with continuity correction using the Holm P-value adjustment method (a non-parametric pairwise comparison of medians) was also measured. P-values of less than 0.05 were considered significant for all parameters and tests except parametric tests performed on Nuclear Area and Muscle Area where P-values of less than 0.01 were considered statistically significant.

Method Development and Results

Preliminary Experiment

Electron microscopy images are at the nanometer scale and so it is not always straightforward to understand what cellular components are present. After producing some preliminary images, therefore, the first stage was to determine how to identify the various cellular components. I used Wheater's Functional Histology to identify structures of interest. Figure 3 is adapted from Robertson et al.[85] and summarises the features of interest in maturing human pluripotent stem cell derived cardiomyocytes (hiPSC-CMs).

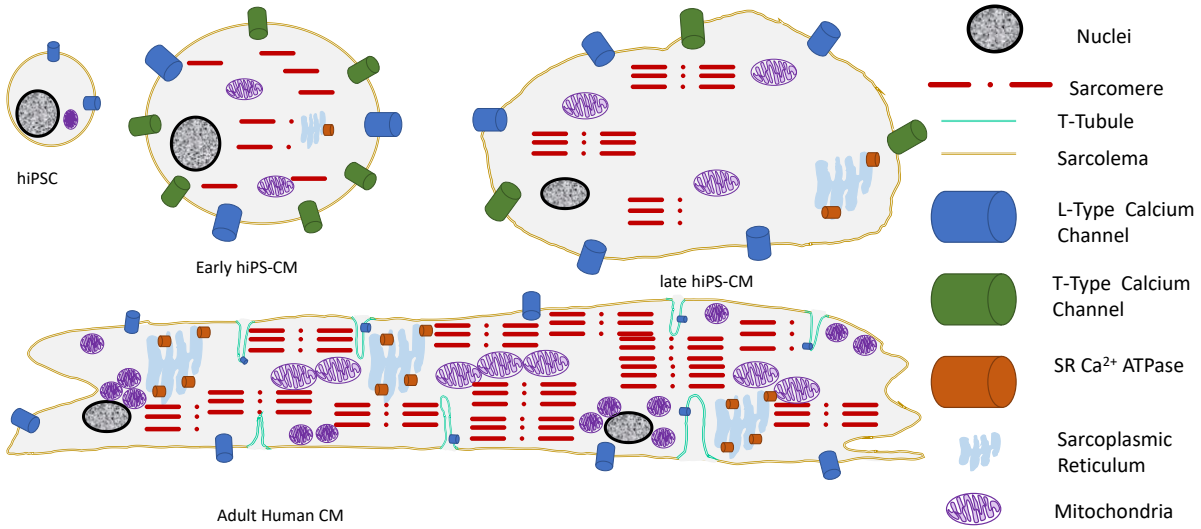


***Figure 3** : features of maturing human pluripotent stem cell derived cardiomyocytes (adapted from Robertson et al.[85])*

Figure 4 comprises three images showing cellular structures such as nuclei, mitochondria, muscle fibres, ribosomes and lipid droplets, in different regions of the cell. Some of the structures are unambiguous, especially the nuclei which can be identified as a membrane bound light grey speckled area containing darker speckled areas close to the membrane. Sometimes a darker area is visible in the middle of the nucleus, this is the nucleolus. However, many of the structures appear different in different images or are difficult to identify. In our data, lipid droplets always appeared as solid dark grey round areas.

However, in other published images the lipid itself has been lost during processing, and the lipid droplet is noticeable by its absence (i.e. bright white areas inside the cell).

The mitochondria can vary in size, shape and location. They can be found anywhere within the cell, sometimes individually and sometimes in clusters. The visualisation of mitochondrial cristae also varies greatly from fine, dark cristae on a lighter mitochondrial matrix to a small number of thick cristae often with a much brighter matrix. In some cases, the cristae are undefined.

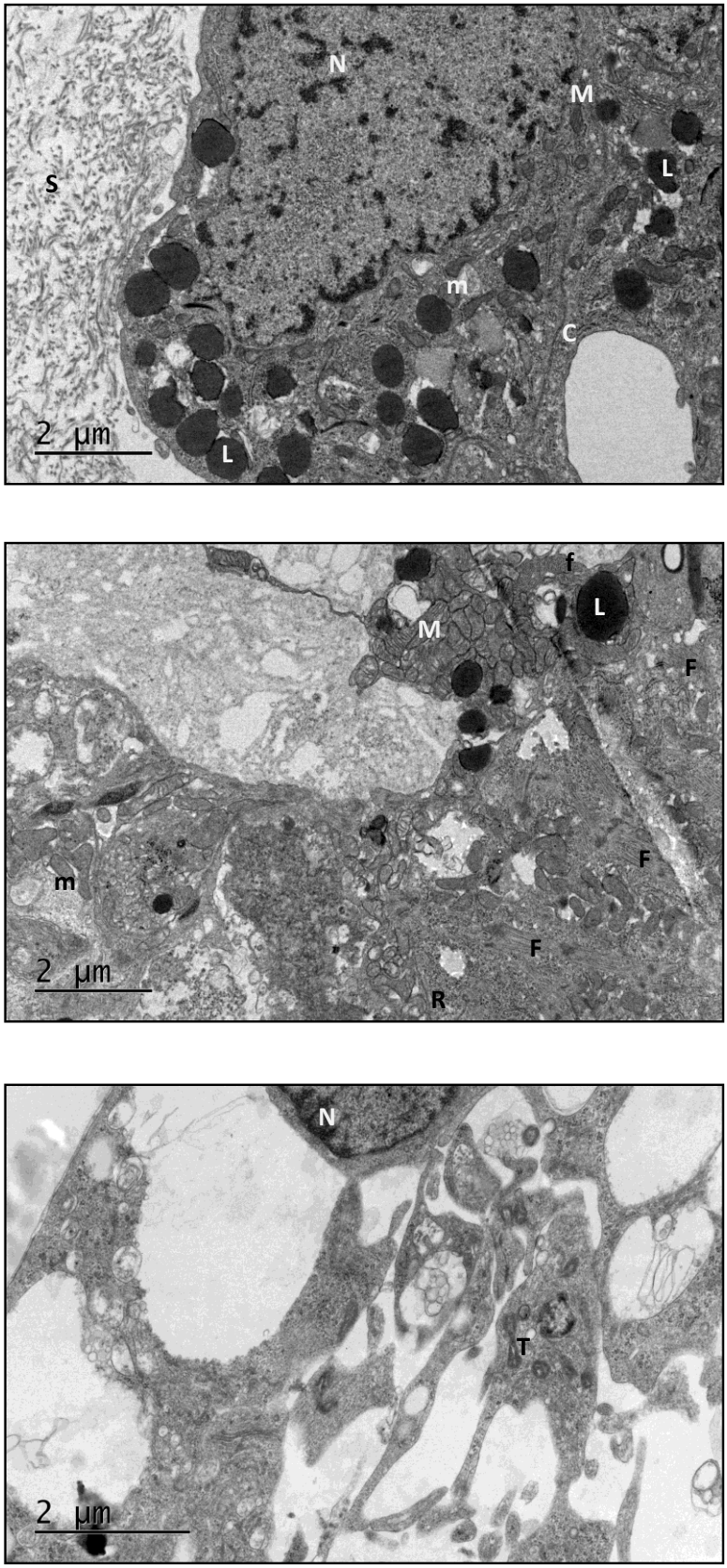


***Figure 4** : Example TEM images. N, nuclei; C, cell boundary; M, mitochondria (fine, dark cristae); L, lipid droplet; m, mitochondria (less defined cristae); T, mitochondria (thick cristae); S, supportive matrix; F, muscle filaments (longitudinal); f, muscle filaments (cross-sectional); R, ribosomes*

Glycogen granules and ribosomes both appear as dark spots in the cytoplasm in unlabelled TEM and the two are reported as being difficult to distinguish in un-labelled TEM[118]. A less common difficulty is the difference between these structures and myosin or actin filaments, which is further complicated by the disorganised nature of immature iPSC-derived cardiomyocytes. When observing the filaments longitudinally, the filaments are clear and the organisation towards sarcomere structures are sometimes evident. However, when the filaments are seen in cross section, they can appear very similar to the ribosomes although the latter can be distinguished as being less regular in shape, and often seen in star-shaped clusters. The cross section of the filaments can also sometimes be seen as short ovals where they have been cut diagonally.

Dr Lisa Heather kindly provided TEM images of control and diabetic rat heart[78] as an example of mature cardiac tissue for comparison with our cultured cells and EHT, shown in Figure 5. These images clearly show muscle fibres and sarcomeres, with mitochondria evident between the fibres, and highlight the difference between mature 3D muscle and immature cardiomyocytes in 2D or loose 3D structures. As sarcomeres and muscle fibres are directional structures, the plane on which the slicing for TEM grids has been done affects the resulting image. In Figure 5, images a and b show the rat heart sliced along the plane of the muscle fibres and sarcomeres. As a result, Figure 5a is composed mainly of one cell (with more cells just visible in the top and bottom of the image). There are clear linear sarcomeric structures and mitochondria layered between them. Figure 5b is of higher magnification and shows the sarcomeric structure in more detail. In comparison, Figure 5's c and d show a cross sectional slice of the muscle fibres of the rat heart. Consequently, Figure 5c shows multiple cells, and the mitochondria are more randomly distributed than the layered organisation of Figure 5a. Although there are darker lines

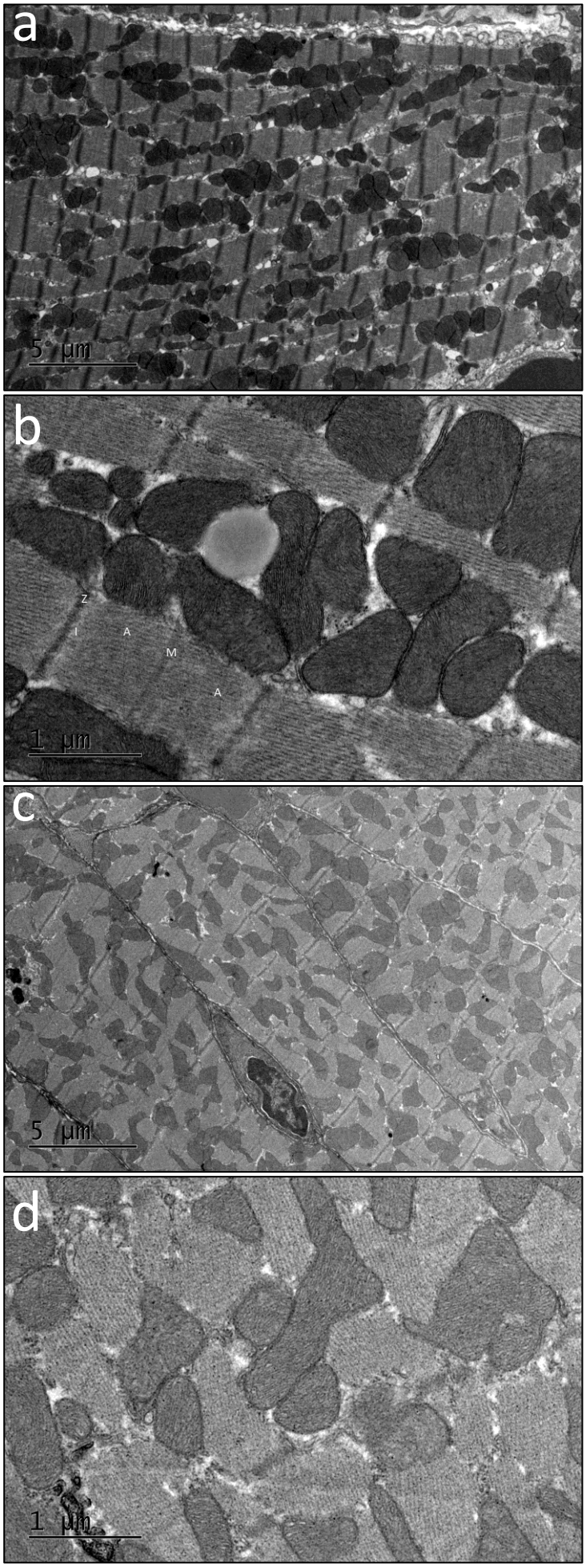


***Figure 5**: images provided by Dr. Lisa Heather. Rat heart sections sliced longitudinally to muscle filaments(a,b) and cross-sectionally to muscle filaments (c,d). Z, Z-line; A, A-band; I, I-band; M, M-band*

within the fibrils seen in Figure 5c, these should not be mistaken for any of the lines or bands associated with the side-on view of a sarcomeric structure. Figure 5d is a higher magnification, and when compared to 5b can be seen to have a different organisation to the longitudinal sarcomeric structure. Figure 5b shows dark Z-lines, flanked by the lighter I-band. The darker section between the I-bands is the A-band, with the M-line in the middle. Perpendicular to these bands, filament lines are apparent. However, despite showing darker areas similar to Z-lines, Figure 5d has no further structure. Furthermore, when compared to 5c, the muscle filaments have a more dotted appearance.

While in rat heart images the orientation of the slice is clear, the less organised structure of cultured cells and EHT makes these structures more difficult to identify. Ideally this project would have involved time spent with the technicians in the Dunn School learning the slicing process and identifying ways to control for the direction of slicing. Unfortunately, the timing of the Coronavirus lockdowns not only made this impossible, but also the technicians were under pressure to complete a backlog of work. There was a delay of several months before receiving the grids.

Having identified the various features in the preliminary images from cultured Cells and EHT, the next stage was to determine what it was realistic to attempt to quantify. Measurements of the area of a cell covered by muscle, nuclei and mitochondria were practical and useful measurements, as were measurements of mitochondrial number, size (average area and maximum diameter) and shape (circularity). The preliminary experiment used a package in Image J to look at mitochondrial networking. However, the high magnification of the TEM images made this unfeasible. 3D confocal microscopy would provide a better platform for assessing mitochondrial networking. Measuring

specific features of mitochondria, such as distance between cristae, was also considered but ultimately deemed too impractical as the cristae were not always easily visualised.

Images – Qualitative Data

Limitations of qualitative Images

Figure 6A is a selection of images showing increasing maturation of CMs from Control Cells and EHT through Mature to insulin resistant cells and EHT. Work from the Carr group has shown that maturation of the cells by addition of oleic acid and by 3D culture

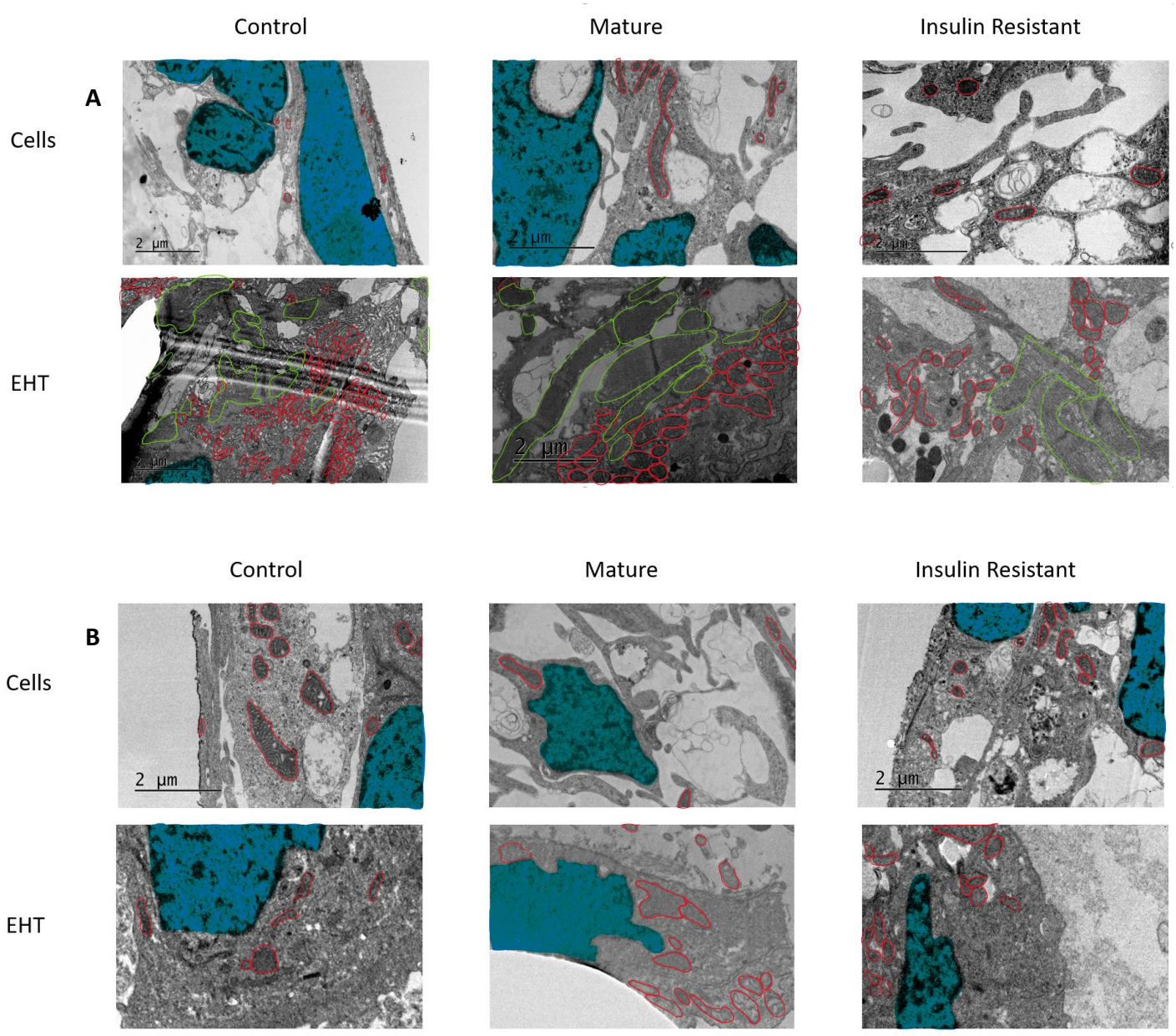


***Figure 6**: two selections of TEM images A, maturation of cells from Control Cells through Mature Cells and Control EHT to Mature EHT; B, no maturation. Blue, Nuclei; Red, Mitochondria; Green, Muscle Fibres*

resulted in a switch from glycolysis towards fatty acid oxidation and an increase in mitochondrial membrane potential (Figure 2). Insulin resistant cells and insulin resistant EHT had greater fatty acid oxidation compared to control, impaired contractility and lipid accumulation. Insulin resistant cells had lower glucose consumption. In the TEM images in Figure 6A, maturation in the 3D EHT can be seen through increased mitochondrial content (red), increased muscle fibre content and organisation (green), and decreased nuclear content (blue). In the insulin resistant cells and EHT the muscle fibres appear less well formed and mitochondria more dispersed. However, a second selection of images (Figure 6B) from the same data set fails to show the maturation seen in 6A. This highlights the lack of robustness of qualitative analysis in this context and the difficulty in selecting 'representative images'. An aim of this project is therefore to develop a protocol for converting this qualitative data set of images to quantifiable data.

Quantitative Data - Method Development

Using FIJI (Image J), each image was analysed for mitochondria, cell area, nuclear area and muscle fibres by drawing a Region Of Interest (ROI) around each cellular structure of interest (Appendix 3 Figure 1). Since the images were produced at different magnifications, a parameter was input to FIJI to adjust for different scales. Various parameters of the ROI sets were measured by FIJI and transferred to an Excel spreadsheet (Appendix 3 Figures 2 and 3). The data were processed to produce the required total and average values. The data of interest were then extracted and transferred to a second spreadsheet (Appendix 3 Figure 4). These processed data were then imported to R for analysis. Table 5 shows the number of images analysed for each group.

Quantitative Data - Analysis in R

Data were first analysed using Prism, and graphs were produced for each parameter (Figure 7). The graphs show little difference in mitochondrial number, size, or shape. There is no difference in circularity, and the small differences seen in number, size and Feret's diameter are unreliable due to large variability in the data. The ratios of total Muscle, Nuclear and Mitochondrial area to the cell area do show clear differences between Cells and EHT, with Mitochondrial Area and Muscle Area greater in EHT, while Nuclear Area is smaller.

There were limitations to the available statistical tests and modelling in Prism. I was unconvinced of the reliability of the results from those statistical tests for my data sets. For this analysis the data from the three biological replicates were combined. Advice from Dr Jack Miller confirmed that this approach was more appropriate than to average the data from each biological replicate and then analyse the data as n=3 from each group. However, in Prism there was no ability to control for the random variable (Sample Name). There was also no option for non-parametric two-factor analysis.

Therefore, data visualisation and statistical analyses were completed in the open-source statistical package R, which provides a level of complexity and flexibility that is not available in alternative statistical packages.

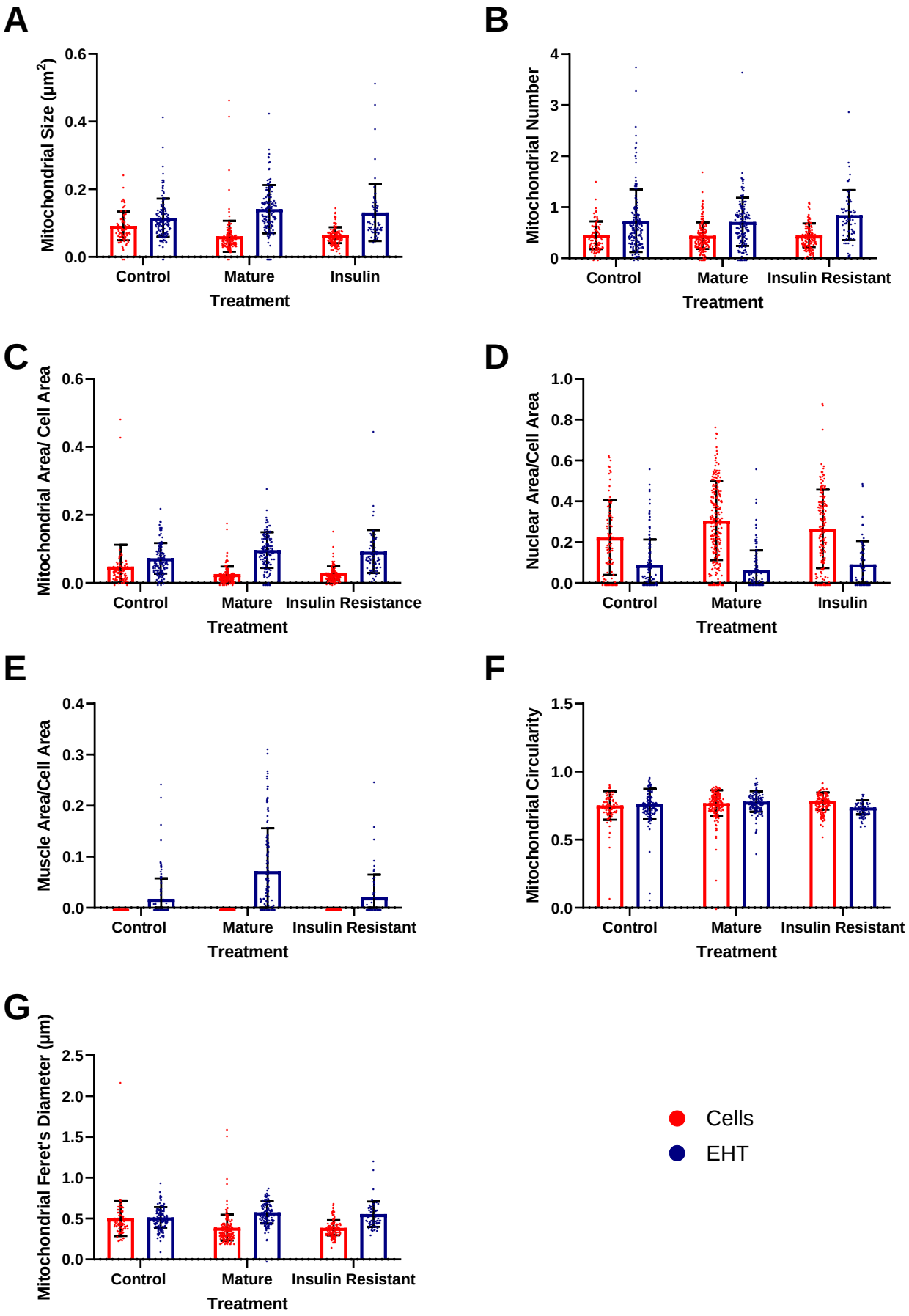


***Figure 7**: Graphical representation with Prism. Individual data points, means and SEM are plotted. Red, Monolayer Cells; Blue, EHT. Data plotted against treatment. A, Mitochondrial Size (µm$^{2)}$; B, Mitochondrial Area; C, Mitochondrial Area/Cell Area; D, Nuclear Area/Cell Area; E, Muscle Area/Cell Area; F, Mitochondrial Circularity; G, Mitochondrial Feret's Diameter (µm)*

As all the graphs in Figure 8 show, the data are not normally distributed. Initially, it was thought the data could be lognormally distributed. Therefore, for the parameters with no 0 values, log transformations were performed. For the parameters with a small number of 0 values, a small constant (half the smallest non-zero value) was added to each data point before log transformations were performed. The log transformations did not produce distributions that were completely normal (Figure 9). However, it was considered that the distributions were close enough to normal for parametric statistics, as long as the tests chosen were sufficiently robust to small deviations from normal distribution. The exception to this were the two parameters containing a large number of 0 value data points, namely Muscle Area and Nuclear Area as many images did not contain muscle and/or nucleus. These parameters required further transformation. The Box-Cox method of transformation was used, however the distributions still deviated from normal (Figure 9D and E) and therefore Aligned Rank Transform ANOVA was performed. Nevertheless, given the extent of skewness of the data and the large number of 0s causing multiple ties in aligned rankings, the Type 1 error is concerning[119]. For comparison, after the Box-Cox transformation, the same parametric tests were performed on the Muscle Area and Nuclear Area data as for the rest of the data, including both parametric and non-parametric multiple comparisons. The most trustworthy of the statistical results for these two data sets are the non-parametric multiple comparisons.

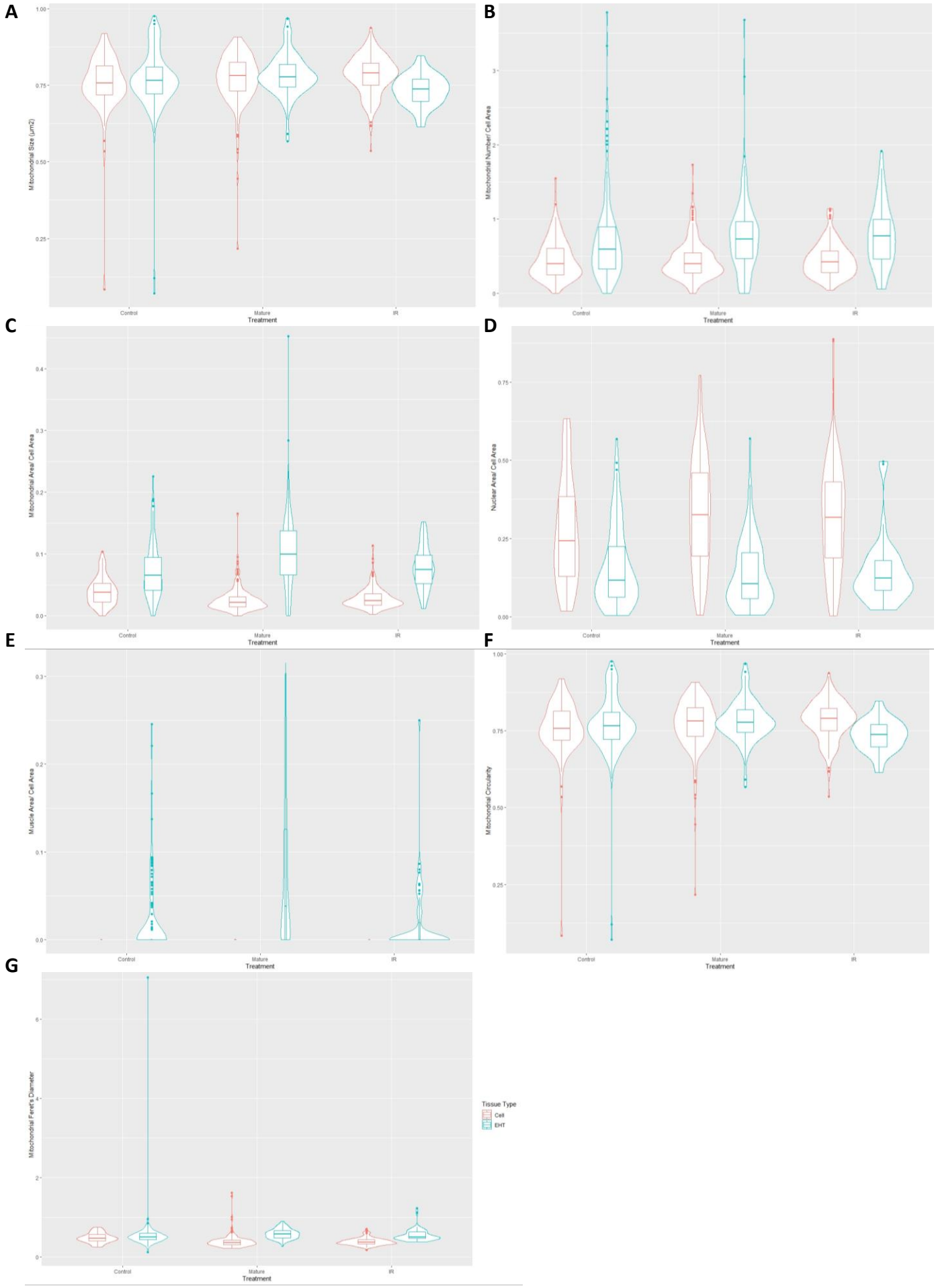


***Figure 8**: Graphical representation of raw data with R. Red, Monolayer Cells; Blue, EHT. Data plotted against treatment. Violin plots are overlayed with boxplots showing the median and interquartile ranges. A, Mitochondrial Size ($\mu m^{2)}$; B, Mitochondrial Number; C, Mitochondrial Area/Cell Area; D, Nuclear Area/Cell Area; E, Muscle Area/Cell Area; F, Mitochondrial Circularity; G, Mitochondrial Feret's Diameter (µm)*

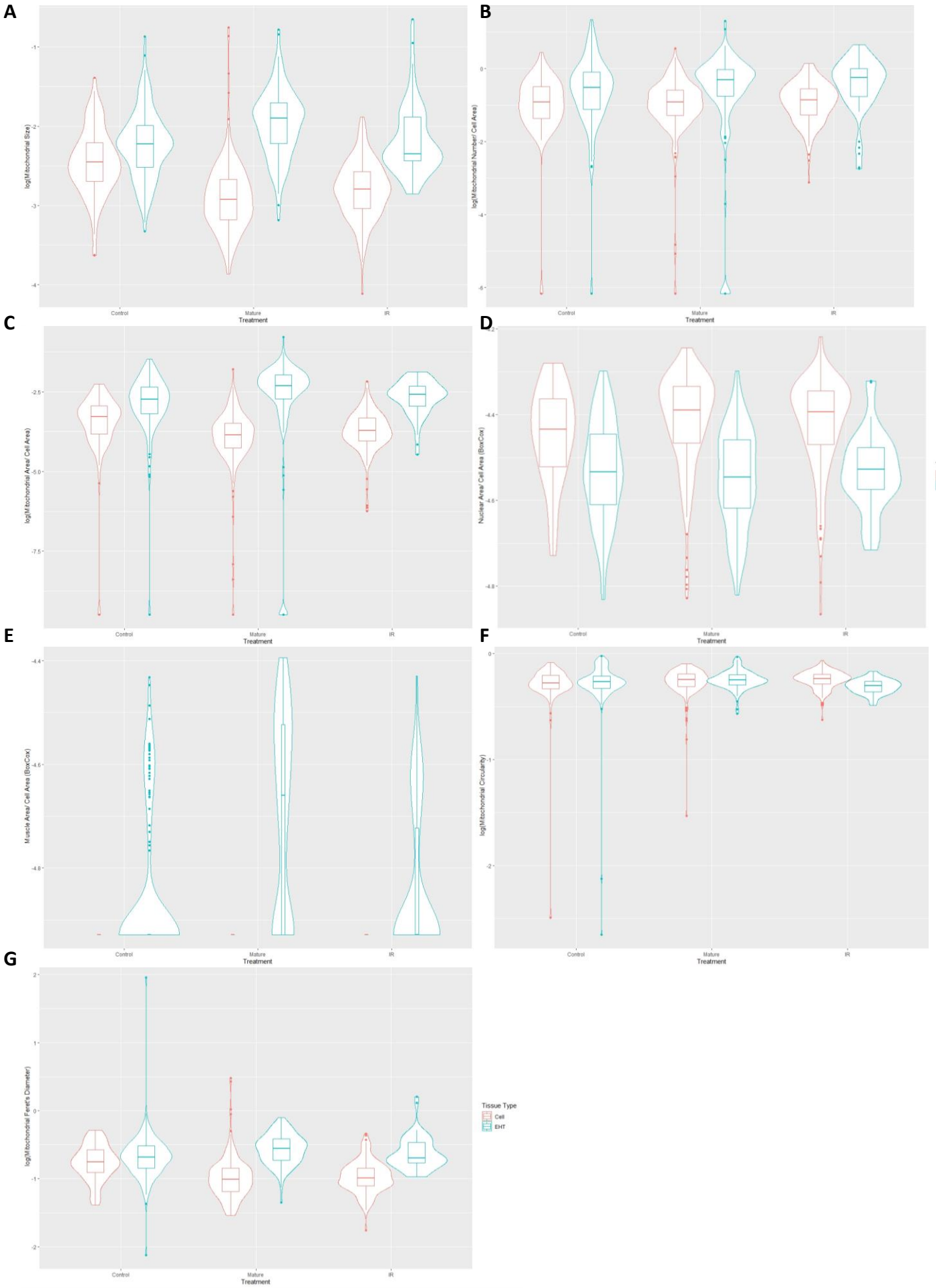


***Figure 9**: Graphical representation of transformed data with R. Red, Monolayer Cells; Blue, EHT. Data plotted against treatment. Violin plots are overlayed with boxplots showing the median and interquartile ranges. A, Mitochondrial Size ($\mu m^{2)}$; B, Mitochondrial Number; C, Mitochondrial Area/Cell Area; D, Nuclear Area/Cell Area; E, Muscle Area/Cell Area; F, Mitochondrial Circularity; G, Mitochondrial Feret's Diameter (µm)*

Quantitative Data – Graphical Representation

Figure 8 shows the graphical representation from R for each of the parameters measured. With the exception of those displaying Mitochondrial Circularity and Mitochondrial Feret's Diameter, all the graphs showed clear differences between Cells and EHT.

Three sets of correlation graphs (Figures 10-12) were plotted to compare Mitochondrial Size, Mitochondrial Area and Mitochondrial Number. The correlation coefficients and corresponding P-values, regression coefficients and R^2 were calculated (Tables 6-8) as well as comparisons of some of the correlations (Table 9). Correlation coefficients (R values) can be converted into z-scores and then used to compare correlations, this was done using an online calculator[120] based on methods in Fisher[121]. This method can only be used to compare correlations from independent samples, not the same sample sets with different parameters, so only correlations from different sample sets were compared.

The correlations were statistically significant even though the fit (R^2) was low because the number of data points were high. Similarly, the corresponding z-scores were compared and shown to be significantly different even with low R^2 values. However, there were many other factors affecting the size, number and total area of mitochondria, causing the low R^2, so they could not be used to predict each other. Instead, the regression lines suggest trends only. One of the factors that caused poor fit to the regression line is heterogeneity within each well of cells or EHT. When culturing, this heterogeneity could be seen as cells in different areas of the wells started to beat at different times. It is also likely that different areas of the EHT matured at different rates as the areas around the posts did not contract as strongly as the sections between them. As the slicing was done by the Dunn School it was not possible to determine any correlation between location of cells and maturity, but it would be useful in future projects involving EHT to spend time

with the slicing technicians to determine a protocol for correlating maturity and distance from the posts.

There was a positive correlation for both Mitochondrial Number (Figure 10) and Size (Figure 11) to Mitochondrial Area but a slight negative correlation for Number to Size (Figure 12). Separating the data by treatment type provides further insight. The Control and IR graphs showed similar trends, while the Mature graphs differed, suggesting oleic acid drove changes to mitochondria which the insulin resistance protocol then reversed. The negative correlation for IR EHT in Size to Area (Figure 11) was likely caused by unhealthy swollen mitochondria.

Culturing as EHT and treating with oleic acid each drove changes to the mitochondria but created a tension between increasing Number and Size. In the Size to Area correlation (Figure 11), the EHT data had a lower regression coefficient than the Cells, so the increase in Mitochondrial Size was less for a given increase in Mitochondrial Area. This suggested culturing as EHT drove an increase in Mitochondrial Area by something other than size. The Number to Area correlation (Figure 10) suggested this was Number, as the regression coefficients of Control Cells and Control EHT were similar and positive. Furthermore, the Number to Size correlation (Figure 12) for all EHTs showed a greater negative correlation than it did for Cells.

The exception to this was the Mature correlation graph which suggested the oleic acid treatment acted to return the Mature EHT regression line so it was parallel to the Mature Cells, however the correlation coefficient and corresponding P-value did not support this. For the Size to Area correlation (Figure 11), the regression coefficients of the Mature graph were greater than Control, suggesting oleic acid treatment was increasing Mitochondrial Size. In the Number to Area correlation, the Mature EHT had a lower

regression coefficient than Control EHT suggesting the oleic acid temperd the increase in Number. Interestingly, the Mature Cells and Control Cells had similar coefficients.

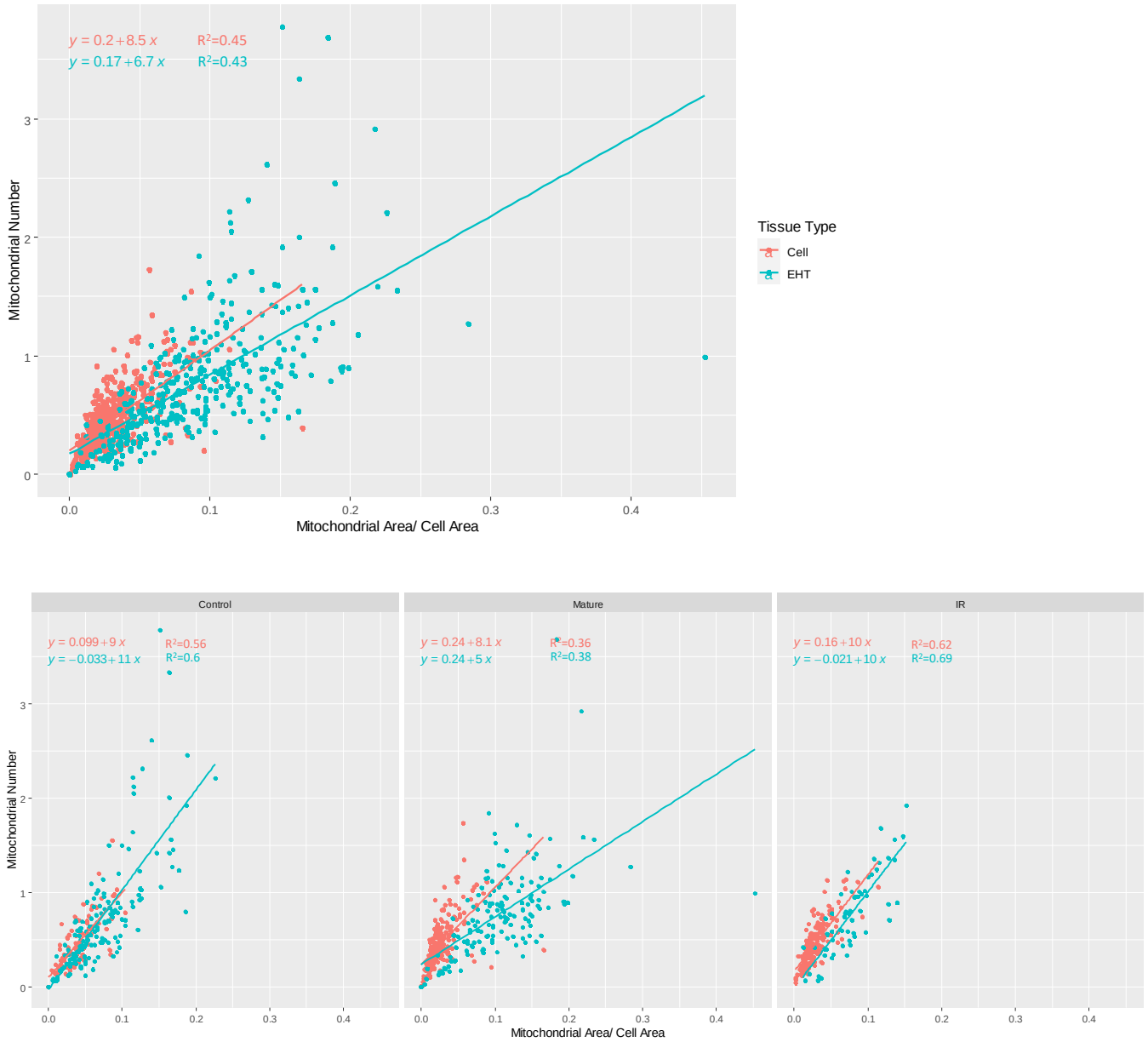


Figure 10 *: Correlation graphs of Mitochondrial Number to Mitochondrial Area/Cell Area. A, all data; B. separated by Treatment. Red, Monolayer Cells; Blue, EHT*

***Table 6**: Correlation and regression coefficients of Mitochondrial Number to Mitochondrial Area/Cell Area.*

		all	ctrl	m	IR
Cells	Regression	8.5	9	8.1	10
	Correlation	0.67	0.75	0.6	0.78
	p-value	$< 2.2\ e^{-16}$	$< 2.2\ e^{-16}$	$< 2.2\ e^{-16}$	$< 2.2\ e^{-16}$
	R^2	0.45	0.56	0.36	0.62
EHT	Regression	6.7	11	5	10
	Correlation	0.66	0.77	0.62	0.83
	p-value	$< 2.2\ e^{-16}$	$< 2.2\ e^{-16}$	$< 2.2\ e^{-16}$	$< 2.2\ e^{-16}$
	R^2	0.43	0.6	0.38	0.69



***Figure 11**: Correlation graphs of Mitochondrial Size to Mitochondrial Area/Cell Area. A, all data; B. separated by Treatment. Red, Monolayer Cells; Blue, EHT*

***Table 7**: Correlation and regression coefficients of Mitochondrial Size to Mitochondrial Area/Cell Area.*

		all	ctrl	m	IR
Cells	Regression	1.1	0.77	1.6	0.56
	Correlation	0.55	0.36	0.64	0.42
	p-value	$< 2.2\ e^{-16}$	0.00034	$< 2.2\ e^{-16}$	$2.8\ e^{-9}$
	R^2	0.31	0.17	0.42	0.17
EHT	Regression	0.39	0.069	0.62	-0.78
	Correlation	0.22	0.011	0.39	-0.34
	p-value	$1.9\ e^{-5}$	0.9	$5.7\ e^{-7}$	0.0081
	R^2	0.87	0.003	0.26	0.12

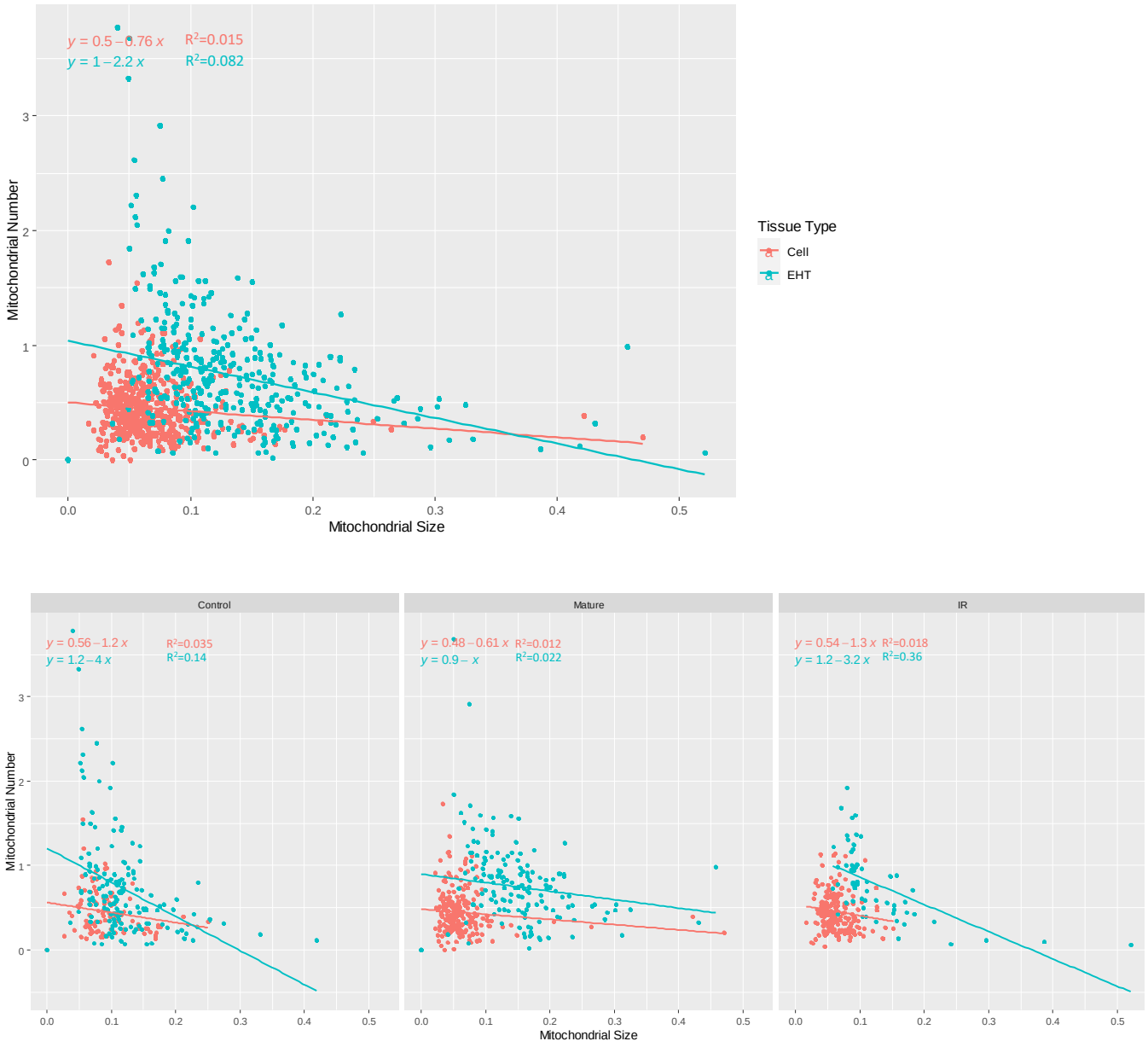


***Figure 12**: Correlation graphs of Mitochondrial Number to Mitochondrial Size. A, all data; B. separated by Treatment. Red, Monolayer Cells; Blue, EHT*

***Table 8** : Correlation and regression coefficients of Mitochondrial Number to Mitochondrial Size.*

		all	ctrl	m	IR
Cells	Regression	-0.76	-1.2	-0.61	-1.3
	Correlation	-0.15	-0.29	-0.13	-0.13
	p-value	0.00069	0.0046	0.046	0.065
	R^2	0.015	0.035	0.012	0.018
EHT	Regression	-2.2	-4	-1	-3.2
	Correlation	-0.4	-0.42	-0.4	-0.6
	p-value	$2.3\ e^{-15}$	$6.8\ e^{-8}$	$4.1\ e^{-7}$	$5.4\ e^{-7}$
	R^2	0.082	0.14	0.022	0.36

***Table 9**: Comparison of correlation coefficients: z-scores and P-values.*

Parameters Compared	Treatment/Cell type Compared	Z-score		P-value
Mitochondrial Number to Mitochondrial Area/Cell Area	Control EHT to Control Cells	-0.3618		0.7175
	Mature EHT to Mature Cells	0.3063		0.7593
	Mature EHT to Control EHT	-2.567		0.0102
Mitochondrial Size to Mitochondrial Area/Cell Area	Control EHT to Control Cells	2.7940		0.005
	Mature EHT to Mature Cells	3.331		0.0009
	Control Cells to Mature Cells	-3.120		0.0018
	Control EHT to Mature EHT	-3.511		0.00045
Mitochondrial Number to Mitochondrial Size	All EHT to All Cells	-3.992		0.000065
	Control EHT to Control Cells	1.139		0.2548
	Mature EHT to Mature Cells	2.813		0.0049

Quantitative Data – Statistical Tests - Parametric

The experimental design had two variables to be investigated (Tissue Type and Treatment) and a third random variable (Sample Name). In R, a simple model was created to control for the random variable and allow for two-factor analysis of the data (all R code is presented in Appendix 4). Subsequently, Two-Way ANOVA was performed to assess for population differences between Tissue Type and Treatment. For the majority of parameters, the ANOVA tests showed the Tissue Type factor to have a significant effect on differences in population but not the Treatment factor.

We wanted to know if there was a difference within both Cells and EHT between Control and Mature and between Mature and IR. For multiple comparisons, we wanted to test between two samples which had only one difference in protocol. Between the Control and Mature protocols, there was only the difference of the oleic acid step. Between Mature and IR protocols, only the high insulin and palmitate step was different. However, as both these steps were different between Control and IR, we were not interested in a pairwise comparison between these samples. To further clarify the result seen in the ANOVA, we wanted to know specifically if there was a difference between Mature EHT and Mature Cells. So, multiple comparisons on the simple model created in R were performed using the estimated marginal means (emmeans package) with a Tukey method of P-value adjustment.

Quantitative Data – Statistical Tests – Non-parametric

As previously discussed, Muscle Area and Nuclear Area required non-parametric tests. An Aligned Rank Transform was performed prior to an ANOVA.

For the non-parametric multiple comparisons, the Wilcoxon test was applied (Wilcoxon rank sum test with continuity correction and a holm method of P-value adjustment). The same samples were compared as for the parametric equivalent, between: Cell Control and Mature; Cell Mature and IR; EHT Control and Mature; EHT Mature and IR; and between EHT Mature and Cells Mature.

Because the graphs suggested a greater distribution of values in the more mature samples compared to less mature, a test was used to see if this difference in variance was statistically significant, separate to the multiple comparison tests that compared population averages. The Ansari-Bradley (AB) test was used as it is a non-parametric, robust equivalent to the more well-known F-test. P-value adjustments were done using p.adjust and a Holm method.

Quantitative Data – Results

Mitochondrial Size

Figures 7/8/9A show the data for Mitochondrial Size, illustrating that the average size of the mitochondria in EHT was slightly greater than in Cells (P-value < 0.0001). The graphs specifically showed this in the case of Mature EHT over Mature Cells (P-value < 0.0001). The distribution was greater in Mature EHT compared to Mature Cells (AB test P-value < 0.0001).

The apparent greater size of mitochondria in Mature EHT population over Control EHT seen in the graph was statistically significant but there was no significant difference in distribution between these two sample sets. When comparing Mature EHT and IR EHT, there was no significant difference in means or distribution.

***Table 10**: Statistical analysis for Mitochondrial Size with P-values for each statistical test. The tests (from top down) were: Two-way ANOVA, estimated marginal means pairwise equality test and an Ansari-Bradley pairwise variance equality test with Tukey P-value adjustment method for the equality tests. P < 0.05 was considered statistically significant and are represented in **bold**.*

ANOVA	All	Tissue Type Factor	Treatment Factor		
	0.000694	**$1.815e^{-9}$**	**0.6249**		
Multiple Comparisons (Mean)	Cell		EHT		Cell : EHT
	Control : Mature	Mature : IR	Control : Mature	Mature : IR	Mature
	0.0142	0.7101	**0.0413**	0.1110	**<0.0001**
Multiple Comparisons (Variance)	Cell		EHT		Cell : EHT
	Control : Mature	Mature : IR	Control : Mature	Mature : IR	Mature
	0.03852	0.2284	0.6116	0.07746	**$9.691e^{-5}$**

Mitochondrial Number

Figures 7/8/9B show the data for Mitochondrial Number. EHT had a wider distribution than Cells, and a slightly greater mean compared to Cells (P-value < 0.001). The difference in means between Mature EHT and Mature Cells was not significant (P-value = 0.0749), however there was a significant difference in distribution between these two sample sets (AB test P-value < 0.0001). There was no difference between Control EHT and Mature EHT, or between Mature and IR EHT, in either means or distribution.

Table 11: *Statistical analysis for Mitochondrial Number with P-values for each statistical test. The tests (from top down) were: Two-way ANOVA, estimated marginal means pairwise equality test and an Ansari-Bradley pairwise variance equality test with Tukey P-value adjustment method for the equality tests. P < 0.05 was considered statistically significant and are represented in* ***bold****.*

ANOVA	All	Tissue Type Factor	Treatment Factor		
	0.1873	**0.0001503**	0.07330		
Multiple Comparisons (Mean)	Cell		EHT		Cell : EHT
	Control : Mature	Mature : IR	Control : Mature	Mature : IR	Mature
	0.9953	0.8699	0.9950	0.4243	0.0749
Multiple Comparisons (Variance)	Cell		EHT		Cell : EHT
	Control : Mature	Mature : IR	Control : Mature	Mature : IR	Mature
	0.3040	0.8912	1.0	1.0	**$2.333e^{-6}$**

Mitochondrial Area

Figures 7/8/9C show Mitochondrial Area as a proportion of cell area, where EHT had a wider distribution and a greater average than Cells. The ANOVA showed tissue type as a significant factor (Table 12) and the difference between Mature Cells and Mature EHTs was also significant (P-value = 0.0001). The distribution was also significantly different (AB test P-value < 0.0001). There was no difference between the groups within each cell type.

Table 12: *Statistical analysis for Mitochondrial Area with P-values for each statistical test. The tests (from top down) were: Two-way ANOVA, estimated marginal means pairwise equality test and an Ansari-Bradley pairwise variance equality test with Tukey P-value adjustment method for the equality tests. P < 0.05 was considered statistically significant and are represented in* ***bold****.*

ANOVA	All	Tissue Type Factor	Treatment Factor		
	0.02592	**$2.732e^{-13}$**	0.1854		
Multiple Comparisons (Mean)	Cell		EHT		Cell : EHT
	Control : Mature	Mature : IR	Control : Mature	Mature : IR	Mature
	0.1057	0.5713	0.2825	0.9809	**0.0001**
Multiple Comparisons (Variance)	Cell		EHT		Cell : EHT
	Control : Mature	Mature : IR	Control : Mature	Mature : IR	Mature
	0.03546	0.09174	0.2547	0.5622	**$2.2e^{-13}$**

Nuclear Area

Figures 7/8/9D show Nuclear Area and that the data had a more skewed distribution, with many 0 value images. As the intention was to measure the nuclei as a proportion of total cell volume, where no nuclei were visible this proportion was 0. Even though it was not possible for an entire cell to be missing a nucleus, images of individual sections would not be representative of the entire cell, and some may have lacked nuclei. These images may have been from cells with smaller nuclei in comparison to the cytoplasmic area such that no part of the nucleus was included in the standard image, however this was still a valid result. It was only when the data from all the images for a sample were gathered that the results were representative of the cells in that sample. If the "0 value" images were not included, it would have given an over-estimation of the ratio between nuclear area and cell area. Therefore, values of 0 for individual images needed to be included in the analysis to avoid selection bias. The Nuclear Area was significantly less in EHT compared with Cells with the ANOVA confirming Tissue Type was a significant factor (Table 13). There was a significant difference between population averages for Mature EHT and Mature Cells, which was confirmed by both an emmeans and a Wilcoxon P-value ≤ 0.0001. Similarly, there was also a difference between Control and Mature cells. As the parametric test (emmeans) had an increased likelihood of Type1 error and was close to the P-value cut off for significance of 0.05 (0.0341), the non-parametric test was of particular importance. In this case it supported the emmeans result with a P-value of 0.0023. Mature EHT had a slightly lower average and a more skewed distribution than Control EHT, however, the differences were not significantly different (Wilcoxon P-value = 0.5804, emmeans P-value = 0.4352; AB test P-value = 0.1358). Mature EHT also

had a slightly lower average and a more skewed distribution than IR EHT, however neither were significant.

Table 13: *Statistical analysis for Nuclear Area with P-values for each statistical test. The tests (from top down) were: Two-way ANOVA, an ART followed by two-way ANOVA, estimated marginal means pairwise equality test with a Tukey P-value adjustment, a Wilcoxon rank sum test with Holm P-value adjustment and an Ansari-Bradley pairwise variance equality test with Tukey P-value adjustment. For non-parametric tests, P < 0.05 was considered statistically significant and for parametric tests, P < 0.01 was considered statistically significant. P-values representing statistical significance are in* ***bold****.*

ANOVA		All	Tissue Type Factor	Treatment Factor		
	Parametric	**0.005329**	**$<2.22e^{-16}$**	0.4351		
	Non-parametric	**$6.799e^{-6}$**	**$<2.22e^{-16}$**	**$1.143e^{-10}$**		
Multiple Comparisons (Mean)		Cell		EHT		Cell : EHT
		Control : Mature	Mature : IR	Control : Mature	Mature : IR	Mature
	Parametric	0.0341	0.1821	0.4352	0.6058	**0.0001**
	Non-parametric	**0.0023**	0.1652	0.5804	0.6959	**$<2.0e^{-16}$**
Multiple Comparisons (Variance)		Cell		EHT		Cell : EHT
		Control : Mature	Mature : IR	Control : Mature	Mature : IR	Mature
		1	1	0.1358	0.07314	0.4046

Muscle Area

Figures 7/8/9E show Muscle Area, this parameter showed the most dramatic differences. There was no muscle area in any of the Cell samples and so multiple comparison tests to compare between Cell values were not run, the zero results making comparisons inappropriate. However, the '0 value' data is still a result so a two-way ANOVA to analyse within EHT and between Cells and EHT, along with multiple comparisons between Cells and EHT, were completed. As expected, the ANOVA showed Tissue Type to be a significant factor (Table 14). More interestingly the ANOVA also showed Treatment to be a significant factor. The difference in averages for Mature EHT and Mature Cells was

significant (Wilcoxon P-value < 0.0001, emmeans P-value = 0.0001), as was the difference in distribution (AB test P-value < 0.0001). The Mature EHT distribution was least skewed as it had the fewest 0 values (AB test P-value < 0.0001 compared with Control EHT, n.s. compared with IR EHT) and the average muscle area in Mature EHT was significantly greater than that in Control and IR EHT (Wilcoxon P-value < 0.0001, emmeans P-value < 0.001 vs Control; Wilcoxon P-value < 0.0001, emmeans P-value < 0.01 vs IR).

Table 14: *Statistical analysis for Muscle Area with P-values for each statistical test. The tests (from top down) were: Two-way ANOVA, an ART followed by two-way ANOVA, estimated marginal means pairwise equality test with a Tukey P-value adjustment, a Wilcoxon rank sum test with Holm P-value adjustment and an Ansari-Bradley pairwise variance equality test with Tukey P-value adjustment. For non-parametric tests, P < 0.05 was considered statistically significant and for parametric tests, P < 0.01 was considered statistically significant. P-values representing statistical significance are in* ***bold****.*

ANOVA		All	Tissue Type Factor	Treatment Factor		
	Parametric	**0.0006096**	**$3.718e^{-16}$**	**0.0002405**		
	Non-parametric	**$<2.22e^{-16}$**	**$<2.22e^{-16}$**	**$<2.22e^{-16}$**		
Multiple Comparisons (Mean)		Cell		EHT		Cell : EHT
		Control : Mature	Mature : IR	Control : Mature	Mature : IR	Mature
	Parametric	N/A	N/A	**0.0002**	**0.0072**	**0.0001**
	Non-parametric	N/A	N/A	**$5.7e^{-12}$**	**$2.9e^{-6}$**	**$<2e^{-16}$**
Multiple Comparisons (Variance)		Cell		EHT		Cell : EHT
		Control : Mature	Mature : IR	Control : Mature	Mature : IR	Mature
		N/A	N/A	**$1.5228e^{-5}$**	0.3853	**$<2.2e^{-16}$**

Mitochondrial Circularity

Figures 7/8/9F show Mitochondrial circularity. There were no significant differences in average circularity, again the distribution of the Mature EHT was significantly less skewed than that of the Mature Cell and the Control EHT (AB test P-values are <0.01 and <0.05 respectively, Table 15).

Table 15: *Statistical analysis for Mitochondrial Circularity with P-values for each statistical test. The tests (from top down) were: Two-way ANOVA, estimated marginal means pairwise equality test and an Ansari-Bradley pairwise variance equality test with Tukey P-value adjustment method for the equality tests. P < 0.05 was considered statistically significant and are represented in* ***bold****.*

ANOVA	All	Tissue Type Factor	Treatment Factor		
	0.05654	0.6144	0.1560		
Multiple Comparisons (Mean)	Cell		EHT		Cell : EHT
	Control : Mature	Mature : IR	Control : Mature	Mature : IR	Mature
	0.4953	0.5928	0.2599	0.1384	0.4668
Multiple Comparisons (Variance)	Cell		EHT		Cell : EHT
	Control : Mature	Mature : IR	Control : Mature	Mature : IR	Mature
	0.8864	0.19216	**0.02172**	0.4610	**0.009852**

Feret's Diameter of Mitochondria

Figures 7/8/9G show Feret's Diameter, where mitochondria in EHT had a slightly greater Feret's diameter than those in Cells (P-value < 0.0001; Table 16). This was driven by a significantly greater Feret's Diameter in the Mature EHT compared with that in Cells (P-value < 0.001). There was also a significant difference in distribution between Mature Cells and Mature EHT (AB test P-value < 0.05). There were no within-group differences in this parameter.

Table 16: *Statistical analysis for Mitochondrial Feret's Diameter with P-values for each statistical test. The tests (from top down) were: Two-way ANOVA, estimated marginal means pairwise equality test and an Ansari-Bradley pairwise variance equality test with Tukey P-value adjustment method for the equality tests. P < 0.05 was considered statistically significant and are represented in* ***bold****.*

ANOVA	All	Tissue Type Factor	Treatment Factor		
	0.0108	**$1.163e^{-5}$**	0.7753		
Multiple Comparisons (Mean)	Cell		EHT		Cell : EHT
	Control : Mature	Mature : IR	Control : Mature	Mature : IR	Mature
	0.0696	0.9612	0.1637	0.4271	**0.0005**
Multiple Comparisons (Variance)	Cell		EHT		Cell : EHT
	Control : Mature	Mature : IR	Control : Mature	Mature : IR	Mature
	0.06506	0.06506	0.9359	0.5652	**0.03948**

Discussion

We know from previous work that metabolic changes occur in hiPSC-CMs matured by oleic acid or culture as 3D EHTs with a switch from glycolysis towards fatty acid oxidation. Induction of insulin resistance results in a further decrease in glycolysis with a likely increase in fatty acid oxidation (although not shown to be significant in preliminary data) and increased lipid accumulation. The aim of this study was to assess if there were also structural changes and if these were quantifiable.

Previously produced confocal images (Figure 2C, produced by Ujang Purnama) show sarcomere development occurs within the EHT. Similarly, Mannhardt et al.[122] contains a range of confocal images showing maturation of sarcomeres comparable to those seen in the Carr lab. While higher magnification confocal images show structures resembling sarcomeres, there is a lack of detail. This can be provided using TEM however few studies have used this technique for EHT. Mannhardt et al.[122] and Katare et al.[123] show similar cellular structures to the images produced in this project, although our images show more mitochondria and on average fewer well organised sarcomeres. This may be an example of the limitation of 'representative' images, or it may be due to differences in maturation methods. The EHTs shown by Katare et al.[123] were prepared using isolated cardiomyoctyes from neonatal rats which are thought to be more mature than the hiPSC-CMs used here. They also use mechanical stretch which is likely to drive maturation by sarcomere development rather than metabolic changes. Mannhardt et al.[122] use stem cell derived cardiomyocytes, with a similar differentiation protocol to that used by the Carr lab, however they start with human embryonic stem cells rather than hiPSCs and have a longer culture time post casting. The TEM image shown is from an EHT maintained for 35 days; substantially longer than those used in this project. It is known that extended time

in culture induces maturation [85,122] but the work of the Carr group has shown that stimulation of fatty acid oxidation can induce maturation in a shorter period of time. Mannhardt et al. were focussing on the analysis of contractile function and did not make any changes to the culture medium. It may be that the addition of oleic acid induces changes to mitochondria but does not drive sarcomeric maturation to the extent seen after the longer culture time. More recent work from the same group has looked at the link between improved contractile function and increased fatty acid oxidation[124]. They compared hiPSC-CM in monolayer culture and in EHT matured for 21-45 days and saw maturation of mitochondrial structure in EHT using TEM. They did not add fatty acid to the culture medium but showed increased fatty acid oxidation with prolonged culture. They saw increased mitochondrial DNA in EHT compared with monolayer culture but did not produce any quantitative data from the TEM images. This suggests that the prolonged culture produced a comparable maturation of metabolism to that seen with addition of oleic acid to the culture medium, with increased sarcomeric maturation. However, the longer time in culture increases both time and cost to the experiments and, as always, the most appropriate maturation method will depend on the experimental question.

Our images allowed visual identification of most of the common cellular structures in cardiomyocytes and we were able to quantify nuclear, muscle and mitochondrial areas as a proportion of cell area, and mitochondrial size, circularity and maximum diameter. We were unable to quantify the dilation of cristae in mitochondria due lack of definition in some mitochondria[125]. The mitochondria in cardiomyocytes have very high-density cristae. In TEM images of rat mitochondria at low magnifications, the closely packed cristae can be indistinct as seen in (Figure 5a and c) but densely packed cristae can be

seen at higher magnification (Figure 5b and d). As mitochondrial membranes appear darker than the matrix, this is a good indicator of membrane density at magnifications where cristae cannot be distinguished: lightly stained undefined mitochondria are likely to be immature, dark stained undefined mitochondria are likely to be mature. This is illustrated by the top image in Figure 5. Separating mitochondrial populations by maturity would be of use in our data sets as we have both 'dark' and 'light' mitochondria and it would provide another method of establishing cell and metabolic maturity. The difficulty is in identifying the differences as staining is not uniform between samples, so 'dark' and 'light' are subjective terms with the corresponding lack of consistency. An alternative would be to reimage the grids using a higher magnification which should allow for better analysis of the mitochondrial cristae, differentiating between the densely and less densely packed cristae and potentially providing quantification of dilation. This would however be time consuming and was not feasible within the constraints of this project.

It was not possible to separate out different populations of mitochondria within the cultured cells. In TEM literature, these populations have been identified by location within the organised structure of the cardiomyocytes[94]. As the cultured cells were still maturing, their structure was not yet consistently organised, and so could not be reliably used for identification of mitochondrial populations. Little is known about the formation of mitochondrial populations during cardiomyocyte development. However, it has been suggested that they form during the maturation of cardiomyocytes from the post-natal to adult stage, coinciding with the metabolic switch, increased cristae density and increased mitochondrial mass[126]. Given the rest of the ultrastructure in the cultured cells had not developed to a fully adult stage, it is likely that the mitochondria populations had also not yet formed and so we were not able to identify them.

It may be possible to use the cristae morphology to indicate the initial stages of formation of the mitochondrial populations. However, literature describes the lamelliform and tubular cristae in 3D scanning electron microscopy[127], rather than transmission electron microscopy. This is because the differences in morphology are clearer in 3D. It would be interesting to see if the differences in morphology of cristae seen in our images correlate to lamelliform and tubular cristae.

As the cellular substructure of our EHTs was still forming, it was unlikely that identification of T-tubules would be possible. Indeed, it is unusual to identify these structures in hiPSC-CMs[85]. This does not mean that they are absent, rather the organisation of T-tubules develops alongside sarcomere and sarcomeric reticulum development. T-tubules initially have disorganised orientations but in adult tissue the T-tubules orientate perpendicular to the direction of muscle filaments. This means that even in mature tissue, identification of T-tubules can be difficult as usually it is necessary to slice along the longitudinal axis of the myofilaments which creates a cross-section of the T-tubules. This makes them difficult to distinguish from small vesicles. This issue is encountered by Mannhardt et al. who describe 'tubular structures…in close proximity to Z-lines'. We were unable to visualise any similar structures in EHTs, however we do see T-tubules in the rat images provided by Dr. Lisa Heather. It is likely that the previously mentioned longer culture time of EHTs by Mannhardt et al.[122] enabled them to identify possible T-tubule structures.

It has been demonstrated in this project that as the cells mature the Nuclear Area gets smaller. This is because as cardiomyocytes mature the nuclei grow at a slower rate than the cell, decreasing the nuclear to cell area ratio [128]. However, even in the most mature cells (Mature EHT), Nuclear Area was still a factor of ten greater than in the rat images,

indicating the EHTs could still be matured further. Cardiomyocytes in adult tissue are often binucleated due to nuclear division without cellular division[90], but this was not seen in our Mature EHTs. It is known that CMs proliferate immediately after birth but as the cells mature they soon stop proliferating and the heart increases in size through hypertrophy. It is therefore likely that the decrease in nuclear area as a proportion of cell area in more mature cells was due to increased cell size and constant nuclear size rather than a decrease in nuclear size. In this project the increased tension in EHT may have increased the cell size and so caused the decreased Nuclear Area, however oleic acid did not appear to cause a further decrease in Nuclear Area suggesting it had no effect on cell size.

Oleic acid did increase the amount of structured muscle in EHT (supporting confocal images taken by Ujang Purmana). The difference in variance within the muscle data supported the suggestion that some cells were maturing faster than others. The Muscle Area decreased in IR EHT compared to Mature EHT which supports this protocol producing a good model for insulin resistant muscle as insulin resistant mice have been shown to have lower muscle fiber density[129].

It is worth noting that this muscle area data refers to organised filaments. As individual filaments have fine structure, and actin filaments are important for cellular functions other than muscle (e.g. cytoskeleton[130] and vesicle transport[131]), it is only when these filaments begin to line up parallel to each other that we can confidently identify them as muscle related structures. The monolayer cells were beating, although with a less forceful 'twitching' of cells rather than pulling against posts as in EHT, and therefore must contain muscle filament. This lower force requirement in 2D may not have been enough to encourage the organisation of filaments necessary for them to be visible.

The Mitochondrial Area was greater in EHT, as we would expect given the greater fatty acid oxidation seen in Lopez et al[86]. This was a result of both a greater Mitochondrial Number and Size. Interestingly, when oleic acid was added to the EHT culture media, there was a further increase in mitochondrial size but no change in mitochondrial number. Previous work by the Carr group (Figure 2D) showed a greater increase in fatty acid oxidation induced by culture in EHT compared with 2D than that seen by addition of oleic acid to EHT culture. Therefore, it makes sense that 3D culture induced an increase in both mitochondrial size and number, but the further increase in fatty acid oxidation induced by addition of oleic acid could be accommodated by increased maturation of existing mitochondria.

Despite increasing in EHT, Mitochondrial Area was still somewhat lower than that seen in the rat cardiomyocytes, by a factor of three. However, published data show mitochondrial proportion of the cell as between that seen in our rat and EHT data, varying from 0.15 to 0.25[96–98]. This suggested the proportion of EHT cell area taken up by mitochondria was approaching that of mature tissue. For Mitochondrial Number, there were similar values for both the rat data and EHT.

Thus, by comparing only Mitochondrial Area and Mitochondrial Number (albeit from different species), one might conclude that there was little difference in mitochondrial maturation between EHT and *in vivo* tissue. However, looking at Mitochondrial Size, the average value for the rat tissue was five times greater than that for EHT suggesting that further maturation of the mitochondria was needed.

The graphs of correlations suggested that oleic acid was an important factor for increased mitochondrial size. Indeed, in human skeletal muscle, IF mitochondrial size has also been shown to be inversely associated with whole-body respiratory quotient (CO_2 produced/O_2

consumed). Whole-body respiratory quotient was used as the marker of whole-body relative lipid oxidation, with lower values indicating higher lipid, relative to glucose oxidation and was measured both during exercise and at rest[132]. This indicates that the metabolic switch from glycolysis to fatty acid oxidation in our cells was important for mitochondrial maturation.

The parameters used in this project to quantify mitochondrial shape were Circularity and maximum diameter (Feret's Diameter). Feret's diameter values were consistent across all cultured samples with the larger values for rat images explained by the concordant greater size. Circularity data showed that there was a reasonably consistent shape across all the cultured samples and the rat images. The values were consistent with those reported by Kalkhoran et al.[94], although they report slight but significant value differences in Circularity for different mitochondrial populations with SS and PN populations having Circularity of about 0.1 greater than IF. Importantly, Kalkhoran et al.[94] only used images of longitudinal slices, where the oblong shape of IF mitochondria can be measured.

Larger and more elongated cardiac mitochondria are generally considered to be more mature and, in combination with increased cristae density, there is a concordant increase in β-oxidation and Electron Transport Chain proteins[113]. It would be useful to further asses this maturation in the cultured cells by assessing the expression of key proteins involved in fatty acid oxidation and the Electron Transport Chain: fatty acid translocase FAT/CD36 and mitochondrial proteins such as Carnitine palmitoyltransferase 1 (CPT1), mitochondrial uncoupling protein 3 and subunits of electron transport proteins such as ATP synthase and Cytochrome Oxidase Subunit IV (COX4)[133]. In addition, oxygen

consumption by isolated mitochondria could be measured to assess mitochondrial function.

Culturing as EHT and with oleic acid are both designed to mature the CMs, but structurally they caused different changes. This is likely due to the mechanisms by which they induce maturation. Culturing as EHT changes how cells interact with each other (3D rather than 2D) and increases the tension in the cells and the force needed for contraction. This resulted in cellular changes and caused the changes seen in sarcomeres and nuclei. Culturing as EHT also caused an increase in mitochondrial number as well as size. The presence of more, smaller (compared to with oleic acid) mitochondria fits with those seen in PN and SS mitochondria.

In contrast, oleic acid drives the change from a metabolic direction, inducing a metabolic switch and causing mitochondrial maturation, as shown by an increase in size. Oleic acid only indirectly impacted sarcomere development due to the increased efficiency in fuel usage, which may increase the contractility of the cells, and there was no effect on nuclei.

The previous data on the Insulin Resistant cell model has shown an ablation of the insulin stimulated AKT response, a significant decrease in glucose consumption and an increase in lipid deposition (Figure 2). However, the quantitative analysis of TEM images in this project has shown only a decrease in muscle content, with no significant change in mitochondrial size or shape. This could be caused by the cumulative effect of the cells not being mature enough before the IR protocol, especially in terms of mitochondrial size and shape; a lag between the metabolic changes seen in previous data and structural changes caused by long term effects; and not quantifying cristae structure which could be affected faster than other structural features. Many of the ultrastructural defects associated with diabetic cardiomyopathy are due to chronic exposure to elevated fats and/or glucose.

Therefore the IR protocol may need to be modified to include longer exposure to the high insulin and palmitate levels and increasing the glucose concentration in the media. Recent work by the Carr group has shown that changes in the response to hypoxia in the diabetic rat heart seen by Prof Lisa Heather's group can be recapitulated in the IR iPSC-CM[134]. The rat model of Type 2 Diabetes used by the Heather group represents the early stages of the disease and analysis of the TEM images of rat cardiac tissue by the Heather group did not identify major changes in mitochondrial number or structure. This suggests that our model also represents the early effects of insulin resistance and it would be interesting to explore structural changes in a chronic model of the disease.

Conclusion

The aim of this project was to determine whether imaging the ultrastructure of the iPSC-CM as 2D (monolayer cells) and 3D (EHT), under various treatment conditions, would generate information to probe the changes induced. The quantification process developed in this project is laborious in comparison to the qualitative 'representative image' approach often taken with electron microscopy. While it could be argued that the effects of culturing as EHTs compared to monolayer cells was sufficiently obvious that quantification was unnecessary, this was not the case for the more modest Treatment effects. The effect of oleic acid on mitochondrial size, the importance of mitochondrial size in further maturation and the effect of IR on muscle content would not be clear had there only been qualitative analysis.

Although it was clear that the ultrastructure of the EHT was still much less organised than that of mature muscle, and that the cells had not developed either T-tubules or different mitochondrial populations, some maturation of mitochondrial size could be seen with the addition of oleic acid and there was clear damage to muscle formation induced by the

insulin resistant protocol. We had hoped to see the formation of mitochondrial networks in the mature tissue, but these were not particularly evident. Clearly further maturation is needed to produce a muscle structure that truly models that in the adult heart.

This project is part of a larger endeavour to create more mature models of cardiac tissue, both healthy and diseased, and to determine whether the models recapitulate changes seen in animal models, thereby providing a route to translation. Other groups have shown that prolonged culture in 3D[122], afterload[135], the induction of mechanical stretch and/or electrical pacing[136] increased structural maturation. It would be interesting to measure metabolic changes in these models and to see the effect of a combination of these techniques with oleic acid in the media. For an insulin resistant model, we showed here that the addition of palmitate for a week induced muscle damage and so long-term culture in this media may result in an undesired level of cell death. Diabetes is a chronic condition and the effect of insulin resistance on cardiomyocytes may take several weeks to develop. This may explain why we only saw subtle changes in IR-EHT data. For a model of chronic insulin resistance it may be necessary to adjust the level of nutrients to induce a more gradual change over a longer time. Indeed, for future projects it is likely that the combination of conditions for maturation and induction of disease, and the methods used to analyse the tissue produced, will vary with the complexity and nature of the question being asked. It is unlikely detailed statistical analysis of TEM images, as performed here, will form part of much of the future work unless the aim focuses on structural changes to the CMs or mitochondria.

Concluding Statements

Quantification of images is a time-consuming process, as analysis, whether drawing or grading, has to be done manually. While a grading system such as that used in the kidney (see Appendix 1) is fast, seconds per image compared to minutes or hours for TEM images, it is very subjective and only provides one parameter. The drawing method used to analyse the TEM images is far more time consuming, but it does create a more detailed data set.

The quantity of data within each TEM image varied greatly and determined the type of data that could be gathered. High magnification images do not allow for mitochondrial networking analysis, while lower magnification TEM images contain too much information to be able to use a simple grading method. For example, if we wanted to analyse quality of cristae using a grading method, we would need to use high magnification images (minimum x2500 magnification). In cardiac tissue specifically, the plane of slicing is important for determining changes in sarcomeric size and structure. Also important is separating the mitochondrial populations. These are both currently difficult to achieve in the cultured tissue, although it is hoped that as the process for maturing tissue *in vitro* improves the cellular structures will become more evident, allowing the different mitochondrial populations and the sarcomere orientation to be identified. Despite some limitations, the project has proved that quantification can highlight some differences in structure that could otherwise be missed, in this case the effect of oleic acid on mitochondrial size, and its importance to furthering the mitochondrial maturity in EHTs.

Appendix 1 -Diabetic nephropathy

[This work was undertaken as the baseline for a project with the Ashcroft group, but was discontinued following a move to the Carr group. Although far from complete it is included here as it also concerns structural changes induced in diabetes.]

Introduction

Diabetic nephropathy is a major cause of end stage renal disease (ESRD) and a significant drain on health care resources[137]. For patients with diabetes there is a 20-30% likelihood of developing kidney disease. Diabetic nephropathy statistics for ESRD vary by type of diabetes: T1DM patients have a 75% chance of developing ESRD 20 years post nephropathy diagnosis whereas for T2DM patients this is only around 20%. One proposed explanation of this discrepancy is that T2DM patients are generally diagnosed later in life and so death from other causes occur before ESRD develops. Clinical renal involvement tends to occur 15-25 years after initial onset of diabetes [138]. The initial symptoms of diabetic nephropathy for patients include: oedema of the ankles, feet and hands, haematuria, exhaustion, shortness of breath and nausea[139].

The major cause of diabetic nephropathy is hyperglycaemia which upsets the balance of synthesis and degradation of extracellular matrix components leading to mesangial alterations including mesangial matrix expansion (MME) and glomerular basement membrane (GBM) thickening[140]. Hyperglycaemia creates toxic by-products such as advanced glycosylated end products (AGEs) which increase TGF-β_1 signalling and cause MME by increasing matrix synthesis and decreasing matrix degradation[141]. In addition, hyperglycaemia activates the diacylglycerol-phosphate kinase C (DAG-PKC) pathway leading to GBM thickening[142]. Hyperglycaemia increases the activity of aldose reductase

(converting glucose to sorbitol), also leading to MME and GBM thickening. Family history of hypertension or CVD are risk factors for diabetic nephropathy. MME further increases systemic hypertension and blood pressure is directly related to glomerular pressure which is a cause of lesions and sclerosis[138]. MME also increases albuminurea and decreases glomerular filtration[138] while podocyte separation of GBM leads to increased proteinurea[140].

As hyperglycaemia is the main cause of physical changes in the glomeruli in diabetic nephropathy, the most important prevention and treatment is tight glycaemic control[138,143]. Control of blood pressure is also important to avoid increased glomerular pressure. The hyperglycaemia associated with Diabetes Mellitus exacerbates the effects of hypertension in the glomeruli by causing autoregulation of the microcirculation to malfunction. *In vitro* studies suggest a mechanism: small, repeated changes in pressure inside the glomeruli cause stretch-relaxation cycles which stimulate TGF-β_1 and mesangial matrix component production[144]. Dyslipidaemia and smoking are both risk factors in diabetic nephropathy[138,145]. Protein restriction in the early stages of diabetic nephropathy can slow disease progression by reducing glomerular filtration and proteinurea. However, in ESRD over-restriction of protein can increase morbidity and mortality[138].

Models of Diabetic Nephropathy

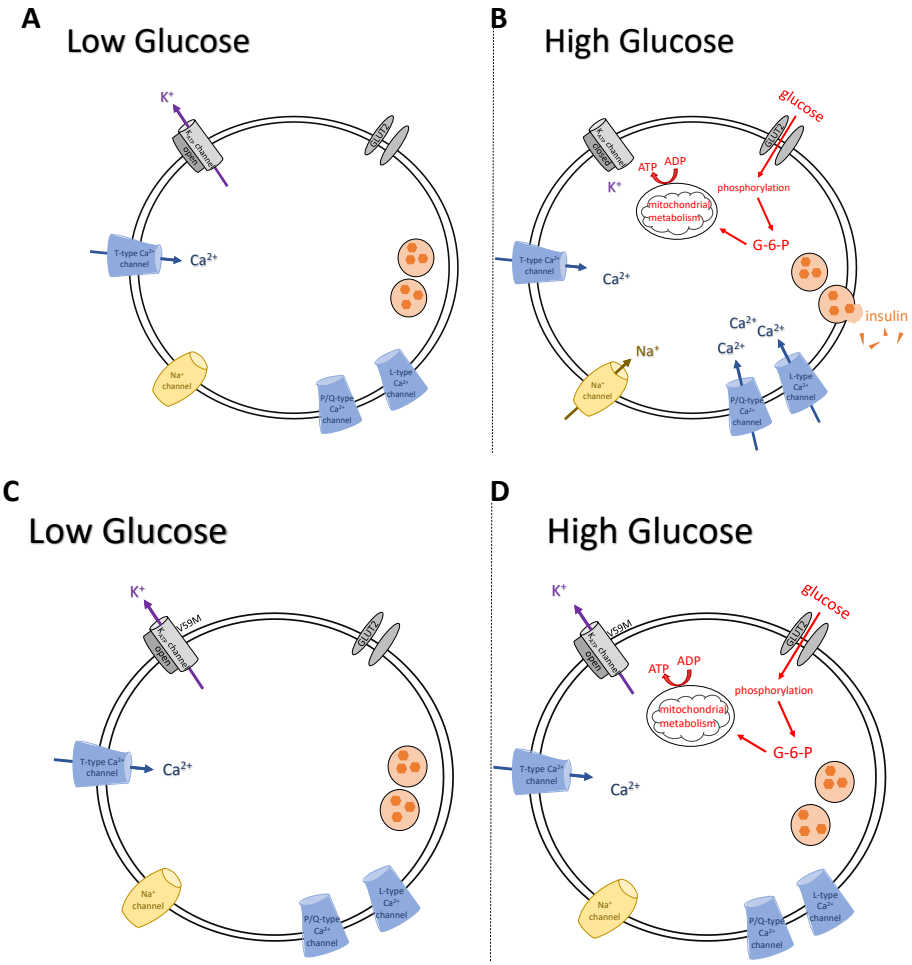
Mice are commonly used in research to model human disease as they are cost-effective with a relatively short life cycle. A historical focus of research using mice has led to a developed understanding of mouse genetics, good availability of tools for genetic manipulation and phenotyping, and a number of commercially available inbred strains to model many diseases.

Specific to diabetic nephropathy modelling, the Animal Models of Diabetic Complications Consortium has supported the research into finding good mouse models of diabetic nephropathy and standardising phenotyping. There are already many mouse strains that model MME but only a few are reported to show other features of diabetic nephropathy such as podocyte loss and advanced lesions[146,147]. A potential cause is the short life cycle of the mouse which means they do not live long enough to develop renal failure[148]. Also, it has been postulated that some features such as podocyte loss have been overlooked in the phenotyping of some strains. Finally, some inbred strains are resistant to diabetic nephropathy, including C57BL/6 which is a commonly used background for diabetic models[146].

Mouse model of Neonatal Diabetes

The Ashcroft lab developed a mouse model (βV59M) which separates hyperglycaemia and dyslipidaemia. The βV59M mouse model expresses a tamoxifen inducible K_{ATP} channel activating mutation (Kir6.2-V59M) in β-cells, under the rat insulin promoter (Rip-Cre-ER). With a healthy K_{ATP} channel, the channel is open in a low glucose environment, allowing potassium ions to flow out of the β-cells down the concentration gradient (Appendix 1 Figure 1A). Under high glucose conditions, the mitochondrial metabolism leads to the closure of the K_{ATP} channel, preventing the outflow of potassium ions and creating a small electrical potential across the membrane. This triggers a chain of voltage-gated ion channels, creating a high concentration of calcium ions inside the cell which cause insulin exocytosis (Appendix 1 Figure 1B). The V59M mutation in the K_{ATP} channel is considered an activating, gating mutation and prevents channel closure. So, when

activated, this mutation turns off insulin secretion, mimicking neonatal diabetes (Appendix 1 Figure 1C and D).



Appendix 1 Figure 1*: Mechanism of glucose stimulated insulin release in β-cells. A-B, β-cells without a mutation in K_{ATP} channel in high and low glucose respectively; C-D, β-cells with V59M mutation in the K_{ATP} channel in high and low glucose respectively.*

Data from Brereton et al. shows plasma glucose concentrations of > 20mM after tamoxifen injection compared to about 5 mM for controls. Diabetes can be reversed using sulphonylureas, which inhibit the K_{ATP} channel and promote insulin secretion, restoring normoglycaemia[149].

Diabetic nephropathy in βV59M mice as indicated by mesangial expansion.

Preliminary experiments conducted by Dr Maria Rohm using kidneys from diabetic βV59M mice showed signs of hyperfiltration, exceeded renal threshold, and increased levels of albumin and total protein in urine. Staining for fibrosis and inflammation/macrophage infiltration did not highlight any significant differences between control and diabetic mice. However, both assessments of glomeruli area/glomerular filtration and MME showed significant changes indicative of kidney disease.

Aims

As MME was more pronounced, we concluded this was the clearest indicator of diabetic nephropathy in the βV59M mouse model and could be used in future investigations. The aim was to further elucidate the extent to which this mouse model was susceptible to diabetic nephropathy and how this changed over the life span of the animals. If the model could be shown to reliably reproduce elements of diabetic nephropathy, it could be used to determine the specific impact of hyperglycaemia without the confounding factor of dyslipidaemia.

Methods

Animals

βV59M mice were generated as in Brereton et al. [149] Colonies were bred, maintained, induced and monitored (including blood glucose levels) as in Rohm et al.[150]

Kidneys

Removal from mice

Mice were sacrificed by cervical dislocation. The kidneys were removed by dissection and put directly into 10% Formaldehyde solution for fixing. After a minimum of 48 hours, they were transferred into 70% ethanol solution.

Imbedding in Paraffin

The kidneys were divided lengthways and placed in an imbedding cassette and then a tissue-transfer processor to dehydrate and perfuse with paraffin. Hot paraffin was poured into each cassette to cover the kidney and placed on a cold block to solidify.

Slicing

The wax blocks were frozen at -20°C. Slices of 0.2µm were placed onto slides using the Leica RM2255 Rotary Microtome.

Staining

Immersion steps with xylene and decreasing concentrations of ethanol hydrated the tissue which was then stained with 0.5% Periodic acid solution, Schiff's reagent and Mayer's hematoxylin. It was then dehydrated, and a cover slip fixed using DPX mounting media.

Microscopy and Analysis

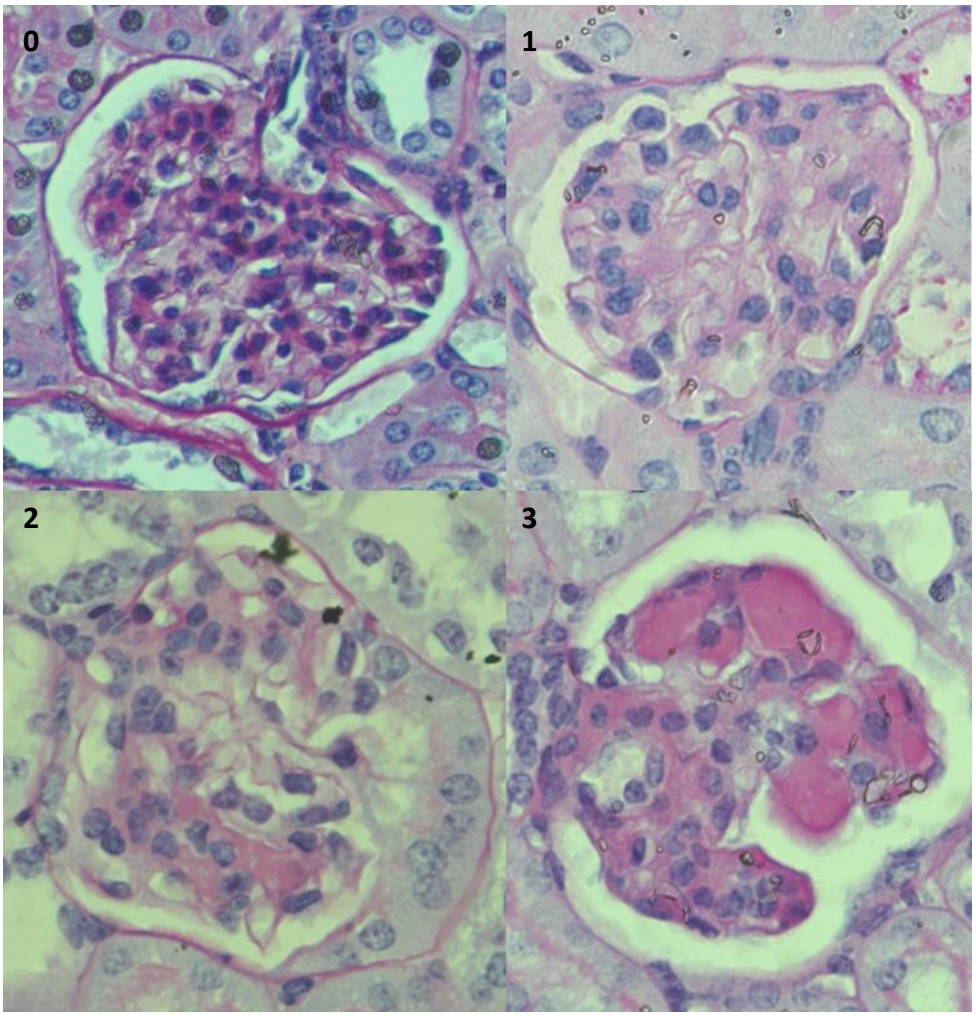
Stained slides were analysed using confocal microscopy. 20-30 glomeruli were analysed per mouse. Each glomerulus was given an MME score from 0-3 (Appendix 1 Figure 2).

Statistics

Data shown are mean ± standard error of the mean. Data point numbers and number of experiments are indicated in the figure legends. Significance was tested using T-test, One-way analysis of variance (ANOVA) or Two-way ANOVA with either Duckett's, Welch's, Bonferroni or Turkey *post hoc* tests as indicated. Results were considered statistically significant when $P<0.05$.

Results

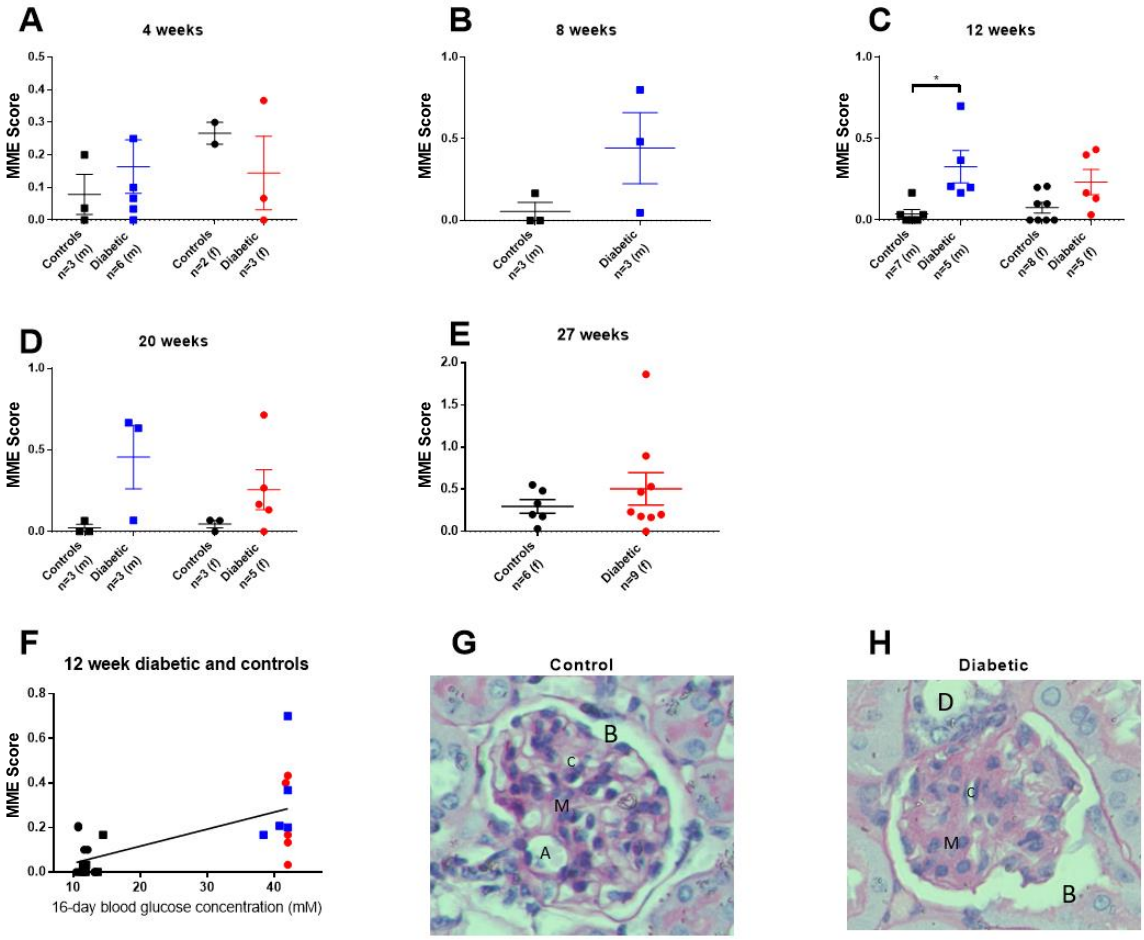
Kidneys were harvested from mice at various time-points after diabetes was induced by tamoxifen injection (x-week diabetic). The kidneys were stained using the PAS staining protocol for MME (see Methods). Each glomerulus was given an MME score based on the amount of PAS staining, principally the score relates to the number of nuclei that can fit into the areas of PAS staining that lack other structures (with a maximum score of three). However, the scoring was more subjective as the scorer also took into account the intensity of the staining comparative to the rest of the image as well as the total staining



Appendix 1 Figure 2: *Glycogen stained kidney slices were analysed and given an MME score from 0-3 based on the level of MME indicated by the areas of glomeruli stained pink and lacking other features. Images in the figure (labelled 0-3) are representative of glomeruli with said score.*

across the whole glomerulus. Consequently, training by an experienced scorer and practice was important before scoring any images to be included in results. It was also important to score some images multiple times to ensure consistency over time and blinding to avoid bias.

Significantly increased MME in kidneys from 12-week diabetic mice (Appendix 1 Figure 3C) was observed and there was a trend to an increase in 8-week



***Appendix 1 Figure 3**: Diabetic βV59M mice have kidney disease as indicated by increased mesangial expansion.*
*(A-E) Mice were culled x weeks post-tamoxifen injection. For each mouse, 20-30 glomeruli were given a score for mesangial expansion (MME) (see Appendix). Data are mean MME score for individual diabetic (coloured) and control (black) mice and mean values for each group of mice (horizontal bars) ±SEM. (*P<0.05, **P<0.01; T-test with Welch's correction.) (F) Linear regression of blood glucose concentration 16 days post injection (tamoxifen or control) and MME score for each mouse. Where blood glucose was too high to be analysed by Alpha Track, it was recorded as 42 mM. Slope ±SE: 0.007631 ± 0.001881 P=0.0005 (G, H) Representative periodic acid stained (PAS) glomeruli for 12 week control mice (G, MME score 0) and 12-week diabetic mice (H, MME score 2). A: Arteriole, B: Bowman's space, C: Capillary Lumen, D: Distal Tubule, M: Mesangial Cells*

(Appendix 1 Figure 3B) and 20-week (Appendix 1 Figure 3D) diabetic mice. For 12-week mice, there was also a correlation between the 16-day plasma glucose and MME (Appendix 1 Figure 3F). There was no difference in MME between the 27-week non-diabetic and diabetic mice (Appendix 1 Figure 3E). This appeared to be due to an increase in MME in the non-diabetic mice rather than a decrease in the diabetic mice, which could be due to increased age-dependent non-diabetic nephropathy in these older mice. The result could also be due to the all-female cohort of mice. As is well known, diabetic phenotypes are not as strong in females[151], and there could be 'leakiness' of the tamoxifen induced mutation which would be particularly strong due to elevated levels of oestrogen.

Discussion

The increase in non-diabetic MME in the mice between 12 and 27 weeks was most likely due to tamoxifen leakage rather than age related non-diabetic nephropathy as the C57BL/6 strain is well documented as being resistant to nephropathy[146].

In a healthy kidney, mesangial cells facilitate the breakdown of the extracellular matrix and are a local controller of glomerular filtration[137]. MME is the accumulation of mesangial cells' extra-cellular matrix by glycosylation of matrix proteins. This prevents the normal degradation of these proteins leading to occlusion of glomerular capillaries causing loss of function of the glomeruli.

Periodic acid Schiff's (PAS) staining is routinely used to stain kidney slices and observe MME. PAS staining oxidises the 1-2 glycol group found in many carbohydrates, including glycolipids, glycoproteins and glycogen. While PAS staining of glomeruli is usually considered indicative of carbohydrates other than glycogen, especially the glycoproteins

associated with MME, it could also be indicating glycogen deposition. While glycogen content in healthy kidneys is minimal, glycogen deposition in the kidneys is associated with diabetes. The main location of deposition is considered to be the Henle's loop, but it has been suggested that increased glomerular PAS staining could be contributed to by glycogen deposition[152]. While it would have been interesting to use these kidney sections to stain specifically for glycogen using an antibody, and then to investigate whether the glycogen build up differs between diabetic and non-diabetic mice and may itself toxic in addition to the structural problems MME causes, the glycogen anti-body is difficult to produce and therefore a scarce resource. Furthermore, this avenue of investigation was of low priority given nephropathy was not the main focus of the study.

Long-term hyperglycaemia increases the aldose reductase enzyme and sorbitol production, which in turn increases the extracellular matrix[153]. The upregulated polyol pathway is associated with many tissues in diabetes including Diabetic Nephropathy[154]. As increased flux through this pathway increases fructose (which create more AGEs than glucose) it contributes to MME[155]. Investigations into the polyol pathway in pancreatic islets in this mouse model have generated interesting data [156] so it would have been interesting to extend this investigation to the kidneys.

Appendix 2 - References

1. Digital, P. and M. T., NHS. Prescribing for Diabetes: England 2007/08 to 2017/18. *Prescribing for Diabetes: England 2007/08 to 2017/18* https://files.digital.nhs.uk/C6/6167D2/NHS-DIGITAL-pres-diab-eng-1718.pdf (2018).

2. Hex, N., Bartlett, C., Wright, D., Taylor, M. & Varley, D. Estimating the current and future costs of Type 1 and Type 2 diabetes in the UK, including direct health costs and indirect societal and productivity costs. *Diabetic Medicine* **29**, 855–862 (2012).

3. Mahajan, A. *et al.* Fine-mapping type 2 diabetes loci to single-variant resolution using high-density imputation and islet-specific epigenome maps. *Nat Genet* **50**, 1505–1513 (2018).

4. DeFronzo, R. A. *et al.* Type 2 diabetes mellitus. *Nature Reviews Disease Primers* **1**, nrdp201519 (2015).

5. Rorsman, P. & Ashcroft, F. M. Pancreatic β-Cell Electrical Activity and Insulin Secretion: Of Mice and Men. *Physiological Reviews* **98**, 117–214 (2018).

6. Kawahito, S., Kitahata, H. & Oshita, S. Problems associated with glucose toxicity: Role of hyperglycemia-induced oxidative stress. *World J Gastroentero* **15**, 4137–4142 (2009).

7. Brereton, M. F. *et al.* Hyperglycaemia induces metabolic dysfunction and glycogen accumulation in pancreatic β-cells. *Nat Commun* **7**, 13496 (2016).

8. DeFronzo, R. A. From the triumvirate to the "ominous octet”: a new paradigm for the treatment of type 2 diabetes mellitus. *Diabetes* **58**, (2009).

9. DeFronzo, R. A., Ferrannini, E., Hendler, R. & Wahren, J. Influence of hyperinsulinemia, hyperglycemia, and the route of glucose administration on splanchnic glucose exchange. *PNAS* **75**, 5173–5177 (1978).

10. Ferrannini, E., Simonson, D. & Katz, L. The disposal of an oral glucose load in patients with non-insulin-dependent diabetes. *Metabolism* **37**, 79–85 (1988).

11. DeFronzo, R. *et al.* Characterization of renal glucose reabsorption in response to dapagliflozin in healthy subjects and subjects with type 2 diabetes. *Diabetes Care* **36**, 3169–3176 (2013).

12. Barrett, E., Wang, H. & Upchurch, C. Insulin regulates its own delivery to skeletal muscle by feed-forward actions on the vasculature. *Am J Physiol Endocrinol Metab* **301**, E252-63 (2011).

13. Baron, A. Hemodynamic actions of insulin. *Am J Physiol* **267**, (1994).

14. Khalid, M., Alkaabi, J., Khan, M. A. & Adem, A. Insulin Signal Transduction Perturbations in Insulin Resistance. *Int J Mol Sci* **22**, 8590 (2021).

15. DeFronzo. Insulin resistance, lipotoxicity, type 2 diabetes and atherosclerosis: the missing links. The Claude Bernard Lecture 2009. *Diabetologia* **53**, 1270–87 (2010).

16. Samuel, V. & Cell, S.-G. Mechanisms for insulin resistance: common threads and missing links. *Cell* **148**, 852–71 (2012).

17. Krüger, M. *et al.* Dissection of the insulin signaling pathway via quantitative phosphoproteomics. *PNAS* **105**, 2451–6 (2008).

18. Cusi, K. *et al.* Insulin resistance differentially affects the PI 3-kinase–and MAP kinase–mediated signaling in human muscle. *J Clin Invest.* **105**, 311–20 (2000).

19. Krook, A. *et al.* Characterization of signal transduction and glucose transport in skeletal muscle from type 2 diabetic patients. *Diabetes* **49**, 284–92 (2000).

20. Hiratani, K. *et al.* Roles of mTOR and JNK in serine phosphorylation, translocation, and degradation of IRS-1. *Biochem Biophys Res Commum.* **335**, 836–42 (2005).

21. Bouzakri, K. *et al.* IRS-1 serine phosphorylation and insulin resistance in skeletal muscle from pancreas transplant recipients. *Diabetes* **55**, 785–91 (2006).

22. Copps, K. & -. Regulation of insulin sensitivity by serine/threonine phosphorylation of insulin receptor substrate proteins IRS1 and IRS2. *Diabetologia* **55**, 2565–82 (2012).

23. Yu, C. *et al.* Mechanism by which fatty acids inhibit insulin activation of insulin receptor substrate-1 (IRS-1)-associated phosphatidylinositol 3-kinase activity in muscle. *J Biol Chem* **277**, 50230–6 (2002).

24. Petersen, K. *et al.* Mitochondrial dysfunction in the elderly: possible role in insulin resistance. *Science* **300**, 1140–2 (2003).

25. Petersen, K., Dufour, S. & Med, S. G. Decreased insulin-stimulated ATP synthesis and phosphate transport in muscle of insulin-resistant offspring of type 2 diabetic parents. *PLoS Med* **2**, e223 (2005).

26. Wang, C., Wang, C., Huang, H. & -. Mitochondrial dysfunction leads to impairment of insulin sensitivity and adiponectin secretion in adipocytes. *FEBS J.* **280**, 1039–50 (2013).

27. Lumeng, C. & Saltiel, S.-. Inflammatory links between obesity and metabolic disease. *J Clin Ivest.* **121**, 2111–7 (2011).

28. Weir, G. C. & Bonner-Weir, S. Five Stages of Evolving Beta-Cell Dysfunction During Progression to Diabetes. *Diabetes* **53**, S16–S21 (2004).

29. Foundation, B. H. BHF CVD Statistics UK Factsheet. https://www.bhf.org.uk/what-we-do/our-research/heart-statistics (2175).

30. Seferović, P. M. & Paulus, W. J. Clinical diabetic cardiomyopathy: a two-faced disease with restrictive and dilated phenotypes. *Eur Heart J* **36**, 1718–1727 (2015).

31. Kenny, H. C. & Abel, E. D. Heart Failure in Type 2 Diabetes Mellitus. *Circ Res* **124**, 121–141 (2019).

32. Mannucci, E., Dicembrini, I., Lauria, A. & Pozzilli, P. Is Glucose Control Important for Prevention of Cardiovascular Disease in Diabetes? *Diabetes Care* **36**, S259–S263 (2013).

33. McGurnaghan, S. *et al.* Cardiovascular disease prevalence and risk factor prevalence in Type 2 diabetes: a contemporary analysis. *Diabetic Med* **36**, 718–725 (2019).

34. NICE. Cardiovascular disease: risk assessment and reduction, including lipid modification. https://www.nice.org.uk/guidance/cg181 (2014).

35. NICE. Hypertension in adults: diagnosis and management. https://www.nice.org.uk/guidance/ng136 (2019).

36. NICE. Type 2 diabetes in adults: management. https://www.nice.org.uk/guidance/ng28 (2015).

37. Saydah, S. H., Gregg, E. W., Kahn, H. S. & Ali, M. K. Mortality associated with less intense risk-factor control among adults with diabetes in the United States. *Prim Care Diabetes* **12**, 3–12 (2018).

38. Pernicova, I. & Korbonits, M. Metformin—mode of action and clinical implications for diabetes and cancer. *Nat Rev Endocrinol* **10**, 143–156 (2014).

39. Sakamoto, J. *et al.* Activation of Human Peroxisome Proliferator-Activated Receptor (PPAR) Subtypes by Pioglitazone. *Biochem Bioph Res Co* **278**, 704–711 (2000).

40. Packer, M. *et al.* Cardiovascular and Renal Outcomes with Empagliflozin in Heart Failure. *New Engl J Med* **383**, 1413–1424 (2020).

41. McMurray, J. J. V. *et al.* Dapagliflozin in Patients with Heart Failure and Reduced Ejection Fraction. *New Engl J Med* **381**, 1995–2008 (2019).

42. Petrie, M. C. *et al.* Effect of Dapagliflozin on Worsening Heart Failure and Cardiovascular Death in Patients With Heart Failure With and Without Diabetes. *Jama* **323**, 1353 (2020).

43. Marso, S. P. *et al.* Liraglutide and Cardiovascular Outcomes in Type 2 Diabetes. *New Engl J Medicine* **375**, 311–322 (2016).

44. Marso, S. P. *et al.* Semaglutide and Cardiovascular Outcomes in Patients with Type 2 Diabetes. *New Engl J Medicine* **375**, 1834–1844 (2016).

45. Zinman, B. *et al.* Empagliflozin, Cardiovascular Outcomes, and Mortality in Type 2 Diabetes. *New Engl J Medicine* **373**, 2117–2128 (2015).

46. Neal, B. *et al.* Canagliflozin and Cardiovascular and Renal Events in Type 2 Diabetes. *New Engl J Medicine* **377**, 644–657 (2017).

47. Kerr, M., Dodd, M. S. & Heather, L. C. The 'Goldilocks zone' of fatty acid metabolism; to ensure that the relationship with cardiac function is just right. *Clin Sci* **131**, 2079–2094 (2017).

48. Ward, M.-L. & Crossman, D. J. Mechanisms underlying the impaired contractility of diabetic cardiomyopathy. *World J Cardiol* **6**, 577–584 (2014).

49. Galloway, C. A. & Yoon, Y. Mitochondrial Dynamics in Diabetic Cardiomyopathy. *Antioxid Redox Sign* **22**, 1545–1562 (2015).

50. SEARLS, Y. M., SMIRNOVA, I. V., FEGLEY, B. R. & STEHNO-BITTEL, L. Exercise Attenuates Diabetes-Induced Ultrastructural Changes in Rat Cardiac Tissue. *Medicine Sci Sports Exerc* **36**, 1863–1870 (2004).

51. Salvatore, T. *et al.* The Diabetic Cardiomyopathy: The Contributing Pathophysiological Mechanisms. *Frontiers Medicine* **8**, 695792 (2021).

52. Mohan, M. *et al.* Left Ventricular Hypertrophy in Diabetic Cardiomyopathy: A Target for Intervention. *Frontiers Cardiovasc Medicine* **8**, 746382 (2021).

53. Wilson, A. J. *et al.* Reactive oxygen species signalling in the diabetic heart: emerging prospect for therapeutic targeting. *Heart* **104**, 293–299 (2017).

54. Bugger, H. & Abel, E. D. Molecular mechanisms of diabetic cardiomyopathy. *Diabetologia* **57**, 660–671 (2014).

55. Doenst, T., Nguyen, T. & Abel, E. Cardiac metabolism in heart failure: implications beyond ATP production. *Circ. res* **113**, 709–24 (2013).

56. Vusse, G. van der, Bilsen, M. van & Glatz, J. Cardiac fatty acid uptake and transport in health and disease. *Cardiovasc. Res.* **45**, 279–93 (2000).

57. Ibrahimi, A. *et al.* Expression of the CD36 homolog (FAT) in fibroblast cells: effects on fatty acid transport. *Proc Natl Acad Sci USA.* **93**, 2646–51 (1996).

58. Hardy, C., Weiss, R., Bottomley - & Gerstenblith, G. Altered myocardial high-energy phosphate metabolites in patients with dilated cardiomyopathy. *Am Heart J.* **122**, 795–801 (1991).

59. Conway, M. *et al.* Detection of low phosphocreatine to ATP ratio in failing hypertrophied human myocardium by 31P magnetic resonance spectroscopy. *Lancet* **338**, 973–6 (1991).

60. Heather, L. *et al.* Changes in cardiac substrate transporters and metabolic proteins mirror the metabolic shift in patients with aortic stenosis. *PloS One* **6**, e26326 (2011).

61. Sack, M. *et al.* Fatty acid oxidation enzyme gene expression is downregulated in the failing heart. *Circulation* **94**, 2837–2842 (1996).

62. Heather, L. *et al.* Fatty acid transporter levels and palmitate oxidation rate correlate with ejection fraction in the infarcted rat heart. *Cardiovas Res* **72**, 430–437 (2006).

63. Razeghi, P. *et al.* Metabolic gene expression in fetal and failing human heart. *Circulation* **104**, 2923–31 (2001).

64. Aasum, E., Hafstad, A., Severson, D. & Diabetes, -. Age-dependent changes in metabolism, contractile function, and ischemic sensitivity in hearts from db/db mice. *Diabetes* **52**, 434–41 (2003).

65. Rijzewijk, L. *et al.* Myocardial steatosis is an independent predictor of diastolic dysfunction in type 2 diabetes mellitus. *J Am Coll Cardiol* **52**, 1793–99 (2008).

66. Zlobine, I. & Gopal, K. Lipotoxicity in obesity and diabetes-related cardiac dysfunction. *Biochim Biophys Acta.* **1861**, 1555–68 (2016).

67. Drosatos, K. & Schulze. Cardiac lipotoxicity: molecular pathways and therapeutic implications. *Curr Heart Fail Rep* **10**, 109–21 (2013).

68. Luiken, J. *et al.* Changes in fatty acid transport and transporters are related to the severity of insulin deficiency. *Am J Physiol Endocrinol Metab.* **283**, e612-21 (2002).

69. Levelt, E. *et al.* Ectopic and visceral fat deposition in lean and obese patients with type 2 diabetes. *J Am Coll Cardiol.* **68**, 53–63 (2016).

70. Finck, B. *et al.* The cardiac phenotype induced by PPARα overexpression mimics that caused by diabetes mellitus. *J Clin Invest* **109**, 121–130 (2002).

71. Buchanan, J. *et al.* Reduced cardiac efficiency and altered substrate metabolism precedes the onset of hyperglycemia and contractile dysfunction in two mouse models of insulin. *Endocrinology* **146**, 5341–9 (2005).

72. Boardman, N., Hafstad, A. D., Larsen, T. S., Severson, D. L. & Aasum, E. Increased O2 cost of basal metabolism and excitation-contraction coupling in hearts from type 2 diabetic mice. *Am J Physiol-heart C* **296**, H1373–H1379 (2009).

73. Murray, A., Panagia, M., Hauton, D. & Clarke, K. Plasma free fatty acids and peroxisome proliferator–activated receptor α in the control of myocardial uncoupling protein levels. *Diabetes* **54**, 3496–502 (2005).

74. O'Donnell, J. *et al.* Accelerated triacylglycerol turnover kinetics in hearts of diabetic rats include evidence for compartmented lipid storage. *Am J Physiol Endocrinol Metab.* **290**, e448-55 (2006).

75. Mansor, L. S. *et al.* Increased oxidative metabolism following hypoxia in the type 2 diabetic heart, despite normal hypoxia signalling and metabolic adaptation. *J Physiology* **594**, 307–320 (2016).

76. Bugger, H. & Abel, D. E. Rodent models of diabetic cardiomyopathy. *Dis Model Mech* **2**, 454–466 (2009).

77. Boudina, S. & Abel. Diabetic cardiomyopathy revisited. *Circulation* **115**, 3213–23 (2007).

78. Mansor, L. S. *et al.* Cardiac metabolism in a new rat model of type 2 diabetes using high-fat diet with low dose streptozotocin. *Cardiovasc Diabetol* **12**, 136–136 (2013).

79. Reed, M. *et al.* A new rat model of type 2 diabetes: the fat-fed, streptozotocin-treated rat. *Metabolism* **49**, 1390–4 (2000).

80. Srinivasan, K., Viswanad, B., Asrat, L. & Ramarao, P. Combination of high-fat diet-fed and low-dose streptozotocin-treated rat: a model for type 2 diabetes and pharmacological screening. *Pharmacol Res.* **52**, 313–20 (2005).

81. Milani-Nejad, N. & Janssen, P. M. L. Small and large animal models in cardiac contraction research: Advantages and disadvantages. *Pharmacol Therapeut* **141**, 235–249 (2014).

82. Lemieux, H. & Hoppel, C. L. Mitochondria in the human heart. *J Bioenerg Biomembr* **41**, 99–106 (2009).

83. Burridge, P. W., Keller, G., Gold, J. D. & Wu, J. C. Production of De Novo Cardiomyocytes: Human Pluripotent Stem Cell Differentiation and Direct Reprogramming. *Cell Stem Cell* **10**, 16–28 (2012).

84. Lian, X. *et al.* Robust cardiomyocyte differentiation from human pluripotent stem cells via temporal modulation of canonical Wnt signaling. *PNAS* **109**, e1848-57 (2012).

85. Robertson, C., Tran, D. D. & George, S. C. Concise Review: Maturation Phases of Human Pluripotent Stem Cell-Derived Cardiomyocytes. *Stem Cells* **31**, 829–837 (2013).

86. Lopez, C. A. *et al.* Physiological and pharmacological stimulation for in vitro maturation of substrate metabolism in human induced pluripotent stem cell-derived cardiomyocytes. *Sci Rep-uk* **11**, 7802 (2021).

87. Guo, Y. & Pu, W. T. Cardiomyocyte Maturation: New Phase in Development. *Circ Res* **126**, 1086–1106 (2020).

88. Lieu, D. *et al.* Absence of Transverse Tubules Contributes to Non-Uniform Ca2+ Wavefronts in Mouse and Human Embryonic Stem Cell–Derived Cardiomyocytes. *Stem Cells Dev.* **18**, 1493–500 (2009).

89. Snir, M. *et al.* Assessment of the ultrastructural and proliferative properties of human embryonic stem cell-derived cardiomyocytes. *Am J Physiol Heart Circ Physiol* **285**, H2355-63 (2003).

90. Smolich, J. Ultrastructural and functional features of the developing mammalian heart: a brief overview. *Reprod. Fertil Dev* **7**, 451–61 (1995).

91. Zhu, R. *et al.* Physical developmental cues for the maturation of human pluripotent stem cell-derived cardiomyocytes. *Stem Cell Res Ther* **5**, 117 (2014).

92. Lieu, D. *et al.* Mechanism-based facilitated maturation of human pluripotent stem cell–derived cardiomyocytes. *Circ Arrhythm Electrophysiol* **6**, 191–201 (2013).

93. Yang, X., Pabon, L. & Murry, C. Engineering adolescence: maturation of human pluripotent stem cell–derived cardiomyocytes. *Circ Res.* **114**, 511–23 (2014).

94. Kalkhoran, S. *et al.* Unique morphological characteristics of mitochondrial subtypes in the heart: the effect of ischemia and ischemic preconditioning. *Discov* **5**, e71 (2017).

95. Kuznetsov, A. & Margreiter, R. Heterogeneity of Mitochondria and Mitochondrial Function within Cells as Another Level of Mitochondrial Complexity. *Int J Mol Sci* **10**, 1911–1929 (2009).

96. Tashiro, A., Masuda, T. & Segawa, I. Morphometric comparison of mitochondria and myofibrils of cardiomyocytes between hypertrophic and dilated cardiomyopathies. *Virchows Archiv* **416**, 473–478 (1990).

97. Barth, E., Stämmler, G., Speiser, B. & and, - of molecular. Ultrastructural quantitation of mitochondria and myofilaments in cardiac muscle from 10 different animal species including man. **24**, 669–81 (1992).

98. Hattori, F. *et al.* Nongenetic method for purifying stem cell–derived cardiomyocytes. *Nat. Methods* **7**, 61–6 (2010).

99. Habib, M., Caspi, O. & Gepstein, L. Human embryonic stem cells for cardiomyogenesis. *J Mol Cell Cardiol* **45**, 462–74 (2008).

100. Eschenhagen, T., Eder, A., Vollert, I. & Hansen, A. Physiological aspects of cardiac tissue engineering. *Am J Physiol-heart C* **303**, H133–H143 (2012).

101. Leor, J. *et al.* Bioengineered cardiac grafts: a new approach to repair the infarcted myocardium? *Circulation* **102**, 11156–61 (2000).

102. Ott, H. *et al.* Perfusion-decellularized matrix: using nature's platform to engineer a bioartificial heart. *Nature Medicine* **14**, 213–221 (2008).

103. Papadaki, M. *et al.* Tissue engineering of functional cardiac muscle: molecular, structural, and electrophysiological studies. *Am J Physiol Heart Circ Physiol* **280**, h168-78 (2001).

104. Freed, L. *et al.* Functional assembly of engineered myocardium by electrical stimulation of cardiac myocytes cultured on scaffolds. *PNAS* **101**, 18129–34 (2004).

105. Karoubi, G., Ormiston, M., Stewart, D. & Courtman. Single-cell hydrogel encapsulation for enhanced survival of human marrow stromal cells. *Biomaterials* **30**, 5445–55 (2009).

106. Munoz, J., Zhou, Y. & Jarrett, H. LG4–5 domains of laminin-211 binds α-Dystroglycan to allow myotube attachment and prevent anoikis. *J Cell Physiol* **222**, 111–9 (2010).

107. Bian, W., Liau, B. & Badie, N. Mesoscopic hydrogel molding to control the 3D geometry of bioartificial muscle tissues. *Nature Protocols* **4**, 1522–34 (2009).

108. Fink, C. *et al.* Three-dimensional reconstitution of embryonic cardiomyocytes in a collagen matrix: a new heart muscle model system. *FASEB J* **11**, 683–694 (1997).

109. Morritt, A. *et al.* Cardiac tissue engineering in an in vivo vascularized chamber. *Circulation* **115**, 353–60 (2007).

110. Hansen, A. *et al.* Development of a drug screening platform based on engineered heart tissue. *Circ Res* **107**, 35–44 (2010).

111. Breckwoldt, K. *et al.* Differentiation of cardiomyocytes and generation of human engineered heart tissue. *Nat Protoc* **12**, 1177–1197 (2017).

112. Chung, S. *et al.* Mitochondrial oxidative metabolism is required for the cardiac differentiation of stem cells. *Nat Clin Pract Card* **4**, S60–S67 (2007).

113. Glancy, B., Kim, Y., Katti, P. & Willingham, T. B. The Functional Impact of Mitochondrial Structure Across Subcellular Scales. *Front Physiol* **11**, 541040 (2020).

114. Kanamori, H. *et al.* Autophagic adaptations in diabetic cardiomyopathy differ between type 1 and type 2 diabetes. *Autophagy* **11**, 1146–1160 (2015).

115. Graham, L. & Orenstein, -. Processing tissue and cells for transmission electron microscopy in diagnostic pathology and research. *Nature protocols* **2**, 2439–50 (2007).

116. Yu, J. *et al.* Induced Pluripotent Stem Cell Lines Derived from Human Somatic Cells. *Science* **318**, 1917–1920 (2007).

117. Nichols, W. *et al.* Characterization of a New Human Diploid Cell Strain, IMR-90. *Science* **196**, 60–63 (1977).

118. Thornell, L. E. Distinction of glycogen and ribosome particles in cow purkinje fibers by enzymatic digestion En bloc and in sections. *J Ultra Mol Struct R* **47**, 153–168 (1974).

119. Mansouri, H., Paige, R. L. & Surles, J. G. Aligned Rank Transform Techniques for Analysis of Variance and Multiple Comparisons. *Commun Statistics - Theory Methods* **33**, 2217–2232 (2004).

120. Soper, D. S. Significance of the Difference between Two Correlations Calculator [Software]. https://www.danielsoper.com/statcalc (2022).

121. Fisher, R. A. On the Probable Error of a Coefficient of Correlation Deduced from a Small Sample. *Metron* **1**, 3–32 (1921).

122. Mannhardt, I. *et al.* Human Engineered Heart Tissue: Analysis of Contractile Force. *Stem Cell Rep* **7**, 29–42 (2016).

123. Katare, R. G., Ando, M., Kakinuma, Y. & Sato, T. Engineered Heart Tissue: A Novel Tool to Study the Ischemic Changes of the Heart In Vitro. *Plos One* **5**, e9275 (2010).

124. Ulmer, B. M. *et al.* Contractile Work Contributes to Maturation of Energy Metabolism in hiPSC-Derived Cardiomyocytes. *Stem Cell Rep* **10**, 834–847 (2018).

125. Piquereau, J. *et al.* Mitochondrial dynamics in the adult cardiomyocytes: which roles for a highly specialized cell? *Front Physiol* **4**, 102 (2013).

126. Pohjoismäki, J. L. & Goffart, S. The role of mitochondria in cardiac development and protection. *Free Radic Biology Medicine* **106**, 345–354 (2017).

127. Riva, A., Tandler, B., Loffredo, F., Vazquez, E. & Hoppel, C. Structural differences in two biochemically defined populations of cardiac mitochondria. *Am J Physiol-heart C* **289**, H868–H872 (2005).

128. Gerdes, A. M., Morales, M. C., Handa, V., Moore, J. A. & Alvarez, M. R. Nuclear size and DNA content in rat cardiac myocytes during growth, maturation and aging. *J Mol Cell Cardiol* **23**, 833–839 (1991).

129. Duncan, J. G., Fong, J. L., Medeiros, D. M., Finck, B. N. & Kelly, D. P. Insulin-Resistant Heart Exhibits a Mitochondrial Biogenic Response Driven by the Peroxisome Proliferator-Activated Receptor-α/PGC-1α Gene Regulatory Pathway. *Circulation* **115**, 909–917 (2007).

130. Dominguez, R. & Holmes, K. C. Actin Structure and Function. *Annu Rev Biophys* **40**, 169–186 (2011).

131. DePina, A. S. & Langford, G. M. Vesicle transport: The role of actin filaments and myosin motors. *Microsc Res Techniq* **47**, 93–106 (1999).

132. Castro-Sepulveda, M. *et al.* Relative lipid oxidation associates directly with mitochondrial fusion phenotype and mitochondria-sarcoplasmic reticulum interactions in human skeletal muscle. *Am J Physiol-endoc M* **318**, E848–E855 (2020).

133. Mereweather, L. J., Aparicio, C. N. M. & Heather, L. C. Positioning Metabolism as a Central Player in the Diabetic Heart. *J Lipid Atheroscler* **9**, 92 (2020).

134. Fialho, M. da L. S. *et al.* Activation of HIF1α Rescues the Hypoxic Response and Reverses Metabolic Dysfunction in the Diabetic Heart. *Diabetes* **70**, 2518–2531 (2021).

135. Leonard, A. *et al.* Afterload promotes maturation of human induced pluripotent stem cell derived cardiomyocytes in engineered heart tissues. *J Mol Cell Cardiol* **118**, 147–158 (2018).

136. Lu, K. *et al.* Progressive stretch enhances growth and maturation of 3D stem-cell-derived myocardium. *Theranostics* **11**, 6138–6153 (2021).

137. Gross, J. L. *et al.* Diabetic Nephropathy: Diagnosis, Prevention, and Treatment. *Diabetes Care* **28**, 164–176 (2005).

138. Shahbazian, H. & Rezaii, I. Diabetic kidney disease; review of the current knowledge. *Journal of Renal Injury Prevention* **2**, 73–80 (2013).

139. UK, D. Diabetic Nephropathy (Kidney Disease). https://www.diabetes.org.uk/guide-to-diabetes/complications/kidneys_nephropathy.

140. Lin, J. S. & Susztak, K. Podocytes: the Weakest Link in Diabetic Kidney Disease? *Curr Diabetes Rep* **16**, 45 (2016).

141. McLennan, S. V. *et al.* Advanced glycation end products decrease mesangial cell MMP-7: A role in matrix accumulation in diabetic nephropathy? *Kidney Int* **72**, 481–488 (2007).

142. Noh, H. & King, G. L. The role of protein kinase C activation in diabetic nephropathy. *Kidney Int* **72**, S49–S53 (2007).

143. Group, W. T. for the D. C. and C. T. of D. I. and C. R. Sustained effect of intensive treatment of type 1 diabetes mellitus on development and progression of diabetic nephropathy: the Epidemiology of Diabetes. *JAMA* **290**, 2159–67 (2003).

144. Giunti, S., Barit, D. & Cooper, M. E. Mechanisms of Diabetic Nephropathy. *Hypertension* **48**, 519–526 (2006).

145. Association, A. D. Dyslipidemia management in adults with diabetes. *Diabetes Care* **27**, s68-71 (2004).

146. Alpers, C. E. & Hudkins, K. L. Mouse models of diabetic nephropathy. *Curr Opin Nephrol Hy* **20**, 278–284 (2011).

147. Bai, X. *et al.* A new model of diabetic nephropathy in C57BL/6 mice challenged with advanced oxidation protein products. *Free Radical Bio Med* **118**, 71–84 (2018).

148. Breyer, M. D. *et al.* Mouse models of diabetic nephropathy. *Journal of the American Society of Nephrology* **16**, 27–45 (2005).

149. Brereton, M. F. *et al.* Reversible changes in pancreatic islet structure and function produced by elevated blood glucose. *Nature communications* **5**, 4639 (2014).

150. Rohm, M. *et al.* Cardiac Dysfunction and Metabolic Inflexibility in a Mouse Model of Diabetes Without Dyslipidaemia. *Diabetes* **67**, db171195 (2018).

151. Dubuc, P. U., Scott, K. B. & Peterson, C. M. Sex differences in glycated hemoglobin in diabetic and non-diabetic C57BL/6 mice. *Diabetes Res Clin Pr* **21**, 95–101 (1993).

152. Sullivan, M. A. & Forbes, J. M. Glucose and glycogen in the diabetic kidney: Heroes or villains? *Ebiomedicine* **47**, 590–597 (2019).

153. Bader, E. *et al.* Identification of proliferative and mature β-cells in the islets of Langerhans. *Nature* **535**, 430 (2016).

154. Yan, L. Redox imbalance stress in diabetes mellitus: Role of the polyol pathway. *Animal Model Exp Medicine* **1**, 7–13 (2018).

155. Sharma, V. Role of Different Molecular Pathways in the Development of Diabetes-Induced Nephropathy. *J Diabetes Metabolism* **01**, (2013).

156. Haythorne, E. *et al.* Diabetes causes marked inhibition of mitochondrial metabolism in pancreatic β-cells. *Nat Commun* **10**, 2474 (2019).

Appendix 3 – Data Processing



Appendix 3 – Figure 1: *Regions Of Interest (mitochondria) selected in FIJI (ImageJ)*

Results

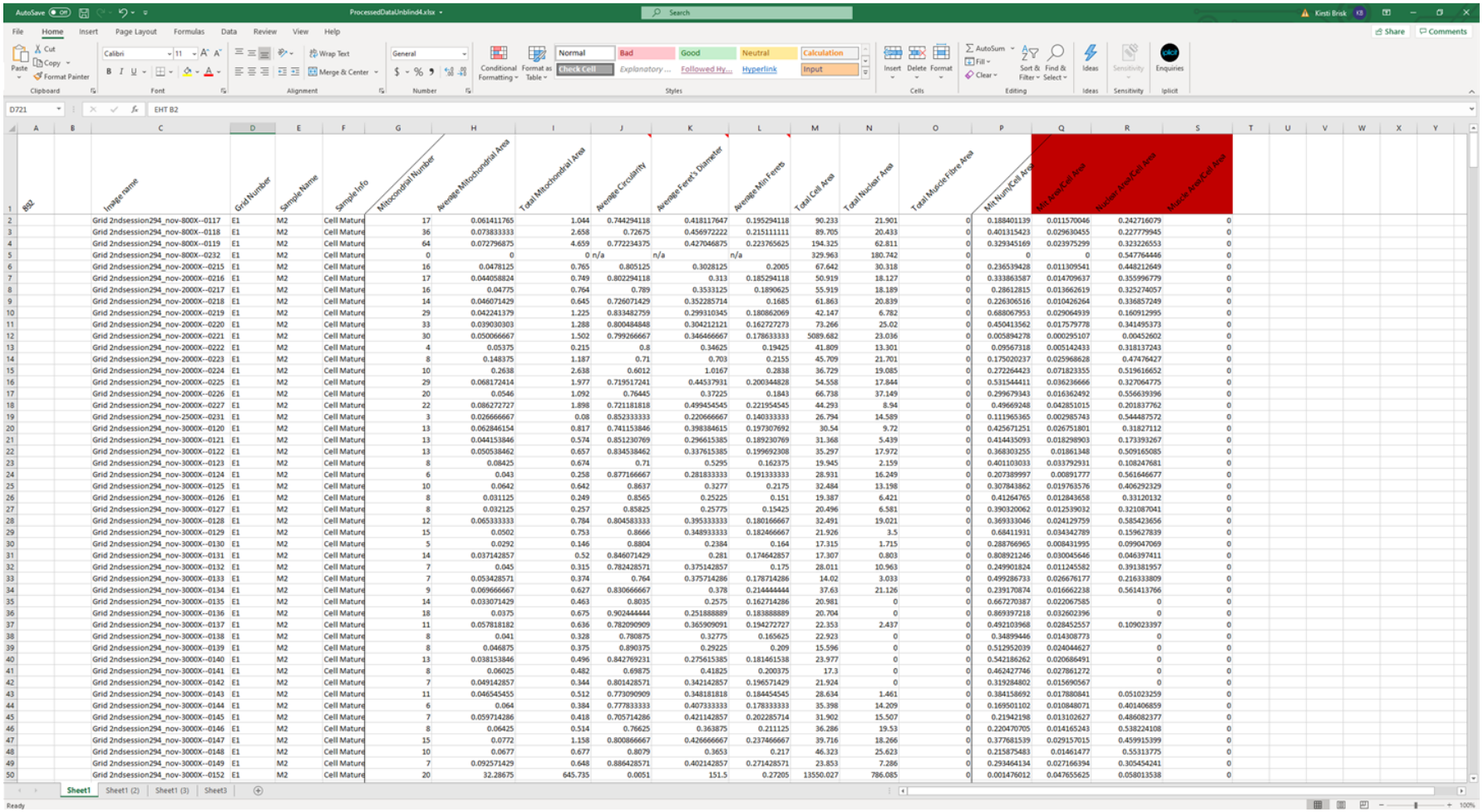
File Edit Font Results

	Area	Perim.	Circ.	Feret	%Area
1	0.309	2.774	0.505	1.265	99.974
2	0.056	0.958	0.761	0.389	99.966
3	0.057	0.879	0.921	0.316	99.992
4	0.027	0.612	0.922	0.223	99.939
5	0.067	1.021	0.810	0.378	99.430
6	0.019	0.492	0.961	0.173	99.838

Appendix 3 – Figure 2: *Parameters measured by FIJI (ImageJ)*

Appendix 3- Figure 3: *Parameters compiled in Microsoft Excel (example snapshot)*

Appendix 3 – Figure 4: *Further calculation and compilation*



	B02	Image name	Grid Number	Sample Name	Sample Info	Mitochondrial Number	Average Mitochondrial Area	Total Mitochondrial Area	Average Circularity	Average Feret's Diameter	Average Min Ferets	Total Cell Area	Total Nuclear Area	Total Muscle Fibre Area	Mit Num/Cell Area	Mit Area/Cell Area	Nuclear Area/Cell Area	Muscle Area/Cell Area
2		Grid 2ndsession294_nov-800X--0117	E1	M2	Cell Mature	17	0.061411765	1.044	0.744294118	0.418117647	0.195294118	90.233	21.901	0	0.188401139	0.011570046	0.242716079	0
3		Grid 2ndsession294_nov-800X--0118	E1	M2	Cell Mature	36	0.073833333	2.658	0.72675	0.456972222	0.215111111	89.705	20.433	0	0.401315423	0.029630455	0.227779945	0
4		Grid 2ndsession294_nov-800X--0119	E1	M2	Cell Mature	64	0.072796875	4.659	0.772234375	0.427046875	0.223765625	194.325	62.811	0	0.329345169	0.023975299	0.323226553	0
5		Grid 2ndsession294_nov-800X--0232	E1	M2	Cell Mature	0	0	0	n/a	n/a	n/a	329.963	180.742	0	0	0	0.547764446	0
6		Grid 2ndsession294_nov-2000X--0215	E1	M2	Cell Mature	16	0.0478125	0.765	0.805125	0.3028125	0.2005	67.642	30.318	0	0.236539428	0.011309541	0.448212649	0
7		Grid 2ndsession294_nov-2000X--0216	E1	M2	Cell Mature	17	0.044058824	0.749	0.802294118	0.313	0.185294118	50.919	18.127	0	0.333863587	0.014709637	0.355996779	0
8		Grid 2ndsession294_nov-2000X--0217	E1	M2	Cell Mature	16	0.04775	0.764	0.789	0.3533125	0.1890625	55.919	18.189	0	0.28612815	0.013662619	0.325274057	0
9		Grid 2ndsession294_nov-2000X--0218	E1	M2	Cell Mature	14	0.046071429	0.645	0.726071429	0.352285714	0.1685	61.863	20.839	0	0.226306516	0.010426264	0.336857249	0
10		Grid 2ndsession294_nov-2000X--0219	E1	M2	Cell Mature	29	0.042241379	1.225	0.833482759	0.299310345	0.180862069	42.147	6.782	0	0.688067953	0.029064939	0.160912995	0
11		Grid 2ndsession294_nov-2000X--0220	E1	M2	Cell Mature	33	0.039030303	1.288	0.800484848	0.304212121	0.162727273	73.266	25.02	0	0.450413562	0.017579778	0.341495373	0
12		Grid 2ndsession294_nov-2000X--0221	E1	M2	Cell Mature	30	0.050066667	1.502	0.799266667	0.346466667	0.178633333	5089.682	23.036	0	0.005894278	0.000295107	0.00452602	0
13		Grid 2ndsession294_nov-2000X--0222	E1	M2	Cell Mature	4	0.05375	0.215	0.8	0.34625	0.19425	41.809	13.301	0	0.09567318	0.005142433	0.318137243	0
14		Grid 2ndsession294_nov-2000X--0223	E1	M2	Cell Mature	8	0.148375	1.187	0.71	0.703	0.2155	45.709	21.701	0	0.175020237	0.025968628	0.47476427	0
15		Grid 2ndsession294_nov-2000X--0224	E1	M2	Cell Mature	10	0.2638	2.638	0.6012	1.0167	0.2838	36.729	19.085	0	0.272264423	0.071823355	0.519616652	0
16		Grid 2ndsession294_nov-2000X--0225	E1	M2	Cell Mature	29	0.068172414	1.977	0.719517241	0.44537931	0.200344828	54.558	17.844	0	0.531544411	0.036236666	0.327064775	0
17		Grid 2ndsession294_nov-2000X--0226	E1	M2	Cell Mature	20	0.0546	1.092	0.76445	0.37225	0.1843	66.738	37.149	0	0.299679343	0.016362492	0.556639396	0
18		Grid 2ndsession294_nov-2000X--0227	E1	M2	Cell Mature	22	0.086272727	1.898	0.721181818	0.499454545	0.221954545	44.293	8.94	0	0.49669248	0.042851015	0.201837762	0
19		Grid 2ndsession294_nov-2500X--0231	E1	M2	Cell Mature	3	0.026666667	0.08	0.852333333	0.220666667	0.140333333	26.794	14.589	0	0.111965365	0.002985743	0.544487572	0
20		Grid 2ndsession294_nov-3000X--0120	E1	M2	Cell Mature	13	0.062846154	0.817	0.741153846	0.398384615	0.197307692	30.54	9.72	0	0.425671251	0.026751801	0.31827112	0
21		Grid 2ndsession294_nov-3000X--0121	E1	M2	Cell Mature	13	0.044153846	0.574	0.851230769	0.296615385	0.189230769	31.368	5.439	0	0.414435093	0.018298903	0.173393267	0
22		Grid 2ndsession294_nov-3000X--0122	E1	M2	Cell Mature	13	0.050538462	0.657	0.834538462	0.337615385	0.199692308	35.297	17.972	0	0.368303255	0.01861348	0.509165085	0
23		Grid 2ndsession294_nov-3000X--0123	E1	M2	Cell Mature	8	0.08425	0.674	0.71	0.5295	0.162375	19.945	2.159	0	0.401103033	0.033792931	0.108247681	0
24		Grid 2ndsession294_nov-3000X--0124	E1	M2	Cell Mature	6	0.043	0.258	0.877166667	0.281833333	0.191333333	28.931	16.249	0	0.207389997	0.00891777	0.561646677	0
25		Grid 2ndsession294_nov-3000X--0125	E1	M2	Cell Mature	10	0.0642	0.642	0.8637	0.3277	0.2175	32.484	13.198	0	0.307843862	0.019763576	0.406292329	0
26		Grid 2ndsession294_nov-3000X--0126	E1	M2	Cell Mature	8	0.031125	0.249	0.8565	0.25225	0.151	19.387	6.421	0	0.41264765	0.012843658	0.33120132	0
27		Grid 2ndsession294_nov-3000X--0127	E1	M2	Cell Mature	8	0.032125	0.257	0.85825	0.25775	0.15425	20.496	6.581	0	0.390320062	0.012539032	0.321087041	0
28		Grid 2ndsession294_nov-3000X--0128	E1	M2	Cell Mature	12	0.065333333	0.784	0.804583333	0.395333333	0.180166667	32.491	19.021	0	0.369333046	0.024129759	0.585423656	0
29		Grid 2ndsession294_nov-3000X--0129	E1	M2	Cell Mature	15	0.0502	0.753	0.8666	0.348933333	0.182466667	21.926	3.5	0	0.68411931	0.034342789	0.159627839	0
30		Grid 2ndsession294_nov-3000X--0130	E1	M2	Cell Mature	5	0.0292	0.146	0.8804	0.2384	0.164	17.315	1.715	0	0.288766965	0.008431995	0.099047069	0
31		Grid 2ndsession294_nov-3000X--0131	E1	M2	Cell Mature	14	0.037142857	0.52	0.846071429	0.281	0.174642857	17.307	0.803	0	0.808921246	0.030045646	0.046397411	0
32		Grid 2ndsession294_nov-3000X--0132	E1	M2	Cell Mature	7	0.045	0.315	0.782428571	0.375142857	0.175	28.011	10.963	0	0.249901824	0.011245582	0.391381957	0
33		Grid 2ndsession294_nov-3000X--0133	E1	M2	Cell Mature	7	0.053428571	0.374	0.764	0.375714286	0.178714286	14.02	3.033	0	0.499286733	0.026676177	0.216333809	0
34		Grid 2ndsession294_nov-3000X--0134	E1	M2	Cell Mature	9	0.069666667	0.627	0.830666667	0.378	0.214444444	37.63	21.126	0	0.239170874	0.016662238	0.561413766	0
35		Grid 2ndsession294_nov-3000X--0135	E1	M2	Cell Mature	14	0.033071429	0.463	0.8035	0.2575	0.162714286	20.981	0	0	0.667270387	0.022067585	0	0
36		Grid 2ndsession294_nov-3000X--0136	E1	M2	Cell Mature	18	0.0375	0.675	0.902444444	0.251888889	0.183888889	20.704	0	0	0.869397218	0.032602396	0	0
37		Grid 2ndsession294_nov-3000X--0137	E1	M2	Cell Mature	11	0.057818182	0.636	0.782090909	0.365909091	0.194272727	22.353	2.437	0	0.492103968	0.028452557	0.109023397	0
38		Grid 2ndsession294_nov-3000X--0138	E1	M2	Cell Mature	8	0.041	0.328	0.780875	0.32775	0.165625	22.923	0	0	0.34899446	0.014308773	0	0
39		Grid 2ndsession294_nov-3000X--0139	E1	M2	Cell Mature	8	0.046875	0.375	0.890375	0.29225	0.209	15.596	0	0	0.512952039	0.024044627	0	0
40		Grid 2ndsession294_nov-3000X--0140	E1	M2	Cell Mature	13	0.038153846	0.496	0.842769231	0.275615385	0.181461538	23.977	0	0	0.542186262	0.020686491	0	0
41		Grid 2ndsession294_nov-3000X--0141	E1	M2	Cell Mature	8	0.06025	0.482	0.69875	0.41825	0.200375	17.3	0	0	0.462427746	0.027861272	0	0
42		Grid 2ndsession294_nov-3000X--0142	E1	M2	Cell Mature	7	0.049142857	0.344	0.801428571	0.342142857	0.196571429	21.924	0	0	0.319284802	0.015690567	0	0
43		Grid 2ndsession294_nov-3000X--0143	E1	M2	Cell Mature	11	0.046545455	0.512	0.773090909	0.348181818	0.184454545	28.634	1.461	0	0.384158692	0.017880841	0.051023259	0
44		Grid 2ndsession294_nov-3000X--0144	E1	M2	Cell Mature	6	0.064	0.384	0.777833333	0.407333333	0.178333333	35.398	14.209	0	0.169501102	0.010848071	0.401406859	0
45		Grid 2ndsession294_nov-3000X--0145	E1	M2	Cell Mature	7	0.059714286	0.418	0.705714286	0.421142857	0.202285714	31.902	15.507	0	0.21942198	0.013102627	0.486082377	0
46		Grid 2ndsession294_nov-3000X--0146	E1	M2	Cell Mature	8	0.06425	0.514	0.76625	0.363875	0.211125	36.286	19.53	0	0.220470705	0.014165243	0.538224108	0
47		Grid 2ndsession294_nov-3000X--0147	E1	M2	Cell Mature	15	0.0772	1.158	0.800866667	0.426666667	0.237466667	39.716	18.266	0	0.377681539	0.029157015	0.459915399	0
48		Grid 2ndsession294_nov-3000X--0148	E1	M2	Cell Mature	10	0.0677	0.677	0.8079	0.3653	0.217	46.323	25.623	0	0.215875483	0.01461477	0.55313775	0
49		Grid 2ndsession294_nov-3000X--0149	E1	M2	Cell Mature	7	0.092571429	0.648	0.886428571	0.402142857	0.271428571	23.853	7.286	0	0.293464134	0.027166394	0.305454241	0
50		Grid 2ndsession294_nov-3000X--0152	E1	M2	Cell Mature	20	32.28675	645.735	0.0051	151.5	0.27205	13550.027	786.085	0	0.001476012	0.047655625	0.058013538	0

Appendix 4 – R code and References

R version 4.1.1: R Core Team (2021). R: A language and environment for statistical computing. R Foundation for Statistical Computing, Vienna, Austria. URL https://www.R-project.org/.

List of R packages used and their references:

"ARTool"- 0.11.1-Kay M, Elkin L, Higgins J, Wobbrock J (2021). _ARTool: Aligned Rank Transform for Nonparametric Factorial ANOVAs_. doi: 10.5281/zenodo.594511 (URL: https://doi.org/10.5281/zenodo.594511), R package version 0.11.1, <URL: https://github.com/mjskay/ARTool>.

Wobbrock J, Findlater L, Gergle D, Higgins J (2011). "The Aligned Rank Transform for Nonparametric Factorial Analyses Using Only ANOVA Procedures." In _Proceedings of the ACM Conference on Human Factors in Computing Systems (CHI '11)_, 143-146. doi: 10.1145/1978942.1978963 (URL:https://doi.org/10.1145/1978942.1978963), <URL:https://depts.washington.edu/acelab/proj/art/>.

"car"- 3.0-11-John Fox and Sanford Weisberg (2019). An {R} Companion to Applied Regression, Third Edition. Thousand Oaks CA: Sage. URL:https://socialsciences.mcmaster.ca/jfox/Books/Companion/

"carData"- 3.0-4- John Fox, Sanford Weisberg and Brad Price (2020). carData: Companion to Applied Regression Data Sets. R package version 3.0-4.

https://CRAN.R-project.org/package=carData

“dplyr”- 1.0.7-Hadley Wickham, Romain François, Lionel Henry and Kirill Müller (2021). dplyr: A Grammar of Data Manipulation. R package version 1.0.7.

https://CRAN.R-project.org/package=dplyr

“dunn.test”- 1.3.5-Alexis Dinno (2017). dunn.test: Dunn's Test of Multiple Comparisons Using Rank Sums. R package version 1.3.5.

https://CRAN.R-project.org/package=dunn.test

“emmeans”- 1.7.0-Russell V. Lenth (2021). emmeans: Estimated Marginal Means, aka Least-Squares Means. R package version 1.7.0.

https://CRAN.R-project.org/package=emmeans

“forcats”- 0.5.1-Hadley Wickham (2021). forcats: Tools for Working with Categorical Variables (Factors). R package version 0.5.1.

https://CRAN.R-project.org/package=forcats

“forecast”- 8.15-Hyndman R, Athanasopoulos G, Bergmeir C, Caceres G, Chhay L, O'Hara-Wild M, Petropoulos F, Razbash S, Wang E, Yasmeen F (2021). _forecast:

Forecasting functions for time series and linear models_. R package version 8.15, <URL: https://pkg.robjhyndman.com/forecast/>.

Hyndman RJ, Khandakar Y (2008). “Automatic time series forecasting: the forecast package for R.” _Journal of Statistical Software_, *26*(3),

1-22. <URL: https://www.jstatsoft.org/article/view/v027i03>

“ggplot2”- 3.3.5- H. Wickham. ggplot2: Elegant Graphics for Data Analysis. Springer-Verlag New York, 2016.

“ggpubr”- 0.4.0-Alboukadel Kassambara (2020). ggpubr: 'ggplot2' Based Publication Ready Plots. R package version 0.4.0.

https://CRAN.R-project.org/package=ggpubr

“lme4”- 1.1-27.1- Douglas Bates, Martin Maechler, Ben Bolker, Steve Walker (2015). Fitting Linear Mixed-Effects Models Using lme4. Journal of Statistical

Software, 67(1), 1-48. doi:10.18637/jss.v067.i01.

“MASS”- 7.3-54-Venables, W. N. & Ripley, B. D. (2002) Modern Applied Statistics with S. Fourth Edition. Springer, New York. ISBN 0-387-95457-0

“Matrix”- 1.3-4-Douglas Bates and Martin Maechler (2021). Matrix: Sparse and Dense Matrix Classes and Methods. R package version 1.3-4.

https://CRAN.R-project.org/package=Matrix

“moments” – 0.14 - Lukasz Komsta and Frederick Novomestky (2015). moments: Moments, cumulants, skewness, kurtosis and related tests. R package version 0.14.

https://CRAN.R-project.org/package=moments

“purrr”- 0.3.4- Lionel Henry and Hadley Wickham (2020). purrr: Functional Programming Tools. R package version 0.3.4. https://CRAN.R-project.org/package=purrr

“stringr”- 1.4.0-Hadley Wickham (2019). stringr: Simple, Consistent Wrappers for Common String Operations. R package version 1.4.0.

https://CRAN.R-project.org/package=stringr

“tibble”- 3.1.5- Kirill Müller and Hadley Wickham (2021). tibble: Simple Data Frames. R package version 3.1.5. https://CRAN.R-project.org/package=tibble

“tidyr”- 1.1.4- Hadley Wickham (2021). tidyr: Tidy Messy Data. R package version 1.1.4. https://CRAN.R-project.org/package=tidyr

“tidyverse”- 1.3.1 -Wickham et al., (2019). Welcome to the tidyverse. Journal of Open Source Software, 4(43), 1686, https://doi.org/10.21105/joss.01686

“xlsx” – 0.6.5- Adrian Dragulescu and Cole Arendt (2020). xlsx: Read, Write, Format Excel 2007 and Excel 97/2000/XP/2003 Files. R package version 0.6.5. https://CRAN.R-project.org/package=xlsx

R code

R code for transferring data to R a tibble data frame

```
kirstiData <- read.xlsx("D:/Carr files/Results/Processed Data5.xlsx",1);

kirstiData<-as_tibble(kirstiData);

kirstiData<- kirstiData %>% mutate(
    Image.name = as.factor(Image.name),
    Grid.Number= as.factor(Grid.Number),
    Sample.Name= as.factor(Sample.Name),
    Sample.Info= as.factor(Sample.Info),
    Average.Mitochondrial.Area=as.double(Average.Mitochondrial.Area),
    Average.Circularity=as.double(Average.Circularity),
    Average.Ferets.Diameter=as.double(Average.Ferets.Diameter),
    )

kirstiData$Average.Mitochondrial.Area[kirstiData$Average.Mitochondrial.Area == 0] <- NA
kirstiData$Average.Circularity[kirstiData$Average.Circularity == 0] <- NA
kirstiData$Average.Ferets.Diameter[kirstiData$Average.Ferets.Diameter == 0] <- NA
kirstiData$Nuclear.AreaOCell.Area[kirstiData$Nuclear.AreaOCell.Area == 0] <- NA

kirstiData <- kirstiData %>% mutate(cellType = case_when (
                                        Sample.Info == "Cell Control" ~ 'Cell',
                                        Sample.Info == "Cell Insulin Resistant" ~ 'Cell',
                                        Sample.Info == "Cell Mature" ~ 'Cell',
                                        Sample.Info == "EHT Control" ~ 'EHT',
                                        Sample.Info == "EHT Insulin Resistant" ~ 'EHT',
                                        Sample.Info == "EHT Mature" ~ 'EHT',
            )) %>% mutate(cellType = as.factor(cellType),
                  Treatment = case_when ( Sample.Info == "Cell Control" ~ 'Control',
                                        Sample.Info == "Cell Insulin Resistant" ~ 'IR',
                                        Sample.Info == "Cell Mature" ~ 'Mature',
                                        Sample.Info == "EHT Control" ~ 'Control',
                                        Sample.Info == "EHT Insulin Resistant" ~ 'IR',
                                        Sample.Info == "EHT Mature" ~ 'Mature',
                  )
                  ) %>% mutate(Treatment = as.factor(Treatment))

kirstiData$Treatment<-factor(kirstiData$Treatment, levels = c("Control", "Mature", "IR"))
```

Example R code for violin/box plot

```
dodgev <- position_dodge(width = 0.75)
dodgeb <- position_dodge(width = 0.75)

ggplot(data=kirstiData, aes(x=Treatment,y=((Muscle.AreaOCell.Area+0.001054)^lambda-1/lambda), color=cellType)) +
  geom_violin(position = dodgev) +
  geom_boxplot(width = 0.05, position = dodgeb)+
  facet_wrap(~factor(cellType, levels = c("Control", "Mature", "IR"))) +
  ylab("Muscle Area/ Cell Area (BoxCox)") +
  labs(color="Tissue Type")
```

Example R code for faceted correlation plot with regression line equation

```
ggplot(data=kirstiData, aes(y=Mit.NumOCell.Area,x=Average.Mitochondrial.Area,color=cellType)) +
  geom_point() +
  geom_smooth(method = lm, se=FALSE) +
  stat_regline_equation() +
  ylab("Mitochondrial Number") +
  xlab("Mitochondrial Size") +
  labs(color="Tissue Type")
```

Example R code for faceted correlation plot with correlation coefficient and P-value

```
ggplot(data=kirstiData, aes(y=Mit.NumOCell.Area,x=Average.Mitochondrial.Area, color=cellType)) +
  geom_point() +
  geom_smooth(method = lm, se=FALSE) +
  stat_cor() +
  facet_wrap(vars(Treatment)) +
  ylab("Mitochondrial Number") +
  xlab("Mitochondrial Size") +
  labs(color="Tissue Type")
```

Example R code for linear model ANOVA

```
aSimpleModel <- lmer((Average.Mitochondrial.Area) ~ Treatment*cellType +  (1|Sample.Name), data=kirstiData)
Anova(aSimpleModel)
```

Example R code for emmeans

```
pairs(emmeans(aSimpleModel, ~Treatment|cellType))
pairs(emmeans(aSimpleModel, ~cellType|Treatment))
```

Example R code for determining lambda for BOXCOX

```
kirstiData<- kirstiData %>% mutate(
  Nuclear.AreaOCell.Area= as.double(Nuclear.AreaOCell.Area),
  Muscle .AreaOCell.Area=as.double(Muscle.AreaOCell.Area),
  Average.Min.Ferets=as.double(Average.Min.Ferets)
)
```

Example R code for ART ANOVA

```
model <- art(Muscle.AreaOCell.Area ~ cellType + Treatment + cellType:Treatment, data = kirstiData)
anova(model)
```

Example R code for Dunn Test

```
dunn.test("Muscle.AreaOCell.Area", "Sample.Info",  method="holm")
```

Example R code for Ansari-Bradley

```
for (jx in c("Control","IR","Mature")) {
  print(jx)
  print(ansari.test(x=(kirstiData %>% filter(cellType == "Cell")
                       %>% filter(Treatment==jx))$Muscle.AreaOCell.Area
                    ,y=(kirstiData %>% filter(cellType == "EHT")
                        %>% filter(Treatment==jx))$Muscle.AreaOCell.Area))
}

for (jx in c("Cell","EHT")) {
  print(jx)
  print(ansari.test(x=(kirstiData %>% filter(Treatment == "Control")
                       %>% filter(cellType==jx))$Muscle.AreaOCell.Area
                    ,y=(kirstiData %>% filter(Treatment == "Mature")
                        %>% filter(cellType==jx))$Muscle.AreaOCell.Area))
}


for (jx in c("Cell","EHT")) {
  print(jx)
  print(ansari.test(x=(kirstiData %>% filter(Treatment == "Mature")
                       %>% filter(cellType==jx))$Muscle.AreaOCell.Area
                    ,y=(kirstiData %>% filter(Treatment == "IR")
                        %>% filter(cellType==jx))$Muscle.AreaOCell.Area))
}
```

Appendix 5 - Experiments

Due to lockdown limitations to laboratory occupancy levels, some of the cells and EHTs were produced by Ujang Purnama. Cell culture duties were shared for the period leading up to and after lockdown in order to minimise the number of people in the lab at any one time. On any given day an allocated lab member changed the media for all cells as required rather than multiple people accessing the lab to each change media on their own samples.

Cells and EHT for preliminary experiments were all produced by me. For the final experiments I carried out media changes for the monolayer cells but not the EHTs. I did not complete the final insulin resistance protocol for any tissues (the preliminary experiments used a prototype protocol). Technicians at the Dunn School sliced and mounted all samples. All other aspects of experiments were conducted by me with supervision where required (e.g. with use of radioactive materials for Processing or where learning techniques). Appendix 5 Table 1 summarises who performed which stages of the experiments.

Appendix 5 Table 1*: Who completed each stage of preliminary and final experiments.*

	Samples for preliminary experiments	Samples for final experiments
Monolayer culture - controls and matured	Kirsti	Kirsti/Ujang
Monolayer culture- IR	Kirsti	Ujang
EHT culture – all samples	Kirsti	Ujang
Cell fixing – monolayer and EHT	Kirsti	Kirsti
Sample prep for EM	Dunn School	Dunn School
EM image acquisition	Kirsti	Kirsti
EM image analysis	Kirsti	Kirsti